Engineering of Highly Coherent Silicon Vacancy Defects in Silicon Carbide

Dissertation zur Erlangung des
naturwissenschaftlichen Doktorgrades
der Julius-Maximilians-Universität Würzburg

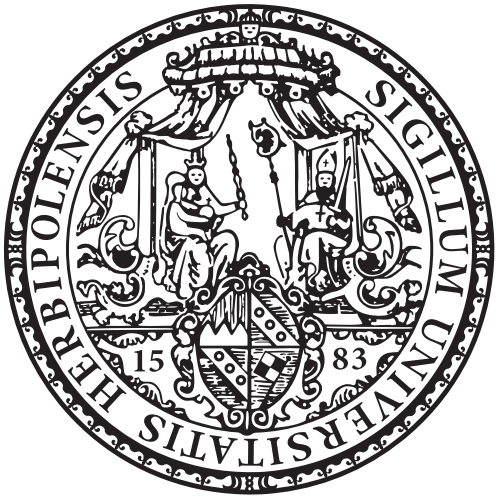

vorgelegt von

Christian Andreas Kasper

aus Gelnhausen

Würzburg, 2020

Eingereicht am: 03.12.2020
bei der Fakultät für Physik und Astronomie

1. Gutachter: Prof. Dr. Vladimir Dyakonov
2. Gutachter: Prof. Dr. Volker Christian Behr
3. Gutachter:
der Dissertation.

Vorsitzende(r): Prof. Dr. Karl Mannheim

1. Prüfer: Prof. Dr. Vladimir Dyakonov
2. Prüfer: Prof. Dr. Volker Christian Behr
3. Prüfer: Prof. Dr. Björn Trauzettel
im Promotionskolloquium

Tag des Promotionskolloquiums: 07.04.2021

Doktorurkunde ausgehändigt am:

Contents

1. Introduction

With electrical hardware components becoming ever smaller and approaching the limits of classical physics, the use of quantum effects for various applications came into the focus of research in the recent decades [1]. The idea of using these effects is not new [2]. However, the possibility of experimental feasibility has been long awaited. Today, the production of devices taking advantage of these effects is closer than ever before. Besides the famous applications like reducing algorithm complexity [3] with a quantum computer consisting of electron or nuclear spin qubits [4] or securing communication channels by means of quantum communication [5] or cryptography [6], there are many other possible applications. One of these applications with tremendeous potential is quantum sensing, capable of boosting measurement precision from the shot-noise limit to the Heisenberg-limit [7] and enabling magnetometry and thermometry with high sensitivity on the nanoscale [8].

With the transition from classical electronics to quantum electronic devices on the doorstep, the search for material platforms with suitable properties for the very demanding tasks involved is becoming increasingly important. A vast amount of candidates is available, hence to find the most universal and powerful ones is an ongoing task of today's research.

One approach in which significant progress has been made in recent years is the application of solid state spintronics. The manipulation and read-out of single, isolated spins capable of performing quantum operations in a controlled manner has been extensively studied [9] [10] [11] [12].

One of these systems is the NV^--center in diamond, standing for a vacancy right next to a nitrogen impurity substituting a carbon atom [13] [14]. Its properties, like near-perfect photostability [15] of single NV^--centers and a long spin coherence up to 600 ms [16], which is a prerequisite for a system of such kind, allow spin manipulation [17], utilization as magnetometers [18], bio sensing [19] and the use as single photon source [20].

As with every material system, there are also some drawbacks to the NV^--center in diamond. The processes to industrially fabricate diamond wafers are immature and no mass production has been established. Further, the manufacturing of devices in-

cluding diamond faces huge technological hurdles due to its large bandgap and consequently high electric resistance. A material platform with the same quantum properties, but cheaper and easier to produce is highly desirable.
Color center defects in silicon carbide (SiC), namely the silicon vacancy (V_{Si}) or the divacancy, hit this exact notch. They are attracting growing attention because of their appealing optical and spin properties. While the V_{Si} defects show slightly shorter spin coherence [21] [22], an existing SiC industry with mature fabrication processes provides large scale production of SiC wafers. Unlike NV^-, they are intrinsic lattice defects and allow the electrical control of the spin state, e.g. via photocurrent or electroluminescence [23]. SiC represents a technologically advanced material, utilized in high-power electronic components for decades. Quantum spintronics [24], single photon emission [25] as well as coherent control of isolated V_{Si} defects have been demonstrated [26].
A very vibrant and successful research area, in which V_{Si} defects as well show huge potential, is the development of a solid-state system for quantum sensing. In vivo quantum sensing of the temperature [27] in bio organisms provides a nanoscale resolution measurement technique, opening up completely new insights in medicine and biology. With its emission spectrum in the near infrared regime, where biological tissue is transparent, the V_{Si} defect in SiC is perfectly suited for applications of this kind. Magnetometry [8] and thermometry [28] have been demonstrated on V_{Si} defects in SiC and the robustness of SiC against radiation and other effects enables sensing applications with V_{Si} under extreme conditions, e.g. in space [29]. Another wide field of application for V_{Si} defect based quantum sensors is opened up by the transition of the automotive industry from internal combustion engine to e-mobility. The use of SiC in high power electronic components in electric cars is steadily increasing. The intrinsic V_{Si} defect potentially allows a very sensitive measurement of magnetic fields, electrical currents and the temperature inside the electronic components with nanometer precision.
The mentioned fields of application of V_{Si} based quantum sensors are only a fraction of the possible applications. What they all have in common, however, is that the V_{Si} defects utilized for quantum sensing need to have certain properties. On the one hand, a sufficiently high defect density is necessary to measure magnetic fields or temperatures in reasonable times, while on the other hand a long spin coherence resulting in a smaller linewidth is desirable, since this increases measurement precision [28].
In contrast to the well studied fabrication of SiC wafers, the influence of the V_{Si} defect creation method on their quantum properties is not adequately studied. The V_{Si} defects are commonly created by particle irradiation, predominantly electron or neutron irradiation but no systematic studies of the effect of irradiation on the V_{Si} defect optical and spin properties have been performed. This is grossly negligent, since the creation

process has a decisive impact on the V_{Si} defects' spin and optical properties.
This thesis is dedicated to the filling of this gap in knowledge about the V_{Si} generation. It is meant to provide an engineering guide of how to create V_{Si} defects with distinct properties, that make them suitable for quantum sensing, but also other quantum applications. The three methods of V_{Si} creation in this thesis are the irradiation of a SiC crystal with electrons, neutrons or protons. Each of these methods results in V_{Si} with different properties, depending on the interactions of the particles with the crystal. The engineering demonstrated in this thesis covers:

- Tuning of the emitter density by varying the irradiation fluence
- Targeted, three-dimensional writing of highly coherent V_{Si} by proton beam writing, scaled down to single V_{Si}
- Fine tuning of the V_{Si} spin coherence by varying the irradiation fluence
- Partial restoration of the V_{Si} photoluminescence and spin coherence in strongly irradiated samples by sample annealing
- Demonstration of Ramsey interferometry on V_{Si} defects to increase quantum sensing precision.

In chapter 5, the V_{Si} created with neutron, electron or proton irradiation were systematically analyzed with regard to their emitter density via photoluminescence (PL) spectroscopy and quantitative electron paramagnetic resonance (EPR). In this manner, optimal creation parameters for defects suitable for quantum sensing were established. Further, proton beam (PB) writing was utilized for a targeted creation of V_{Si} defects, enabeling defect writing into electronic structures. The fluence was reduced until single V_{Si} were observed.
Subsequently, the spin coherence of V_{Si} created by electron, neutron or proton irradiation was determined by means of pulsed Optically Detected Magnetic Resonance (pODMR) in a broad range of irradiation fluences in chapter 6. The results were compared to results obtained by other groups, which gives a wide overview over the effects of irradiation type and fluence on the coherence properties of the V_{Si} defects.
In chapter 7 several samples were annealed to explore the effect on the emitter density and the coherence properties of the V_{Si} defects.
In chapter 8 room-temperature spectral hole burning (SHB) spectroscopy of the V_{Si} defects in silicon carbide enriched with nuclear spin-free isotopes is presented. The mechanisms of inhomogeneous broadening were investigated and a model to describe the inhomogeneous broadening in the samples was developed. Further, two-frequency

Ramsey interferometry was performed to demonstrate absolute dc magnetometry. With the results obtained it is possible to create V_{Si} with desired properties, be it a high density of optically active emitters, a sufficiently long spin coherence or targeted creation into an already existing electronic structure. They ultimately show, that V_{Si} spin defects in SiC are a powerful quantum system for quantum sensing in a technologically advanced material, providing the possibility of custom made sample fabrication with predictable optical and quantum properties.

2. Theory

2.1. Silicon carbide

In this chapter an overview of the silicon carbide properties is given with a focus on crystal defects. After clarifying the basic physics and properties of silicon carbide, a brief explanation of crystal defects in general and their categorization is given.

2.1.1. Silicon carbide in industry and technology

Silicon carbide underwent a slow but steady development from a cheap abrasive to the technologically advanced material system it represents today. Already postulated by Jöns Jakob Berzelius in 1824 [30], it took another 70 years until it was first synthesized by Edward Goodrich Acheson in 1893 [31]. Still today, 127 years later, silicon carbide is the only known stable chemical compound of carbon and silicon. Its natural occurance has, until now, only been reported in meteorites [32]. Its career as an actual high-tech material took off in the 1990s [33] with the possibility of large scale wafer production with sufficient quality and for a reasonable price.
SiC can be viewed as a hybrid between diamond and silicon, combining the advantages of both materials. This leads to some extraordinary properties, some of which are presented in tab. 2.1.

Being one of the hardest materials known in combination with its thermal robustness make it a suitable material system for applications in extreme conditions: From ceramic composite brakes in sports cars (e.g. BMW) [38] to bulletproof vests - SiC can be found where other materials reach their limits. Not only its sturdiness, but also the fact that SiC is a semiconductor with a high breakdown voltage is of great benefit. Hence, SiC is widely used in high power electronics and can be found in a variety of modern electronic devices.
Another recent research topic in which SiC produced headlines is also the topic of this thesis: color center defects for quantum applications. The manipulation of their spin via a microwave field [39] as well as optical [40] or electrical [23] read-out have been demonstrated and they provide outstanding quantum properties for a wide field of

	Silicon	Silicon Carbide	Diamond
Hardness (Mohs)	6.5	9.5	10
Breakdown Field ($MVcm^{-1}$)	0.3	2 – 3	
Thermal Conductivity ($Wcm^{-1}K^{-1}$)	1.1	3.87	10 – 25
Band Gap (eV)	1.5	2.3 – 3.3	5.5

Table 2.1.: Comparison of the physical properties of Si, SiC and diamond [34] [35] [36] [37]

quantum applications and are therefore being intensively studied by many groups. Especially sensing applications based on quantum defects in SiC have become a focus of attention in recent years. Its radiation resistance makes it applicable in space and provides the possibility of potentially using it for magnetic field and temperature sensing applications in next generation exploration spacecrafts [41] [29].
In order to understand the nature of these crystal defects in SiC, a closer look at the crystal structure is essential.

2.1.2. Crystal structure and polytypism

SiC is a wide band gap semiconductor consisting of silicon (Si) and carbon (C) atoms. Each Si atom is surrounded tetrahedrally by four C atoms and vice versa. As displayed in fig. 2.1, the crystal structure can be described by crystal layers with a bi-atomic basis of one Si and one C atom.

While the arrangement in these layers is always hexagonal, the stacking order along the c-axis may vary. Depending on this stacking sequence, SiC occurs in a variety of different crystal structures. This phenomenon is called polytypism and one distinct structure is referred to as a polytype. There are more than 250 polytypes of SiC known so far [42]. While they all have the same chemical formula, the different stacking orders result in slight differences of their physical properties (e.g. the bandgap).
Fig. 2.2 shows the systematic build-up of two different polytypes and their corresponding stacking sequences. With the position of the first layer being A and the one of the second layer being B, there are two possible positions for the third layer (A or C).

In order to uniquely name and simultaneously provide the main information about each polytype, the systematic Ramsdell nomenclature was introduced [43]:

- The first part of the designation is the number of repeating crystal layers in the sequence.

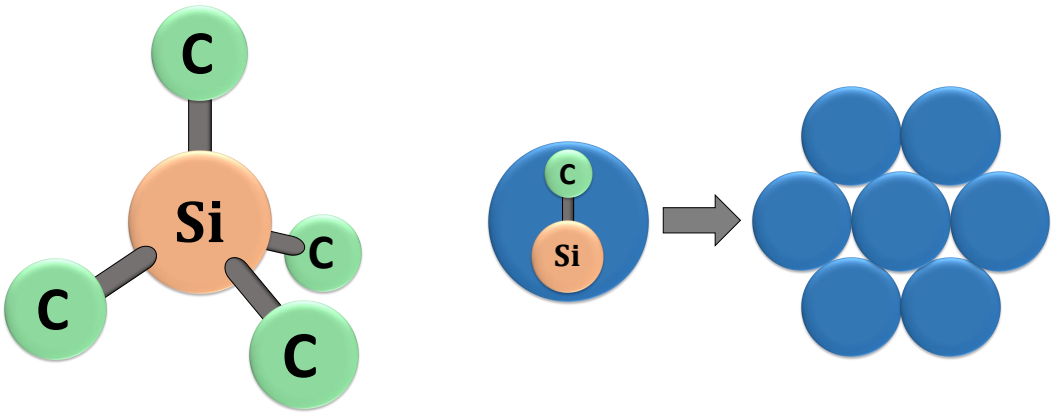

Figure 2.1.: left: Silicon atom in a SiC crystal, tetrahedrally surrounded by four carbon atoms. **right:** Structure of a SiC crystal layer formed by two-atomic bases consisting of a silicon and a carbon atom.

- The second part describes the phase of the polytype, e.g. cubic (C), hexagonal (H) or rhombic (R).

The polytypes 3C- (ABC), 4H- (ABAC) and 6H-SiC (ABCACB) are the easiest to fabricate and hence the most common. In this work, exclusively 4H- and 6H-SiC were studied and all following theory refers to these two polytypes.

2.1.3. Crystal defects

Every genuine crystal contains irregularities in its crystal lattice, so called crystal defects. While some of these defects have no practical use and only hamper the performance of e.g. electrical components [44], other defects offer astounding possibilities and are not meant to be avoided, but highly desired in certain application fields.
Keeping in mind the polytypism of SiC, one can already guess, that SiC offers a plethora of these defects. They have to be distinguished with regard to their macroscopic and microscopic effects on the physical properties of a crystal. One way to categorize them is by their dimensionality:

- **Three-dimensional defects:** Large areas where the crystal is imperfect. They may consist of clusters of impurities, like inclusions of foreign substances or voids. They are generally created by growth failures. In high density, they may impede the performance or stability of the host crystal, but are of no use for quantum applications.

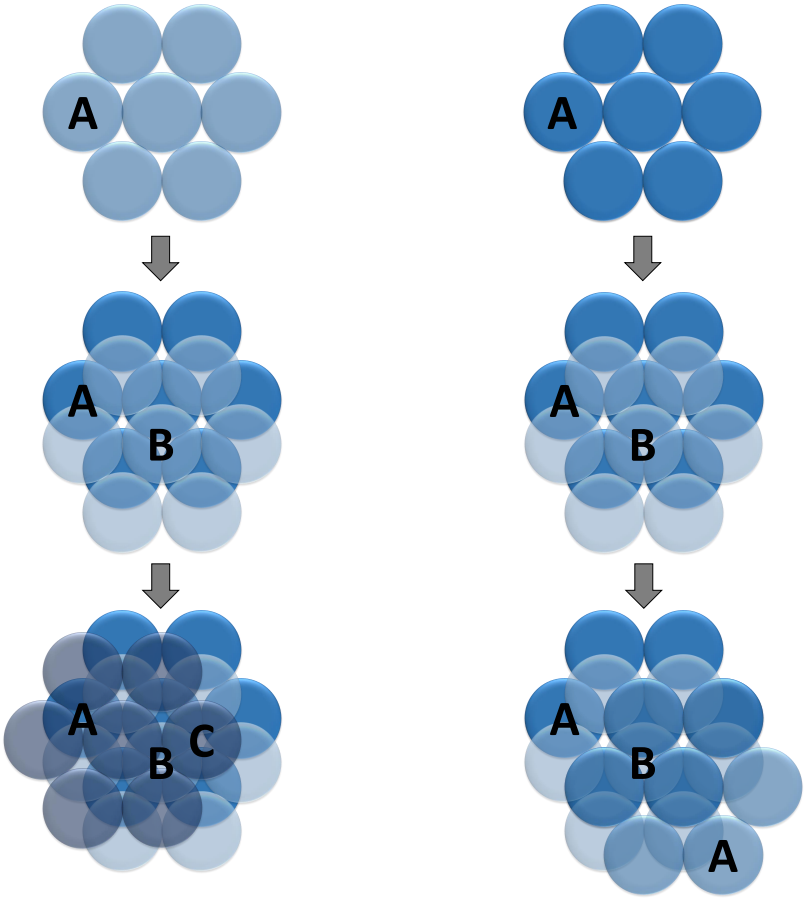

Figure 2.2.: Schematic build-up of two different SiC polytypes out of hexagonal crystal layers formed by a bi-atomic basis of one C and one Si atom. For every new layer there are two possible orientations.

- **Two-dimensional defects:** Mainly grain boundaries in polycrystals or faults in the stacking sequence of a polytype. Similar to the three-dimensional defects, they may impede the performance or stability of e.g. electronic devices, but are also not suitable for the experiments in this work.

- **One-dimensional defects:** Mostly edge or screw dislocations. They may be optically active and hence influence the optical pump cycle of quantum centers (See 2.2.5). Wafers produced nowadays, however, do not show a high density of these dislocations anymore and therefore their influence can be neglected [45].

- **Zero-dimensional defects:** Point defects that can be categorized into extrinsic and intrinsic defects:

1. **Extrinsic:** Defects involving impurities. In the most common cases the foreign atom is either substitutional and replacing a lattice atom or interstitial and located between the lattice sites. Extrinsic defects are often created on purpose, e.g. in the form of dopands.
2. **Intrinsic:** Defects not involving impurities. There is a plethora of intrinsic defects in SiC, the most important ones are listed below:
   a) **An interstitial** is an atom positioned between the lattice sites.
   b) **An antisite** occurs, when a Si-Atom sits on a C lattice site or vice versa.
   c) **A Frenkel pair** consists of an interstital that is bound to a a vacancy.
   d) **A vacancy** is an empty lattice site.

   Also, combinations of a) to d) are possible. This, in combination with the polytypism, gives again an idea of the immense variety of point defects in SiC.

   In addition to this variety, point defects may have several different charge states. Since negatively charged, optically active point defects often change the color of the crystal, they are commonly referred to as color center defects.

In our investigations, we are interested in a certain type of color center defects, more precisely, in negatively charged silicon vacancies (V_{Si} defects) in 4H- and 6H-SiC. It was demonstrated that they can be utilized for room temperature quantum metrology [39] [46] [47] [48], including magnetometry [28] [8] [49] [40] [50] [51] and thermometry [28] [52]. Moreover, single photon emission has been demonstrated [53] [25] and most recently spin state manipulation of single V_{Si} has been accomplished [54] [26]. Also, V_{Si} have the potential to be used as microwave amplifiers, bringing the idea of a defect based MASER into reach [55]. Last but not least, the possibility to access V_{Si} defects optically or electrically and to manipulate their spin states via a microwave field make them potential candidates as qubits for quantum information processing and quantum computing [10] [56] [57]. The outstanding quantum properties of the V_{Si} defects allowing all these applications are discussed in the following.

2.2. The silicon vacancy defect

After the crystal structure of SiC and the nature of its defects has been discussed, the attention is focussed on the main cause around which this thesis revolves: The quantum characteristics of the negatively charged V_{Si}-defect. First, the advantages of V_{Si} defects compared to comparable material systems are highlighted. Then their energy scheme

and spin states are presented, which leads directly to their most extraordinary feature, their optical pump cycle.

2.2.1. Benefits of the silicon vacancy

The V_{Si} defect is not the only color center defect suitable for the aforementioned quantum applications. The first defect to show the possibility of this kind of quantum control was the NV^--center in diamond [14] [16]. The NV^--center and the V_{Si} defect share very similar properties and the methods to engage them are almost the same. Besides these two material systems, other systems like quantum dots [58], superconducting Josephson junctions [59] or trapped ions [60] are promising candidates for application fields like quantum computing or communication and low scale quantum operations have already been performed with these systems. This raises the following question: What are the advantages of V_{Si} defects compared to these systems that justify the euphoria?
The main benefit of NV^- centers in diamond or the V_{Si} defect in SiC compared to the other systems is the applicability at room temperature. Quantum dots, superconducting Josephson junctions or trapped ions usually need to be cooled to cryogenic temperatures in order to work at all. Therefore, future large scale production or everyday usability of these systems faces almost insurmountable hurdles.
Compared to the NV^--centers, V_{Si} defects in SiC, too have several advantages. One consists in the fact that SiC is a well established, technologically highly advanced material. There exists a manufacturing industry and wafers can be bought for reasonable prices, while the production of diamond is costly. As SiC is already used in high power electronics, the industrial fabrication of V_{Si} implemented in electronic structures is convenient compared to NV^- in diamond. Also, V_{Si} defects are intrinsic defects, which again simplifies production a lot, because no foreign atoms need to be implanted in the process.
Another advantage of V_{Si} over comparable material systems is the variability of material parameters and defect types due to polytypism. As mentioned before, different polytypes show slight differences in their physical properties, like bandgap, breakdown field or thermal conductivity. Hence, polytypism can be seen as a tool to tune material parameters custom-made for individual requirements. The color center defects furthermore show slight differences in the emission spectrum and energetic structure in the various polytypes, adding even more degrees of freedom to the material platform.
The emission spectrum itself too has benefits compared to e.g. the NV^--centers' red emission. V_{Si} defects emit light in the near infrared regime (NIR), which is beneficial for in vitro bioimaging, as biological tissue autofluorescence and attenuation are lower

in the NIR [61]. In terms of communication, a V_{Si} defect-based MASER could serve as a low noise amplifier on the receiving end, e.g. for deep space communication [62]. All these properties underline why it is important and necessary to have a closer look at these V_{Si} defects and that they rightly have their place in this research field.

2.2.2. Charge state and energy levels

As shown in fig 2.3, a V_{Si} defect is a free Si lattice site that is occupied by the four dangling bonds of the surrounding carbon atoms.

In 4H-SiC, there are two unequal lattice places for a V_{Si} defect, in 6H-SiC three. The slightly different direct environment results in small differences for their optical and spin properties, although their general quantum properties are very similar. In the following it is sufficient to explain the physics of the V_{Si} defect in 4H-SiC. The differences of V_{Si} defects in 6H-SiC will be highlighted at the necessary points.

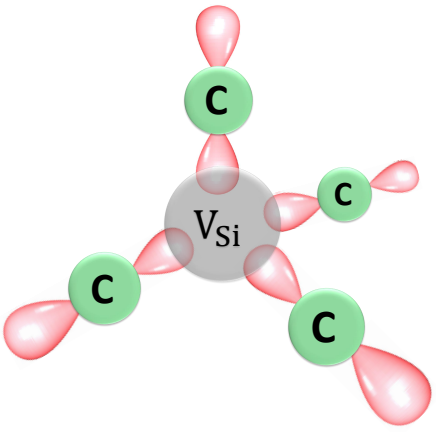

Figure 2.3.: Schematic representation of a silicon vacancy in SiC. The wave functions of the four dangling bonds overlap at the position of the V_{Si} defect.

According to the C_{3V} symmetry of the system, the environment of a V_{Si} defect gives rise to discrete energy levels which the unbound electrons may occupy [63], the lowest of which (a_1') is double degenerate and located inside the valence band. Two additional levels (a_1 and e) lie within the band gap, with a_1 being double and e being quadruple degenerate (See fig. 2.4) [63]. Since a_1' can host two electrons with antiparallel spins, a triplet system with S = 1 is formed.

It was shown by our group, that the optically and spin active color center type of V_{Si}-defects in 4H-SiC are spin quartets with $S = 3/2$ [39]. Hence, the V_{Si} defect must be in the negative charge state in order to be suitable for spin manipulation. This is the

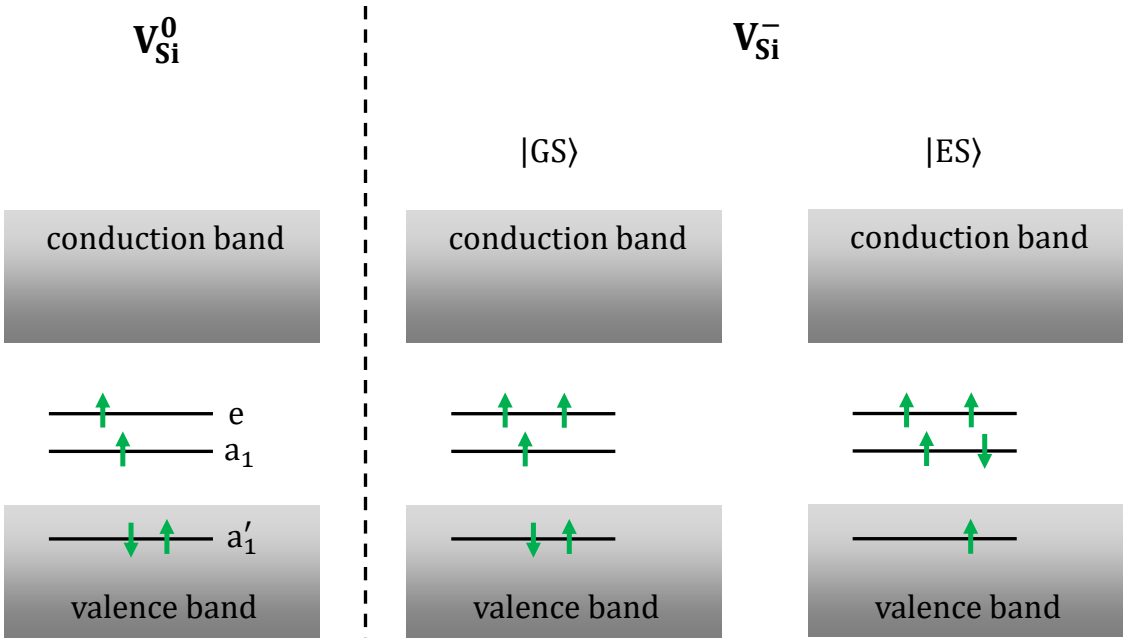

Figure 2.4.: Energy levels of the V_{Si} defect. **left:** Possible population of the energy levels of a V_{Si} defect with no net charge. The levels a_1' and a_1 are double degenerate, e is quadrupole degenerate. **middle:** Negatively charged V_{Si} defect in the ground state. Two electrons populate a_1'. **right:** Negatively charged V_{Si} defect in the excited state. In this case, an electron is lifted from a_1' to a_1 or e.

case, if an additional electron is captured and a total of five electrons occupies the V_{Si}-defect. Two of the electrons are again paired in the lowest energy level a_1', which results in a quadruplet spin system with $S = 3/2$. Since only this negative charge state is of interest for this work, the term "V_{Si}-defect" refers to the negatively charged V_{Si} defect in 4H-or 6H-SiC from this point on.

It is possible to optically excite negatively charged V_{Si} defects by exciting one of the electrons from a_1' to a_1 or e. Describing quantum phenomena in a vacancy with five electrons and complex geometry will ultimately lead to complex pictures. A more convenient approach is to describe the system in total, as illustrated schematically in fig. 2.5. In this simplified picture, an excitation of an electron from a_1' to a_1 or e is represented by an energetical jump of the complete system from a ground state |GS⟩ to an excited state |ES⟩. Since a_1 and e are energetically located very close to each other, the two electron jumps from a_1' to a_1 and a_1' to e can be treated equally in this picture.
Another circumstance that must be taken into account when describing the energetic structure of the V_{Si} defects is the existence of two inequivalent lattice sites for a silicon atom in 4H-SiC: One hexagonal and one cubic lattice site. Considering the stacking order ABCB of 4H-SiC, a V_{Si} defect located between crystal layers with the same orientation, i.e. in layer A or C, has a hexagonal geometry. One located between layers with

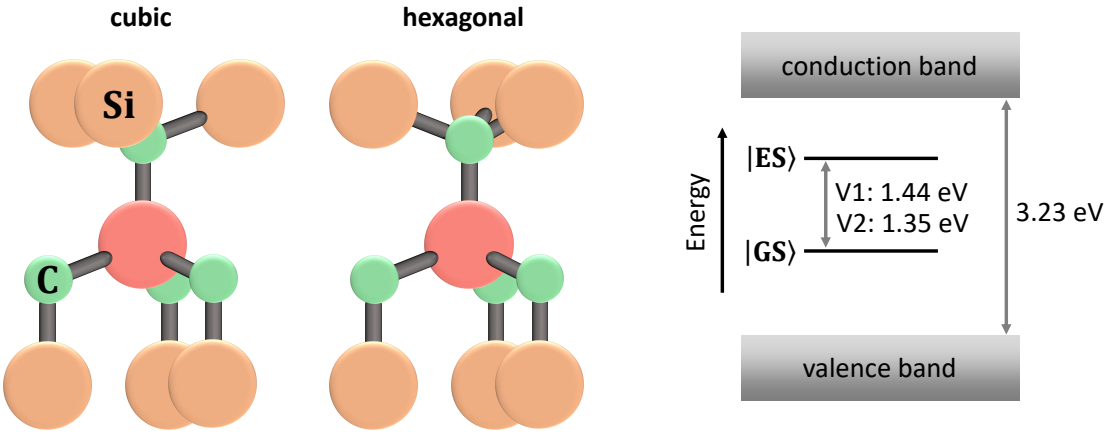

Figure 2.5.: Geometry and energetic location of a negatively charged V_{Si}. **left and middle:** Cubic or hexagonal environment of a V_{Si} defect in a 4H-SiC crystal. V_{Si} with a hexagonal environment are denoted as V1, those with a cubic environment as V2. The configuration of the next neighbour C atoms is equivalent for V1 and V2, but the next nearest neighbour Si atoms are arranged differently. **right:** Schematic energetic position of a V_{Si} quantum system between valence and conduction band. The excitation of a V_{Si} defect in this picture is represented by a transition from a ground $|GS\rangle$ into an excited state $|ES\rangle$. The energy gap between these states differs for V1 and V2.

varying orientation, i.e. layer B, has a cubic geometry (See fig. 2.5). In this work the V_{Si} defects located at lattice sites with hexagonal environment are denoted as V1 and the ones with cubic environment V2. Due to the varying local geometry, the energy between $|GS\rangle$ and $|ES\rangle$ also varies. Hence, there are two possible values for the energetic gap between $|GS\rangle$ and $|ES\rangle$, which influences the photoluminescence spectrum of the V_{Si} defects.

2.2.3. Photoluminescence

When excited optically from $|GS\rangle$ to $|ES\rangle$, the V_{Si}-defects relax back into $|GS\rangle$ after a while and emit photoluminescence (PL). A spectrum of this PL at room temperature together with one at cryogenic temperature is presented in fig. 2.6.

At low temperatures the spectrum consists of sharp lines with high intensity. These are the emission lines ("Zero-Phonon-Lines" (ZPL)) of various crystal defects according to the respective energy difference $E_{ZPL} = E_{|ES\rangle} - E_{|GS\rangle}$ between an excited and a ground state. In the case of the V_{Si} defect, there are two ZPLs, one for V1 at 862 nm and one for V2 at 917 nm, corresponding to the energy differences E_{ZPL} [64]. As in the case of every crystal defect PL, the spectrum at room temperature does not show ZPLs, but prominently consists of their phononic sideband. It arises, because the V_{Si} defects interact with crystal phonons during relaxation. This process can be described using

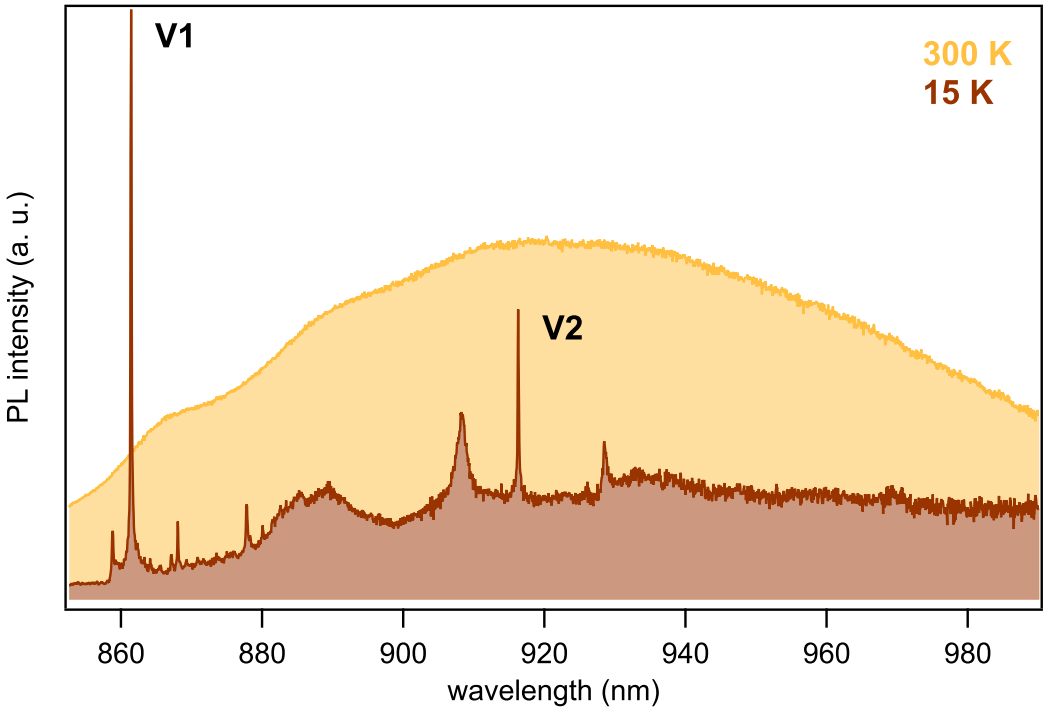

Figure 2.6.: PL spectrum of a V_{Si} ensemble in 4H-SiC at room temperature and 15 K. For excitation a 632 nm He-Ne laser was used. The spectrum at 300 K is broadened due to interactions of the V_{Si} with phonons. At 15 K the spectrum collapses into sharp lines due to a low phonon density. These lines can be attributed to optically active crystal defects and are called zero-phonon-lines (ZPL). The ZPL of V1 and V2 are prominent in the spectrum, hinting at a high percentage of V_{Si}.

the model of vibronic states of |GS⟩ and |ES⟩ with deviating energy, according to the Frank-Condon principle [65]. The phononic sideband is red-shifted in emission and blue-shifted in absorption (See fig. 2.7). It only collapses into the ZPLs at low temperatures as a result of a low phonon density. Since the ZPL is characteristic for a certain type of crystal defect, it can be used to identify defects and very roughly estimate the ratio between the densities of the different defect types in a crystal.

2.2.4. Spin states and zero field splitting

The energy model in fig. 2.5 is very simplified and does not take a basic property of electrons into account: their spin. As discussed above, the negatively charged V_{Si} defect is a spin quartet system with $S = 3/2$. Hence, there are four magnetic quantum numbers $M_s = \pm 1/2 / \pm 3/2$ possible for the ground state |GS⟩ as well as for the excited state |ES⟩.
However, |GS⟩ and |ES⟩ are not energetically degenerate with regards to M_s. EPR studies revealed that they are each split into a $|\pm 1/2\rangle$ and $|\pm 3/2\rangle$ spin sublevel, while $|\pm 1/2\rangle$

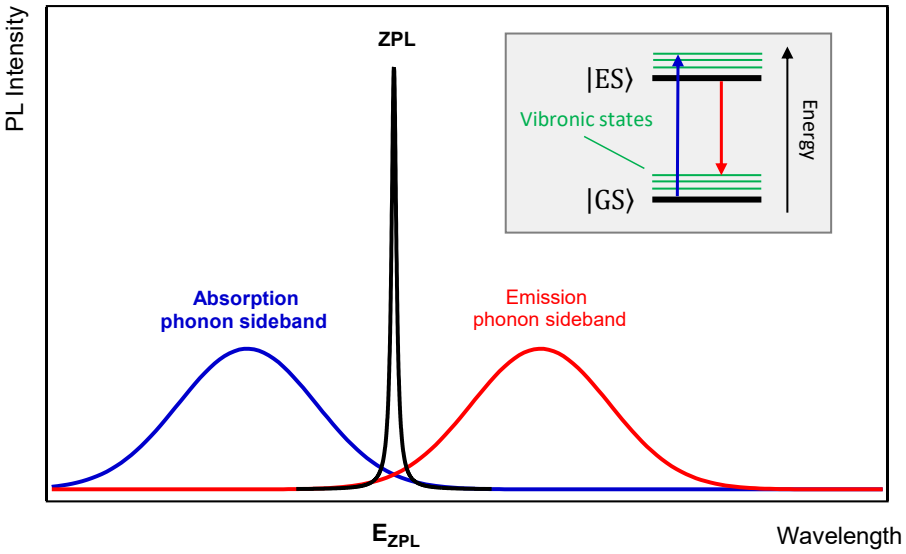

Figure 2.7.: Zero phonon line and phonon sidebands. The ZPL is the direct absorption/emission line without phonon interaction. It is characteristic for a specific defect type. Due to interactions with lattice phonons, the emission/absorption shifts and forms an absorption/emission band according to the Franck-Condon principle. **inset:** Schematic representation of the vibronic states of the V_{Si}. They can be seen as virtual states in a model to describe the interaction of V_{Si} and crystal phonons during luminescent relaxation.

is energetically more favourable for the system (See fig. 2.8) [66]. The energy gap $E_{ZFS} = E_{\pm 3/2} - E_{\pm 1/2}$ between these spin states is called zero field splitting (ZFS). In general, a ZFS of a quantum system can be described with a spin Hamiltonian given by [26]:

$$\hat{\mathscr{H}}_{spin} = D\left[\hat{S}_z^2 - \frac{\hat{S}\left(\hat{S}+1\right)}{3}\right] + E\left(\hat{S}_x^2 - \hat{S}_y^2\right) \tag{2.1}$$

with the spin operator $\hat{S} = \left(\hat{S}_x, \hat{S}_y, \hat{S}_z\right)^T$. The ZFS can entirely be described by the parameters D and E. The parameter D describes an axial anisotropy and corresponds to 35 MHz for the V2 V_{Si} defect with $E << D$ [26]. The matrix form of the above Hamiltonian can be given as:

$$\begin{Bmatrix} D & 0 & \sqrt{3}E & 0 \\ 0 & -D & 0 & \sqrt{3}E \\ \sqrt{3}E & 0 & -D & 0 \\ 0 & \sqrt{3}E & 0 & D \end{Bmatrix} \tag{2.2}$$

The eigenvalues deliver the energies of the states

$$\begin{aligned} -\sqrt{D^2+3E^2} \quad &\text{for} \quad M_s = \pm 1/2 \\ +\sqrt{D^2+3E^2} \quad &\text{for} \quad M_s = \pm 3/2 \end{aligned} \tag{2.3}$$

and therefore the energy E_{ZFS} of the ZFS as a function of D and E:

$$E_{\mathrm{ZFS}} = 2\sqrt{D^2+3E^2} \tag{2.4}$$

Analogous to the energy gap E_{ZPL} between |GS⟩ and |ES⟩, E_{ZFS} differs for V1 and V2 due to the local geometry. The value $E_{\mathrm{ZFS,V1}} = 0.17\,\mu$eV of V1 is slightly smaller than the one of V2 with $E_{\mathrm{ZFS,V2}} = 0.27\,\mu$eV [66].
Different theories, involving the reduction of group symmetry, crystal field deformation by a carbon vacancy in the vicinity of the V_{Si} defect and many-electron effects exist regarding the exact nature of the ZFS and it is still the subject of ongoing research [24] [67] [68]. For this study however, the exact origin of the ZFS is not of central importance. Hence, a more detailed discussion of this is waived.

2.2.5. Optical pump cycle

The fundamental feature of the V_{Si} defects with regard to all aforementioned quantum applications involving spin manipulation is the possibility to generate a spin polarization by optical excitation [24]. The theoretical description of this process is highly complex and beyond the scope of this work. For detailed theoretical calculations it is referred to [69]. However, based on certain assumptions, the process can be described sufficiently with the energy model in fig. 2.8 [28].

After excitation into |ES⟩, there are two main relaxation paths for a V_{Si} defect. The first relaxation path is the already discussed photoluminescent optical relaxation under spin preservation, e.g.:

$$|\mathrm{GS}_{1/2}\rangle \rightarrow |\mathrm{ES}_{1/2}\rangle \rightarrow |\mathrm{GS}_{1/2}\rangle \tag{2.5}$$

The second relaxation path is non-luminescent and possible due to the existence of several metastable states |MS⟩, energetically located between |GS⟩ and |ES⟩ [24]. In contrast to the luminescent relaxation, spin preservation does not apply for the transitions from |MS⟩ to |GS⟩ and intersystem crossing is possible.
It has been shown that the ratios of the transition rates of luminescent and non luminescent transitions lead to one spin level ($|\pm 1/2\rangle$ or $|\pm 3/2\rangle$) being preferentially populated [24]. This process is called spin alignment. The polytype and geometry of the

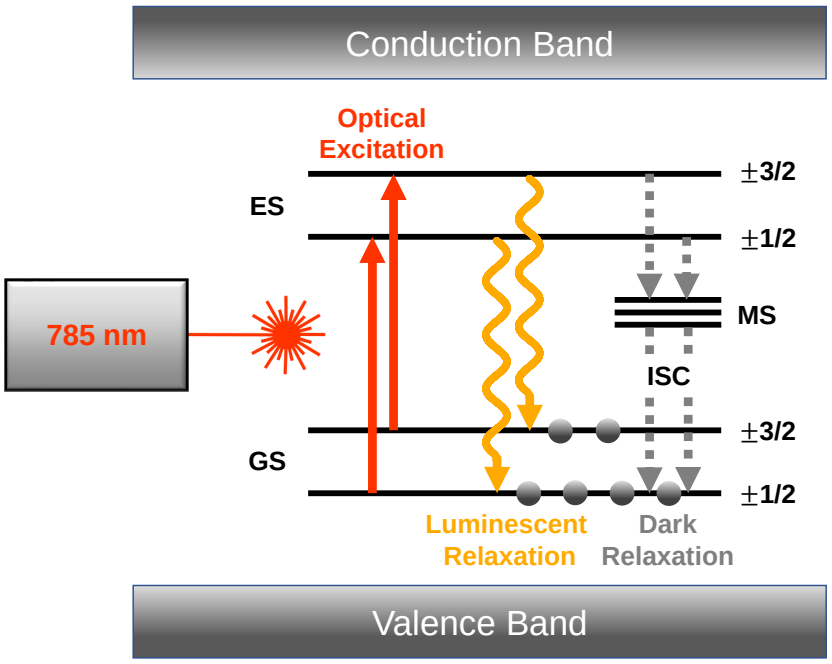

Figure 2.8.: Pump cycle model of a V_{Si} defect. After optical excitation with a laser (red arrows) there are two possible relaxation paths. Optical relaxation (yellow arrows) happens under spin preservation. Intersystem crossing is possible for relaxation over a set of metastable states (grey arrows). The transition rates between all states determine the properties of the V_{Si}: The $|\pm 1/2\rangle$ spin sublevel is pumped under optical excitation and the PL emission of a vacancy in the $|\pm 3/2\rangle$ sublevel is higher than of one in $|\pm 1/2\rangle$.

V_{Si} defect determine which of the two spin sublevels is preferentially populated. In the case of V2 in 4H-SiC the $|\pm 1/2\rangle$ state is preferentially populated. In this manner, the optical pump mechanism enables the initialization of the system into $|\pm 1/2\rangle$.
The interplay of the transition rates has a further effect: V_{Si} defects in the $|\pm 3/2\rangle$ state are brighter, i.e. they emit more PL than those in the $|\pm 1/2\rangle$ state. This spin dependent PL provides the possibility of reading out the spin state of an ensemble or a single V_{Si} via PL. The optical pumping of $|\pm 1/2\rangle$ and the spin dependent PL represent the basic principles of optically detected magnetic resonance (ODMR), which is the main experimental method in this work and explained in 4.4.

2.2.6. Spin sublevels in an external magnetic field

The ODMR measurements in this thesis were conducted with a small external magnetic field applied to the sample. This small field supresses interactions that lead to dephasing of the V_{Si} defect spin coherence, which will be thoroughly dicussed in detail in 6.3.

If the V_{Si} defects are exposed to an external magnetic field B_0 along the spin quantization axis (i.e. $\vec{B}_0 = (0,0,B_0)^T$), the spin Hamiltonian needs to be extended by a Zeeman term [40]:

$$\hat{\mathscr{H}}_{spin} = D\left[\hat{S}_z^2 - \frac{\hat{S}\left(\hat{S}+1\right)}{3}\right] + E\left(\hat{S}_x^2 - \hat{S}_y^2\right) + g\mu_b B_0 \hat{S} \tag{2.6}$$

Where g is the isotropic Landé g factor (g=2.0028), μ_B is the Bohr magneton and $S = 3/2$. This leads to four eigenvalues [70]:

$$\begin{aligned}
&\sqrt{\left(g\mu_b B_0 + D\right)^2 + 3E^2} + \frac{g\mu_B B_0}{2} \quad \text{for} \quad M_s = +3/2 \\
&\sqrt{\left(g\mu_b B_0 - D\right)^2 + 3E^2} - \frac{g\mu_B B_0}{2} \quad \text{for} \quad M_s = +1/2 \\
&-\sqrt{\left(g\mu_b B_0 + D\right)^2 + 3E^2} + \frac{g\mu_B B_0}{2} \quad \text{for} \quad M_s = -1/2 \\
&-\sqrt{\left(g\mu_b B_0 - D\right)^2 + 3E^2} - \frac{g\mu_B B_0}{2} \quad \text{for} \quad M_s = -3/2
\end{aligned} \tag{2.7}$$

If the V_{Si} defects are exposed to an external magnetic field, the spin sublevels of the ground state $|GS\rangle$ as well as of the excited state $|ES\rangle$ are not degenerate anymore, but split due to Zeeman interaction.
The spin sublevels of the V_{Si} defect are still doubly degenerate without external magnetic field, even in presence of electric and strain fields [28]. In contrast to $S = 1$ systems, E does not result in an additional splitting for the $S = 3/2$ V_{Si} defect [70]. With $E = 0$ the spin Hamiltonian can be written as:

$$\hat{\mathscr{H}}_{spin} = D\left[\hat{S}_z^2 - \frac{\hat{S}\left(\hat{S}+1\right)}{3}\right] + g\mu_b B_0 \hat{S} \tag{2.8}$$

Another simplification can be reached, if the direction of B_0 is along the c-axis $B_0 \parallel c$. This was the case in all experiments in this thesis and leads to a linear evolution of the energies of the spin sublevels with the magnetic field B_0:

$$\begin{aligned}
&D + \frac{3}{2} g\mu_b B_0 \quad \text{for} \quad M_s = +3/2 \\
&-D + \frac{3}{2} g\mu_b B_0 \quad \text{for} \quad M_s = +1/2 \\
&-D - \frac{3}{2} g\mu_b B_0 \quad \text{for} \quad M_s = -1/2 \\
&D - \frac{3}{2} g\mu_b B_0 \quad \text{for} \quad M_s = -3/2
\end{aligned} \tag{2.9}$$

The evolution of the spin sublevels in dependence of the magnetic field B_0 is displayed in fig. 8.5.

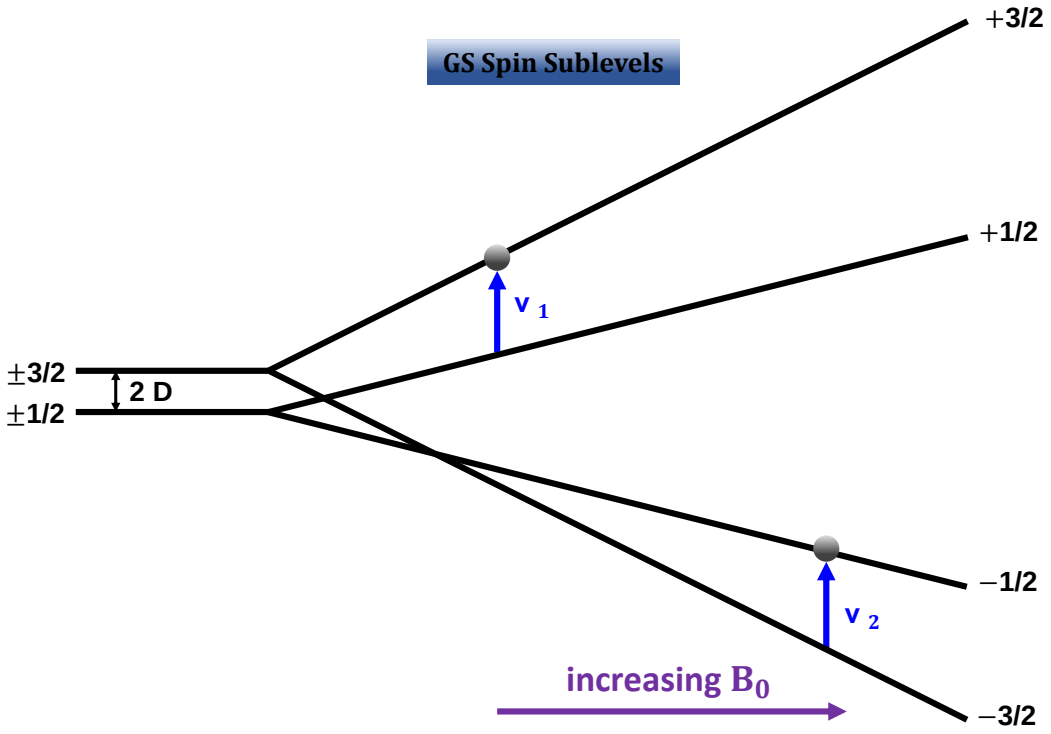

Figure 2.9.: Zeeman splitting of the $|\pm 1/2\rangle$ and $|\pm 3/2\rangle$ spin sublevels in an external magnetic field B along the c-axis. The resonant transitions between the sublevels (blue arrows) can be observed in the cwODMR measurements in 4.4.

Notably, this Zeeman splitting does not influence the optical pumping mechanism, $|+1/2\rangle$ and $|-1/2\rangle$ are equally pumped. In a magnetic field, there are two resonant transitions, one between $|+1/2\rangle$ and $|+3/2\rangle$ and one between $|-3/2\rangle$ and $|-1/2\rangle$ (blue arrows in fig. 8.5), instead of only one at zero field. The transitions are denoted by ν_1 and ν_2 and are observable in ODMR spectra of the form presented in 4.4.

3. Samples

One claim of this thesis is to be a universal manual for the generation of V_{Si} defects in 4H-SiC with certain properties for specific applications. It is therefore essential to discuss the manufacturing process of SiC and the creation of V_{Si} defects in detail.
This chapter covers the preparation of the samples used in this work. At first, the focus is on the growth of SiC crystals. Subsequently, the creation of V_{Si} defects in SiC by particle irradiation is discussed. A number of methods are available, from ensemble generation by electron or neutron irradiation down to the generation of V_{Si} defects at desired locations in the crystal by proton beam writing. Finally, the process of crystal annealing is explained.

3.1. Silicon carbide wafers

The common growth processes of SiC bulk crystals involve sublimation, since SiC does not melt under atmospheric pressure, but sublimates at 1800°C [34]. Today, physical vapor transport (PVT) growth methods are state of the art. In this case, the SiC in condensed phase (often a powder) is sublimated and then deposited to form a crystal [71]. The oldest method is the Lely method (1954), where SiC powder is placed in a graphite crucible and sublimated at 2500°C [72]. In the middle of the crucible there is a cooled graphite rod on which the sublimated SiC deposits and forms a crystal. Usually, an argon gas atmosphere is used to prevent reactions with nitrogen or oxygen. Since these early stages the methods steadily improved. Today it is possible to commercially purchase SiC wafers with near perfect quality. The densities of significant irregularities in terms of electronic device performance, like micropipes and dislocations, are in the low $10^4\,\mathrm{cm}^{-3}$ range [73].
The majority of samples used in this thesis are high purity semi-insulating (HPSI) 4H-SiC wafers purchased from Cree or Norstel. Semi-insulating semiconductors are semiconductors featuring a very high electrical resistivity. This is achieved by a large bandgap, as given in SiC, and a low charge carrier density [74]. In the beginning of HPSI wafer production, vanadium dopands were used as deep level traps to reduce the charge carrier density [75]. However, the absolute density limit of Vanadium atoms in SiC is in the

mid $10^{17}\,cm^{-3}$ range [73]. To overcome this limit, the nitrogen, boron and aluminium density were reduced by source purification and the use of high quality graphite for the growth process. With this step vanadium dopands are not necessary and intrinsic defects are sufficient as deep level traps [76] [71]. In case of the wafers used in this thesis, the experiments were performed in high purity epitaxially grown layers in the wafer with a very low residual dopand density of $\approx 5 \times 10^{14} cm^{-3}$.
In summary this means, HPSI SiC wafers are SiC crystals, containing a very low density of already negatively charged V_{Si} defects. They therefore represent an optimal environment to investigate their spin and coherence properties.

3.2. Defect creation by particle irradiation

The two most frequently used methods for the introduction of intrinsic defects in SiC are specific adjustments of the growth conditions [24] or high energy particle irradiation after growth. However, controlling the growth process in such way, that a homogeneous defect density distribution is achieved, is quite challenging. Also, since the results should be application oriented, it was more in the spirit of this thesis to use commercially available wafers. Therefore, the method of choice in this work was irradiation with electrons, neutrons or protons. There is no optimum irradiation method, as they all have their own advantages and disadvantages, which are schematically presented in fig. 3.1.

While neutrons create a completely homogeneous defect distribution [53] [77], electrons show a certain energy dependent penetration depth, resulting in a defect density gradient [78] [79]. Protons interact according to the quantum mechanical Bethe equation and create a layer of defects with the layer depth being a function of the energy of the protons [80].

3.2.1. Neutron irradiation

In combination with high irradiation fluences, neutron irradiation allows to create high-density V_{Si} ensembles, as required for the realization of room-temperature masers [39] and highly sensitive magnetic field sensors [28]. Since neutrons are not charged, they lose almost all of their energy in collisions with nuclei in the lattice and hence considerably damage the SiC crystal [81]. This leads to the creation of a multitude of defect types other than V_{Si} up to the formation of defect clusters.
The samples used in this thesis were irradiated in two different research reactors. During irradiation, all neutron irradiated samples were cooled to avoid heating by the neu-

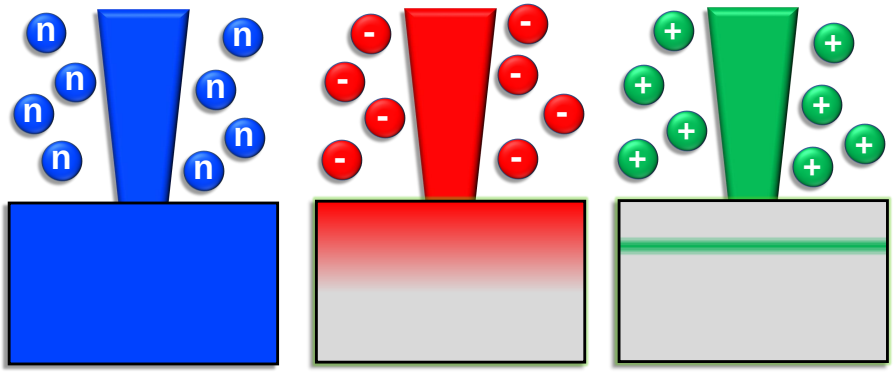

Figure 3.1.: Schematic generation of V_{Si} defects in SiC by MeV particle irradiation. **left:** Neutron irradiation leads to a homogeneous distribution of V_{Si} defects in the crystal. **middle:** Electrons show a penetration depth depending on the electron energy. In case of thick samples, this may lead to a gradient of the V_{Si} density with highest density close to the surface. **right:** Ion irradiation (with e.g. protons) results in the formation of a V_{Si} layer at a depth depending on the ion energy.

trons. The fluence could be tuned by varying the irradiation time and fission power of the reactor. The sample Set S1 consists of pieces of a HPSI wafer purchased from CREE that was cut and irradiated with fluences from $\Phi_N = 4 \times 10^{15}\,\mathrm{cm}^{-2}$ to $\Phi_N = 8.5 \times 10^{18}\,\mathrm{cm}^{-2}$. The irradiation was performed in the chambers DBVK and DBVR at the BER II reactor at the Helmholtz-Zentrum Berlin. In case of SiC the crystal damage caused by neutrons with an energy below 0.18 MeV is neglectably small [82]. Hence, the displacement of thermal neutrons is not counted in the fluence calculation, but only epithermal and fast neutrons are considered.

Two additional samples N1 and N2 were cut from a HPSI wafer purchased from Norstel and irradiated in the TRIGA Mark II fission reactor (General Atomics, San Diego) of the Atominstitut, TU Wien [53]. The neutron energies in the TRIGA reactor are distributed evenly in the range between 100 eV and 100 MeV, with a peak in flux density around 2.5 MeV followed by a sharp cut-off [83] [84]. Again, only epithermal and fast neutrons above 0.18 MeV are considered for the fluence.

The measurement on two wafers from different manufacturers allows a comparison of the quality of the wafers and investigates both the generality of the results as well as the extent of wafer quality on the spin coherence.

3.2.2. Electron irradiation

As in case of neutron irradiation all samples were cooled during irradiation to avoid sample heating. For the sample series S2 of electron irradiated samples a HPSI wafer was purchased from Norstel, cut and irradiated with 2 MeV electrons in a fluence range from $\Phi_e = 1 \times 10^{17}\,\mathrm{cm}^{-2}$ to $\Phi_e = 1 \times 10^{18}\,\mathrm{cm}^{-2}$. The irradiation was performed at the electron beam irradiation facility at QST Takasaki (Japan). One piece was left pristine, with an as-grown V_{Si} concentration of $2 \times 10^{13}\mathrm{cm}^{-3}$. Another piece was irradiated with a varying electron energy of 1 MeV and a fluence of $\Phi_e = 1 \times 10^{17}\mathrm{cm}^{-2}$.
Furthermore, two samples were irradiated with electron energies of 20 MeV (sample E1) and 25 MeV (sample E2) at the electron accelerator ELBE in HZDR (Germany). The beam was extracted through a 300 μm Beryllium vacuum window and passed 150 mm through air before hitting the sample. The incident beam distribution and the small angle scattering in the vacuum window and air leads to a Gaussian shaped beam distribution on the sample. The beam profile was measured at the position of the sample with a Roos ionisation chamber (IC)N34001. The certificate calibrated IC and a Faraday cup were used for the dose and current calibration. From the profile measurement, the irradiation parameters were deduced. In order to monitor the current stability of the electron gun as well as dark current contributions the edge field of the beam was constantly measured and stabilized during the irradiation.

3.2.3. Proton irradiation

In contrast to the aforementioned methods proton irradiation does not create homogeneously distributed crystal damage. The passage of accelerated ions through a crystal and their displacement energy deposition location is governed by the interactions described by the quantum mechanical Bethe Bloch equation for charged heavy particles [85]:

$$-\frac{dE}{dz} = \frac{4\pi n Z^2}{m_e c^2 \beta^2}\left(\frac{e^2}{4\pi\epsilon_0}\right)\left[ln\left(\frac{2m_e c^2\beta^2}{I\left(1-\beta^2\right)}\right) - \beta^2\right] \tag{3.1}$$

Here, E is the Energy of the Ion, z is the distance travelled through the crystal, n is the electron density of the material, e the electron charge, Z the multiple of the electron charge, m_e the electron mass, $\beta = v/c$, where v is the velocity of the particle and c is the speed of light and ϵ_0 the vacuum permittivity. As can be seen, the particle energy is a function of the particle speed, which itself is a function of distance. The quantity $-dE/dz$ can be considered as linear electronic stopping power for a given particle type

and material. Fig. 3.2 shows the stopping power of protons penetrating a SiC crystal as a function of their kinetic energy plotted from the Bethe equation.

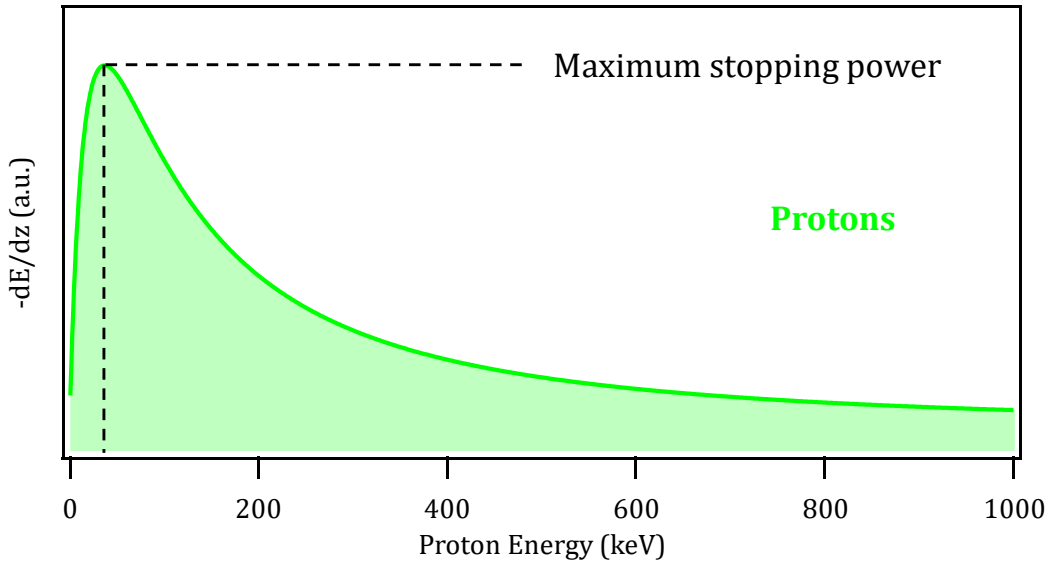

Figure 3.2.: Stopping power of protons as a function of proton energy (qualitative) according to the Bethe formula. The protons lose most of their energy right before they stop.

The stopping power and thus the energy transfer of the protons to the crystal depends strongly on the kinetic energy. If a fast proton enters the crystal, it is initially in the high kinetic energy range and is only slightly slowed down. While being slowed down to lower kinetic energy, it releases more energy per distance to the crystal. Right before it comes to a standstill, the stopping power reaches its maximum and the proton releases all its remaining energy to the crystal in one burst. Hence, protons create crystal damage nearly solely at the position of maximum stopping power, resulting in a layer of crystal defects at this certain depth. This position of maximum stopping power z_B is called the Bragg peak. The depth of the Bragg peak depends on the initial energy of the protons. Faster protons create a defect layer at greater depths, slower protons create layers closer to the surface.

Proton irradiation was done at the TIARA irradiation facilities in Takasaki, Japan. A piece of a 4H-SiC wafer purchased from CREE was placed on an aluminum plate and irradiated with a focused proton beam generated by a single-ended particle accelerator with a typical spotsize of $1\,\mu\text{m} \times 1\,\mu\text{m}$. The irradiation beam current was monitored by a beam dump (Faraday cup) connected to a picoampermeter before and after irradia-

tion. The exact layout of the samples P1 – P5 will be discussed in detail in the sections concerned.
To predict the depth of the Bragg peak and therefore the depth in which the defects are created, the well established software SRIM [86] was used. It calculates displacement statistics, lateral ion straggle and Bragg peak position by means of a Monte Carlo simulation.

3.3. Sample annealing

Irradiation creates a variety of crystal defects which potentially shorten the spin coherence of the V_{Si} defects. Using crystal annealing, the concentration of the unwanted crystal defects can be reduced. Hereby the crystal is heated and cooled down again in a controlled manner to temporarily provide lattice atoms with high thermal energy. Defects, like interstitials or Schottky defects, begin migrating through the crystal at these high thermal energies until e.g. an interstitial meets a free lattice place and the defect is removed.
In order to investigate the effect of annealing on the properties of V_{Si}, several samples were annealed after irradiation. The exact annealing protocols of the samples A1-A4 are discussed in chapter 7.
For annealing the samples were placed in a small boat-shaped piece of ceramic, which itself was then placed into a quartz tube furnace provided by the Bayerisches Zentrum für angewandte Energieforschung (ZAE Bayern). Annealing was performed under argon atmosphere to prevent chemical reactions of the samples with oxygen. The temperature was controlled and monitored by a Eurotherm PID controller.

3.4. Overview

In total, two systematically irradiated sample sets S1 and S2 were used in this work. In addition, several samples with varying properties were examined. The neutron irradiated samples are listed in tab. 3.1, the electron irradiated samples in tab. 3.2. The irradiation procedure and properties of the proton irradiated samples (P1 – P5) and samples H1 and H2 will be discussed in the sections concerned.

	Fluence Φ ($1/cm^{-2}$)	Em. Density N_V ($1/cm^{-3}$)
S1	$4 \times 10^{15} - 8.5 \times 10^{18}$	$1 \times 10^{14} - 1.3 \times 10^{16}$
N1	1×10^{16}	2.5×10^{14}
N2	8×10^{16}	5.9×10^{14}
A1	1×10^{18}	1×10^{16}
A2	1×10^{18}	1×10^{16}

Table 3.1.: List of neutron irradiated samples. The emitter density was obtained via the PL measurements presented in 5.1

	Energy MeV	Fluence Φ ($1/cm^{-2}$)	Em. Density N_V ($1/cm^{-3}$)
S2	2	$1 \times 10^{17} - 1 \times 10^{18}$	$3.9 \times 10^{14} - 9 \times 10^{15}$
S2	1	1×10^{17}	1.5×10^{14}
S2	-	-	2×10^{13}
E1	4.9	9×10^{17}	6×10^{15}
E2	4.9	1×8^{16}	4.8×10^{14}
A3	4.9	1×10^{18}	6.1×10^{15}

Table 3.2.: List of electron irradiated samples. The emitter density was obtained via the PL measurements presented in 5.1

4. Methods

This chapter covers the principles of the different measurement techniques, as well as the setups used. Five measurement techniques were utilized in this thesis:

- **Photoluminescence spectroscopy** was used to measure PL spectra of the V_{Si} defects and determine the V_{Si} density.
- **PL scans and photon-antibunching** were used to resolve proton beam written defect structures and identify luminescent spots as single V_{Si} defects.
- **EPR** was used to determine the density of V_{Si} defects.
- **cwODMR** was used to identify the V_{Si} defects and find the resonant transitions.
- **pODMR** was used to explore the coherence properties of the V_{Si} defects.

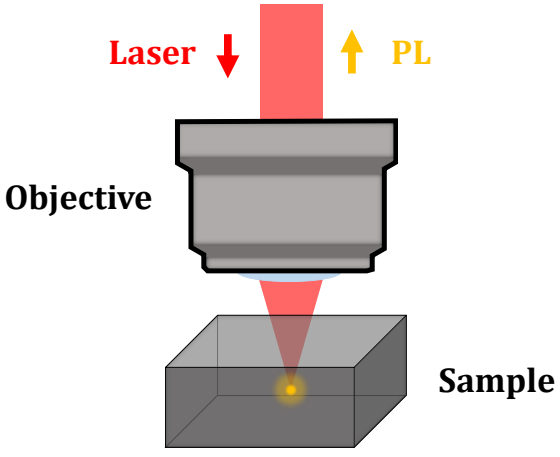

Figure 4.1.: Schematic representation of a confocal measurement setup. Instead of observing a complete image at once, as is the case with a conventional microscope, confocal microscopy always observes only a small area in the focus of the objective. In the case of V_{Si} defects, they are excited in the area of the laser focus. The PL is collected by the same objective.

Apart from EPR all measurements were obtained with a confocal geometry, where the excitation laser light was focused through an objective onto the sample as shown in fig. 4.1. In contrast to classical microscopy, where a full image of an object is taken, confocal microscopy at any time only probes one distinct small volume in a sample. This is at the location of the microscope objective focus, where the laser light is focused. Hence, the source of PL coincides with the microscope focus and the PL is captured by the objective again. It can afterwards be separated from the laser light and guided through a pinhole before it is detected.
Depending on the objective, confocal microscopy can very precisely probe a desired, small volume in a sample. Thus, it is possible to measure e.g. spatially resolved down to single V_{Si} defects with very low background luminescence. In combination with an automatic stage this can be used to resolute profiles of the emitter density and proton beam written structures by scanning the sample with the laser focus.

4.1. Photoluminescence spectroscopy

As discussed in 2.2.3, excited V_{Si} defects emit PL in the NIR range when relaxing into the ground state. For the PL measurements in this thesis the commercial confocal micro Raman spectrometer LabRAM HR800 from HORIBA (see fig. 4.2) was used.

In this setup excitation is accomplished with a 632 nm HeNe laser that is focused via a 100X magnifying Objective onto the sample. The confocally collected PL is seperated from scattered laser light by a dichroic mirror. Subsequently, the PL is guided into the direction of a spectrometer. A lense and a small pinhole are mounted in front of the detection to increase the resolution. The spectrometer is in Czerny-Turner configuration with two available gratings (600 or 1800 grooves/mm) and 0.8 m focal length. The detector is a peltier-cooled silicon based charge coupled device (CCD). The detectors spectral sensitivity profile is taken into account by the measurement software LabSpec. For low temperature measurements an optically accessible cold finger cryostat (MicrostatHe from Oxford Instruments) can be mounted to cool the sample. In this configuration the working distance of the 100X objective is too small and a long working distance objective 50XLWD is used. All PL spectra in this work were measured at this setup.

4.2. Single photon counting

The ability to measure single photons under time correlation is a powerful tool to determine the nature of a light source. A distinct feature of single photon sources is that

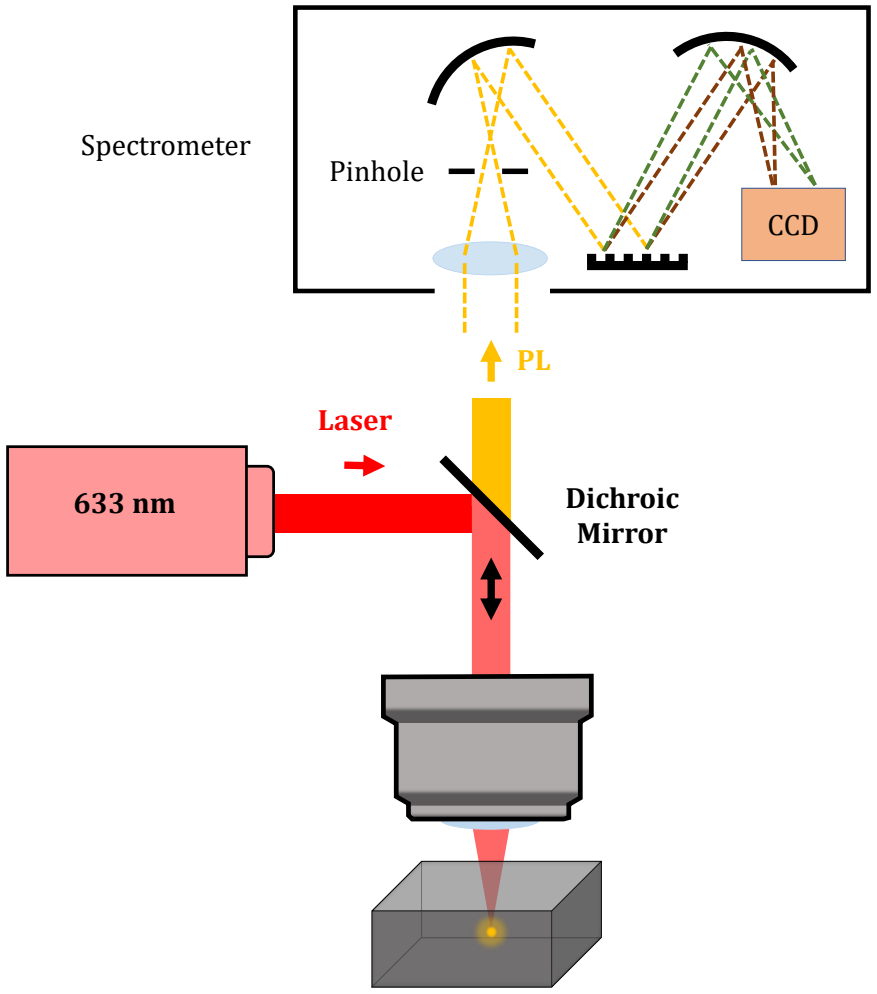

Figure 4.2.: Scheme of the LabRAM setup. All PL spectra in this thesis were measured at this setup. The laser is focussed onto a small collection volume through the objective. The PL from this volume is collected by the same objective, filtered from the laser light by a dichroic mirror and guided to a spectrometer in Czerny-Turner configuration.

after photon emission a subsequent photon can be emitted after a certain time period only. This behaviour is called anti-bunching and can be experimentally verified by time correlated photon detection [87], where the delay times between two consecutively detected photons are recorded. This can be mathematically described with the second order correlation function $g^{(2)}(\tau)$ [88]:

$$g^{(2)}(\tau) = \frac{\langle i(t)\, i(t+\tau)\rangle}{\langle i(t)\rangle^2} \tag{4.1}$$

where $i(t)$ is the number of detected photons for given time t and delay time τ. It describes the expected value for a second photon to be detected after a first one. The

anti-bunching manifests itself in a sharp minimum at $\tau = 0$ with $g^{(2)}(0) < g^{(2)}(\infty)$. Since it is typical for systems with a shelving state to show not only anti-bunching, but also bunching, the V_{Si} defects' $g^{(2)}$ function shows both features due to the presence of their metastable shelving state [53]. A $g^{(2)}$ function with bunching and anti-bunching can be fitted in the form

$$g^{(2)}(\tau) = 1 - (1 + c) \cdot e^{-|\tau|/\tau_1} + c \cdot e^{-|\tau|/\tau_2} \tag{4.2}$$

with fit parameters c and $\tau_{1,2}$ [53]. A fit of this form is schematically shown in fig. 4.3.

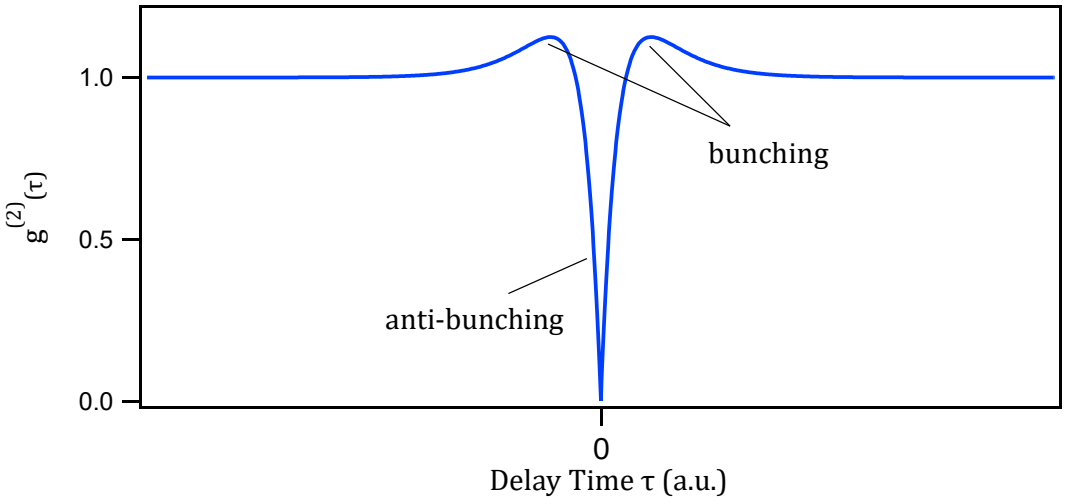

Figure 4.3.: Second order correlation function for quantum emitters featuring bunching and anitbunching. Qualitative $g^{(2)}$ function of a single photon emitter. The criterion for a single photon emitter is a bunching dip below $g^{(2)}(0) = 0.5$. Quantum systems with a shelving state, like the V_{Si} defects, additionally show bunching.

Not only isolated single photon emitters, but also other quantum mechanic systems can show anti-bunching in their correlation function. The number n of quantum emitters in a system determines the value of $g^{(2)}(0)$:

$$g^{(2)}(0) = \frac{\langle n(n-1)\rangle}{\langle n^2\rangle} \tag{4.3}$$

For single photon emitters with $n = 1$ this leads to a minimal value of the $g^{(2)}$ function of $g^{(2)}(0) = 0$. In general, $g^{(2)}(0) < \frac{g^{(2)}(\infty)}{2}$ is a sufficient experimental evidence that a light source is a single photon emitter, since detector dark count rate and background light increase $g^{(2)}(0)$.

4.3. Electron paramagnetic resonance

The electron paramagnetic resonance (EPR) technique is a generic term that covers many different methods and has many variants. The classical electron paramagnetic resonance (EPR) technique is a direct measurement technique, where the absorption of a resonant transition of a spin system is detected.
In EPR, radio frequency (RF) or microwaves (MW) are used to detect resonant transitions, while usually a magnetic field is applied. To conduct the EPR measurements, a SiC sample was placed into a resonator, by means of which RF waves of fixed frequency $f = 9.2\,\mathrm{GHz}$ were applied. In contrast to the ODMR measurements, not the MW frequency but the magnetic field was swept. As discussed in 2.2.6, this leads to a change of the Zeeman splitting of the sublevels. At a certain magnetic field the applied MW frequency meets the resonance between the sublevels and MW are absorbed by the V_{Si} defects. Commonly, the derivative of the absorption curve is plotted in classical EPR.
Fig. 4.4 shows a typical EPR spectrum of the V2 V_{Si} defect in SiC. Three different transitions can be observed.

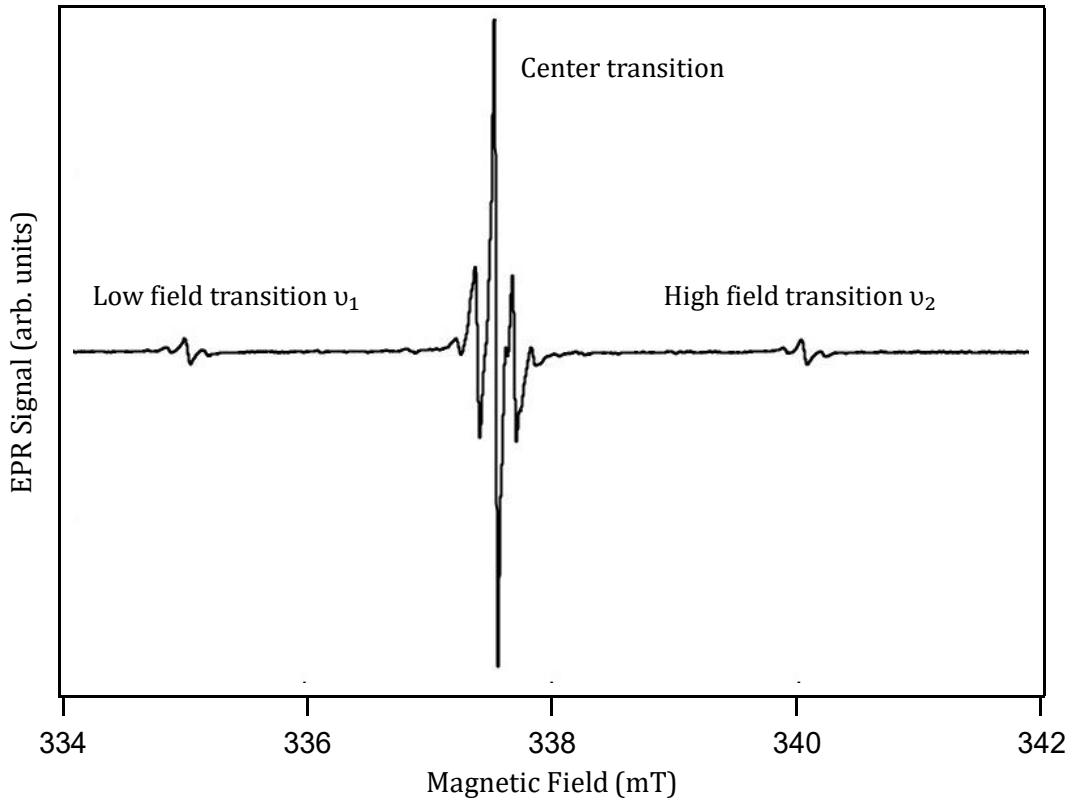

Figure 4.4.: EPR spectrum of V_{Si} defects in SiC. The absolute number of V_{Si} defects can be derived from the side transitions.

The center transition corresponds to $|-1/2\rangle \rightarrow |-1/2\rangle$ superimposed with a variety of spin active systems with $g = 2$. The side transitions, called low- and high-field transitions, can be attributed to ν_1 and ν_2 of the V_{Si} defect, respectively. EPR represents a powerful measurement technique, widely spread in many research fields. In this thesis quantitative EPR was used to determine the total number of resonant spins inside SiC samples.

4.4. Optically detected magnetic resonance (ODMR)

Initializing and reading out a spin state is quite challenging, but this task has been tackled for several decades and the developments are immense. The pioneering work of Alfred Kastler on the optical spectroscopy of mercury atoms in a static magnetic field with the simultaneous application of a radio- frequency field in the 1950s led to the discovery of optically detected magnetic resonance (ODMR) [89]. ODMR is a variation of the electron paramagnetic resonance (EPR) and a collective term for double magnetic resonance methods in which detection takes place in the optical frequency range and not at the actual resonance frequency. It is an indirect detection method, where, as opposed to the microwaves used in the detection of classical EPR spectrometers, the detected signal can be fluorescence, phosphorescence, absorption of light etc. There are various possibilities for ODMR measurements, based either on the change in frequency of an optical transition associated with different spin orientations or, like in case of V_{Si} defects, on the spin dependent PL due to selection rules and transition rates. An advantage over classical EPR is the high detection sensitivity for photons in the optical range compared to microwave photons. The option of selecting a suitable excitation wavelength, e.g. at the ZPL of the V_{Si} defect, also distinguishes it from other EPR methods. Furthermore, ODMR can be measured confocally, which provides the possibility of measuring ODMR spatially resoluted. High sensitivity and spatial selection hence enable ODMR profiles of samples as well as measurements of single isolated spin systems. Commonly, a magnetic field is applied to conduct ODMR measurements. In this work, only zero field ODMR and low field ODMR up to 15 mT were performed. In the following continuous wave (cw)ODMR on V_{Si} defects is described. In this section $|\pm 1/2\rangle$ and $|\pm 3/2\rangle$ refer to the spin sublevels of the ground state $|GS\rangle$.
The basic process of the ODMR measurement on V_{Si} defects is their optical pump mechanism. An ODMR experiment can be divided in the three typical stages of quantum operations: Initialization of a system, manipulation and read out. When excited

with a laser, a V_{Si} defect is optically pumped into the $|\pm 1/2\rangle$ spin sublevel, which represents the initialization of the spin system. To manipulate the spin state of the V_{Si} defect, a radio frequency (RF) field in resonance to the transition from the $|\pm 1/2\rangle$ to the $|\pm 3/2\rangle$ sublevel is applied. For V2, this RF frequency is 70 MHz according to the ZFS. By absorbing a RF photon, a transition between $|\pm 1/2\rangle$ and $|\pm 3/2\rangle$ is induced. Since V_{Si} defects in the $|\pm 3/2\rangle$ sublevel have a stronger PL emission, the current spin state can be read out optically via PL.

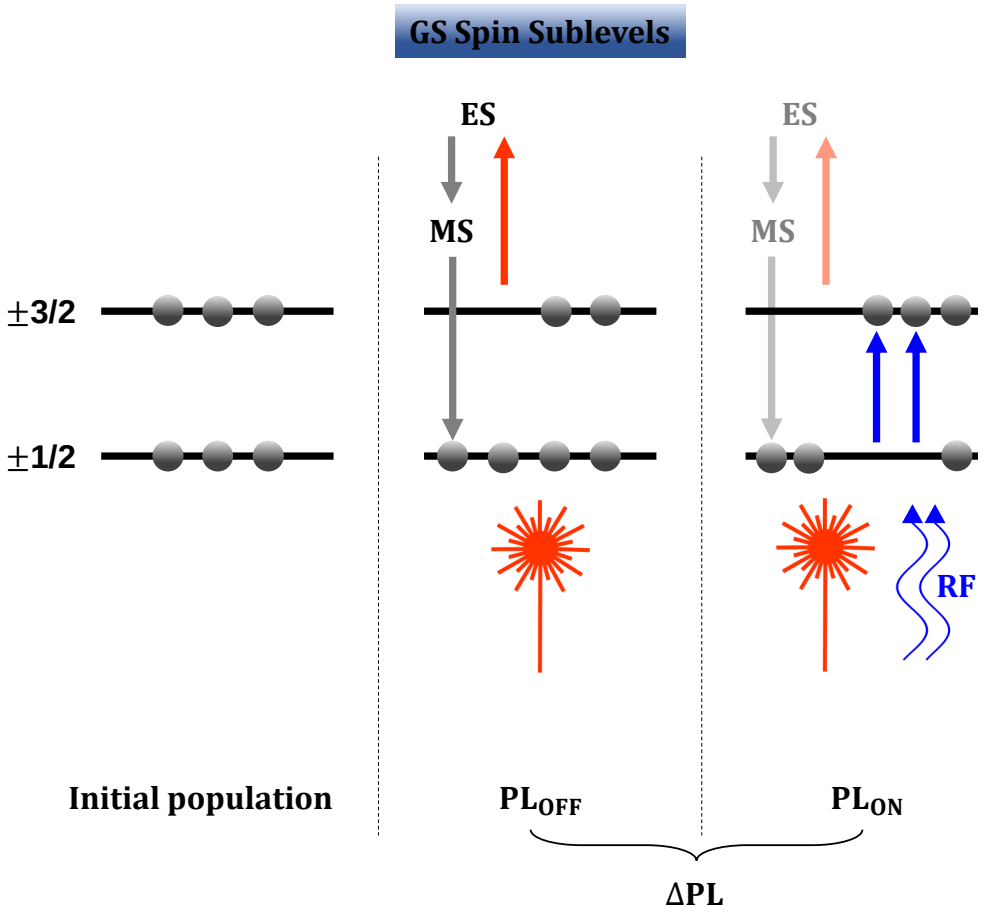

Figure 4.5.: Principle of ODMR of a V_{Si} ensemble. Resonant transitions between the spin sublevels are stimulated by applied RF waves after the V_{Si} defects are optically pumped into the $|\pm 1/2\rangle$ state. A transition from the $|\pm 1/2\rangle$ sublevel into the $|\pm 3/2\rangle$ sublevel results in an increased PL emission, which is detected.

All of the ODMR measurements in this work were performed on ensembles of V_{Si} defects, where a statistical approach is necessary. Fig. 4.5 schematiclly shows the population of the ground state spin sublevels of the V_{Si} defect ensemble during cwODMR. A grey point on the $|\pm 1/2\rangle$ level represents a vacancy in this spin state, the same applies for a grey circle on the $|\pm 3/2\rangle$ level. Without any interaction, the population difference

between $|\pm 1/2\rangle$ and $|\pm 3/2\rangle$ is Boltzmann distributed. Due to the small ZFS the levels can be assumed evenly populated. With optical excitation of the V_{Si} defects the $|\pm 1/2\rangle$ has a higher population due to optical pumping. The population difference that can be achieved via optical pumping depends on various parameters, like the defect density, the crystal quality, excitation and MW power, isotope density, temperature etc. [55]. It is a very important property with regard to the development of a MW amplifier. Additionally to the continuous optical excitation, the RF field is applied. Since $|\pm 1/2\rangle$ is higher populated due to optical pumping, more transitions from $|\pm 1/2\rangle$ to $|\pm 3/2\rangle$ are induced than from $|\pm 3/2\rangle$ to $|\pm 1/2\rangle$. Hence, an applied resonant RF field leads to an increased population of $|\pm 3/2\rangle$ and higher PL emission.
For the cwODMR measurements in this thesis the MW frequency was swept and the PL was detected with RF switched on (PL_{on}) and off (PL_{off}) several times for each applied RF frequency with a Lock-in amplifier. The change $\Delta PL = PL_{on} - PL_{off}$ of the PL is plotted against the frequency. This results in a peak at the resonance, as can be seen in fig. 4.6.

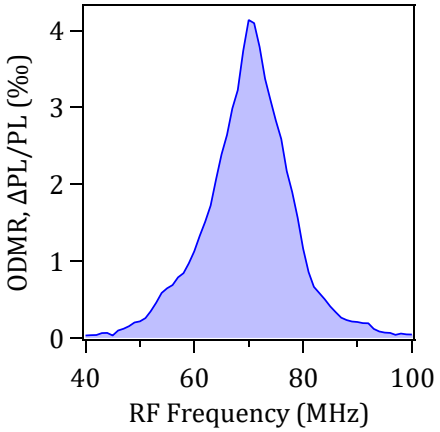

Figure 4.6.: ODMR spectrum of V_{Si} defects in a neutron irradiated sample. The resonance peak occurs at the posistion of the ZFS.

The ODMR spectrum serves as a fingerprint of a defect, since it directly shows the energy of the ZFS. A resonance peak at 70 MHz serves as evidence for the existence of V2 V_{Si} in the measured sample.

4.5. Pulsed ODMR

A crucial characteristic of crystal defects with potential regarding quantum applications are their coherence properties. More precisely, the spin-lattice relaxation time T_1 and the spin-spin coherence time T_2 are decisive factors in terms of usability. To explore the coherence properties of V_{Si} defects in this work, pulsed ODMR (pODMR) with

established pulse sequences well known from NMR was used. Laser and RF pulses are applied to control the V_{Si} defects' spin states.
Analogous to cwODMR every pulse sequence can be devided in three steps:

- The **initialization** of the V_{Si} defects' spins is achieved by means of optical pumping via a laser pulse.
- The **manipulation** of the V_{Si} defects' spins happens via RF pulses.
- The **read out** of the current spin state is attained via detection of the PL intensity.

The RF pulses are created using an RF switch Mini-Circuits ZASWA-2-50DR+. To create the laser pulses, an acousto optic modulator (AOM) is placed in the path of the excitation laser beam. This is schematically presented in fig. 4.7

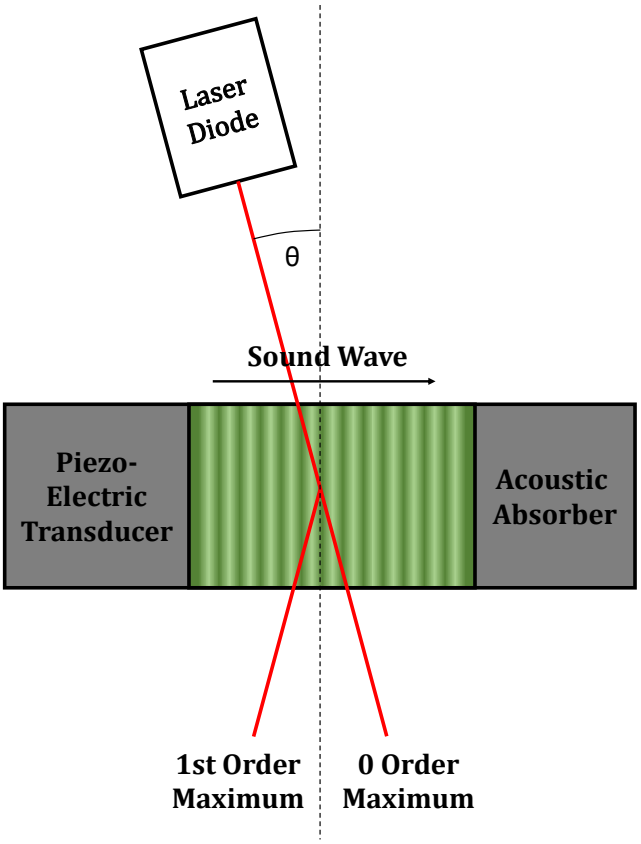

Figure 4.7.: Scheme of an acousto optic modulator (AOM). Density fluctuations in a quartz lattice caused by a sound wave create an optical grid. Scattering of the incoming laser beam on this grid results in the presence of maxima of higher order. These reflexes can be switched on and off very precisely by switching on and off the sound wave.

A piezo electric transducer produces an ultrasonic wave in a quartz crystal, which is absorbed by an acoustic absorber. The sound wave induces a periodic deformation of

the crystal with layers of different density. These density variations cause a periodic variation of the refraction index. Hence, the quartz crystal can be seen as optical grid, when the ultrasound is switched on. Analogous to Bragg scattering, there is positive interference at an angle θ depending on the wavelength of the laser light. A first order maximum occurs at an angle double the angle of incidence 2θ. This maximum is only present with the transducer being switched on. Using the first order maximum for optical excitation, it is thus possible to switch the laser beam on and off very fast and create very sharp laser pulses.
In the following, pODMR is explained on the example of the pulse sequence applied to measure Rabi oscillations. Every two level quantum mechanic system driven with a resonant force field performs Rabi oscillations. In case of V_{Si} in SiC this resonant force is the B_1 field of the RF waves. Fig. 4.8 shows a segment of the pulse sequence used in this work to measure Rabi oscillations of a V_{Si} ensemble.

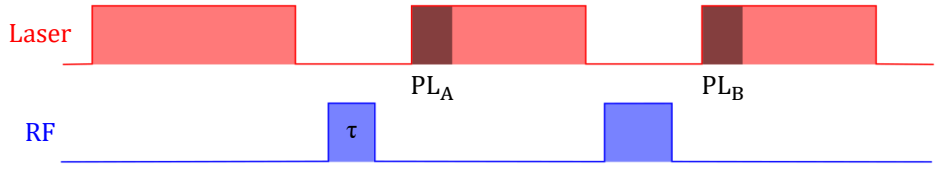

Figure 4.8.: Segment of the pulse sequence applied to obtain rabi oscillations in pODMR experiments. The complete pulse sequence consists of many segments of this kind with the length τ of the first RF pulse of every segment being increased

The segment contains two laser pulses of constant length and two RF-pulses, with one of them being increased at every iteration (For a better understanding the last laser pulse of the previous segment is also shown). The pulse lengths are not to scale, the RF pulses have typical lengths of τ = 100 ns, the laser pulses a constant length of 10 μs. The first laser pulse initializes the V_{Si} defect ensemble into the $|\pm 1/2\rangle$ sublevel. After the laser is switched off, the RF pulse is switched on. In contrast to cwODMR, the RF frequency is not swept, but fixed at the resonance between $|\pm 1/2\rangle$ and $|\pm 3/2\rangle$. Consequently, the RF wave pulses induce transitions between these two sublevels, while the polarization can be read out via the ODMR contrast.
The laser pulses have two functions: Firstly to initialize the system for the next segment and secondly to read out the spin state via PL after each segment. Therefore, the PL is monitored in the first moments of each laser pulse. The time window for this is typically 1 μs.
The complete pulse sequences used in this work consist of many of the segments shown

in fig. 4.8, with τ being increased from a minimal length to a maximal length. The sequences used for the Rabi measurements in this work consisted of 400 segments. For each RF pulse length two values of PL are recorded, one after the iteratively increasing RF pulse PL_A and another one as reference after a RF pulse with constant pulse length PL_B.
While measuring, the sequence was run over and over again and the values of PL_A and PL_B were integrated. Successively, the ODMR contrast
$\Delta PL/PL = (PL_A - PL_B)/(PL_A + PL_B)$ was calculated which corresponds to the spin polarization. To display the time resolved spin polarization, the ODMR contrast was calculated for each RF pulse length τ.
The measurement of Rabi oscillations is a demonstration of coherent control of the system concerned. Additionally, they provide the possibility to determine the pulse lengths needed for advanced pulse sequences to measure T_1 and T_2. They hence represent a fundamental measurement recurring in the upcoming chapters.

4.6. Experimental ODMR-setup

The cwODMR, pulsed ODMR, as well as single photon counting and PL scans were carried out with a home-built setup with home-written software. Its scheme is presented in fig. 4.9. The setup is a very versatile confocal setup and can be adapted for each of the three measurement techniques. At first the configuration for cwODMR is explained.

For optical excitation, the beam of a 785 nm laser diode from Thorlabs (LD785-SE400) is coupled into a 50 μm optical fibre and directed into an optical tower made of Thorlabs cubes. Behind the fiber a lense is mounted to make the divergent beam parallel. It is reflected on a 45 ° mirror and passes a 45 ° 850 nm SP dichroic mirror before it reaches the objective. The beam is focussed onto the sample using a 10X objective (Olympus LMPLN10XIR), with the laser spot measuring approximately 10 μm in diameter. The laser power at the surface of the sample during the measurements was 10 mW. The PL is then collected through the same objective and separated from the scattered laser light by the dichroic mirror and two 800 nm long pass filters. Behind the filter it is coupled into a 600 μm optical fibre and detected using a Si avalanche photodiode (APD) (Thorlabs APD120A). The microwaves are generated by a signal generator (Stanford Research Systems SG384) and amplified by an amplifier (Vectawave VBA1000-18). They are applied to the V_{Si} defects by a 0.5 mm wide copper-stripline the sample is placed on. The MW are on-off modulated with 666 Hz and ODMR is detected using a Signal Recovery 7230 lock-in amplifier. The magnetic field B_0 is generated by a permanent

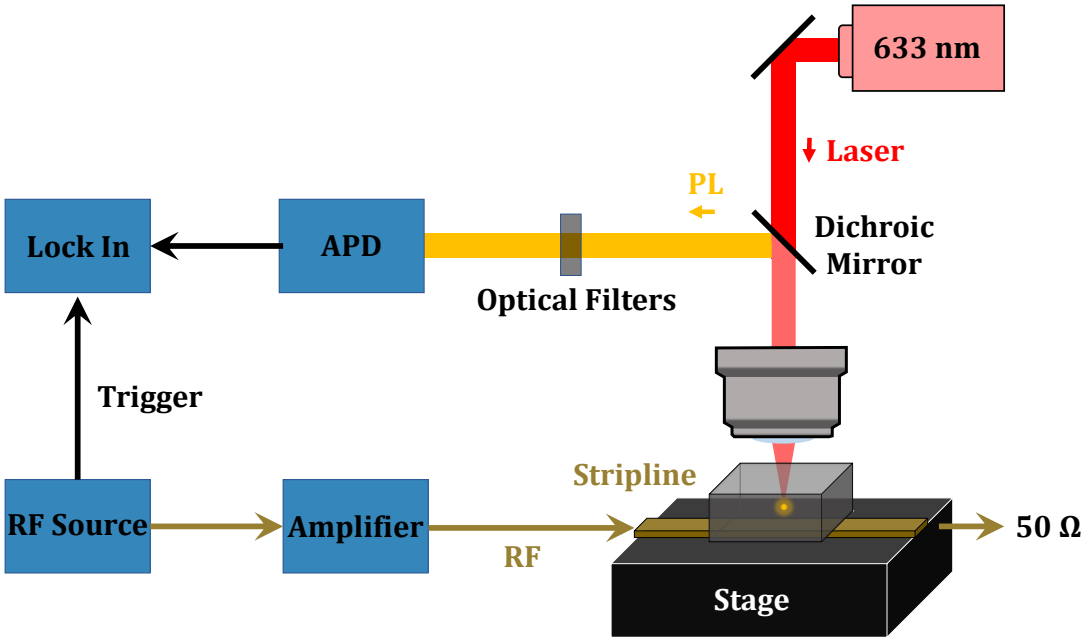

Figure 4.9.: Scheme of the home-built zfODMR setup. In addition to the confocal mode, it can be also used as classical microscope. All cwODMR measurements on the neutron and electron irradiated samples were performed in this configuration. The RF source modulated the RF waves with 666 Hz and the spin dependent change in PL is detected by the Lock-In, that received a trigger signal from the RF source.

magnet below the stripline.
For pulsed ODMR the same optical and MW components were used. The MW source is operated in continuous mode instead of on-off modulation and a MW switch (Mini-Circuits ZASWA-2-50DR+) is added between the MW source and the stripline to generate the pulses (see fig. 4.10).

The laser pulses are generated by an AOM (Opto- Electronic MT250-A02-800) before the laser is coupled into the fiber. The MW switches and the AOM are controlled by a PulseBlaster ESR-PRO 500MHz card from Spin-Core, that sends TTL pulses to the components. For signal processing an oscillator card from GaGe Compuscope is used.

For the single photon counting and PL scan measurements the APD is replaced by a much more sensitive APD from Laser Components able to detect single photons (see fig. 4.11). The signal is processed by the digital converter quTau from quTools, where pulses given out by the APD are counted and digitalized. For the measurement of the $g^{(2)}$- function, a beam splitter is placed between PL collection and detection and the photons are detected by two APDs (See fig. 4.12). The time correlation is processed by the digital converter unit quTau.

The self-built beam splitter consists of a birefringent, transparent dice mounted on rotatable stage as depicted in fig. 4.13. The entering light is separated according to its

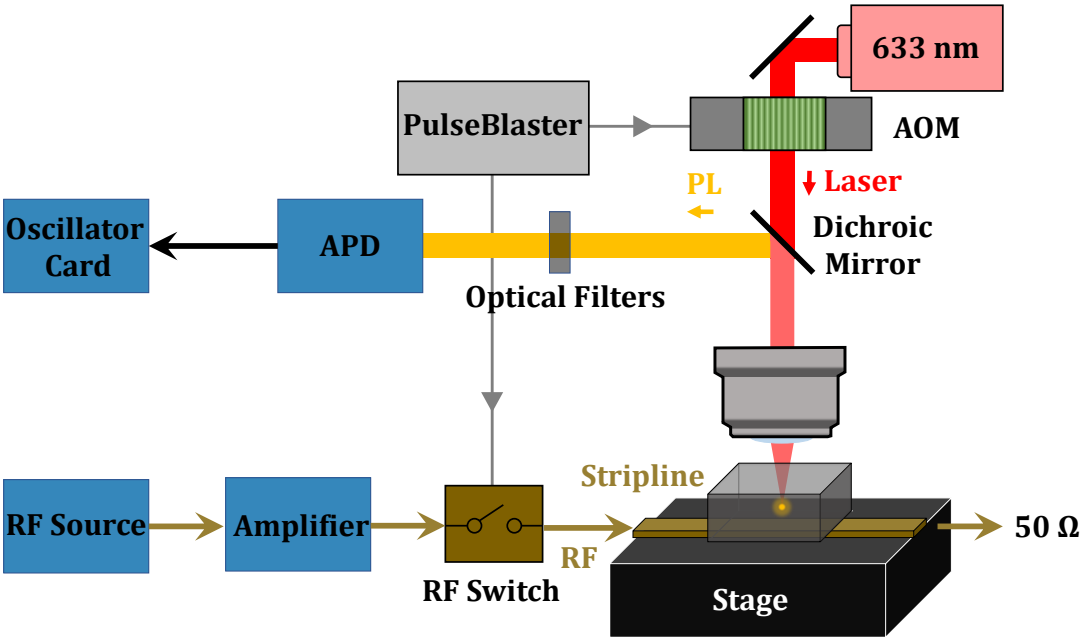

Figure 4.10.: Configuration of the zfODMR setup for pODMR. In contrast to the configuration for cwODMR, the RF source runs in coninuous mode, while a PulseBlaser card sends TTL pulses to the AOM and the RF switch that create the laser and RF pulses. Instead of a Lock-In, an oscillator card is used for signal processing.

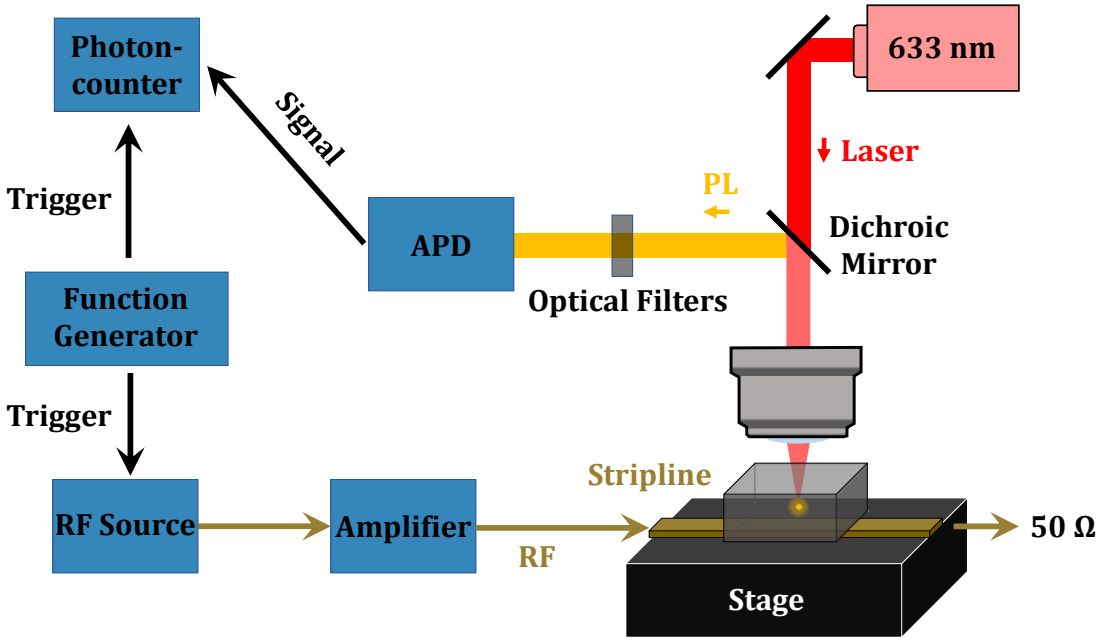

Figure 4.11.: Configuration of the Zf-Setup to conduct 3D PL scans. The objective was exchanged to a higher magnification to achieve better resolution and an APD able to detect single photons was mounted. The signal was processed by a photon counting unit, which was, like the RF source, triggered by a function generator.

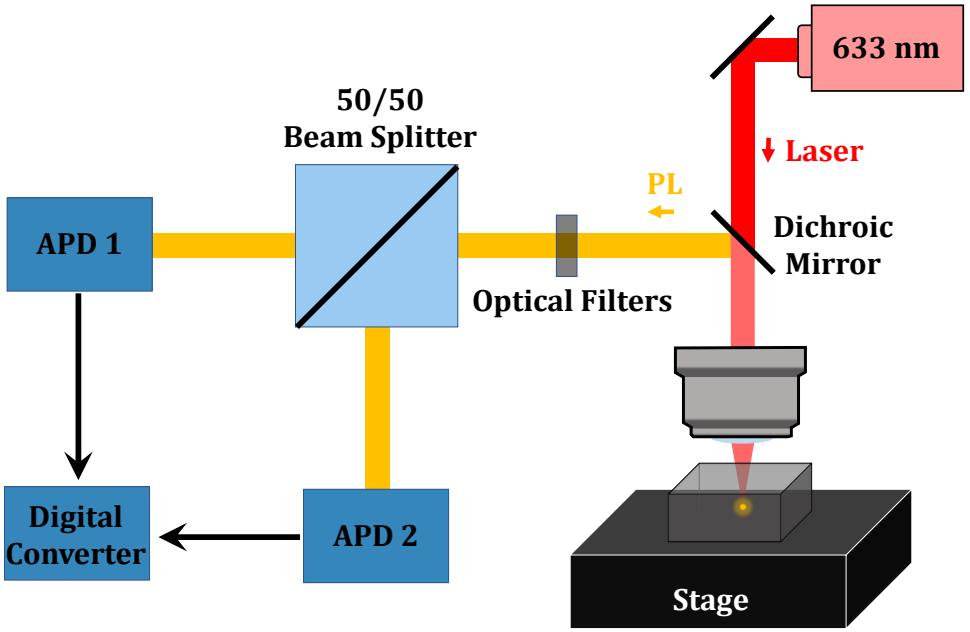

Figure 4.12.: Configuration of the Zf-Setup to measure Hanbury Brown- Twiss. The PL enters a 50:50 beam splitter before being detected in two APDs.

polarization. The two light beams with different polarization are then fiber coupled and guided to the APDs. The beam splitter is tuned to a 50:50 configuration by monitoring the signals of both APD while turning polarization filters before the fibres.

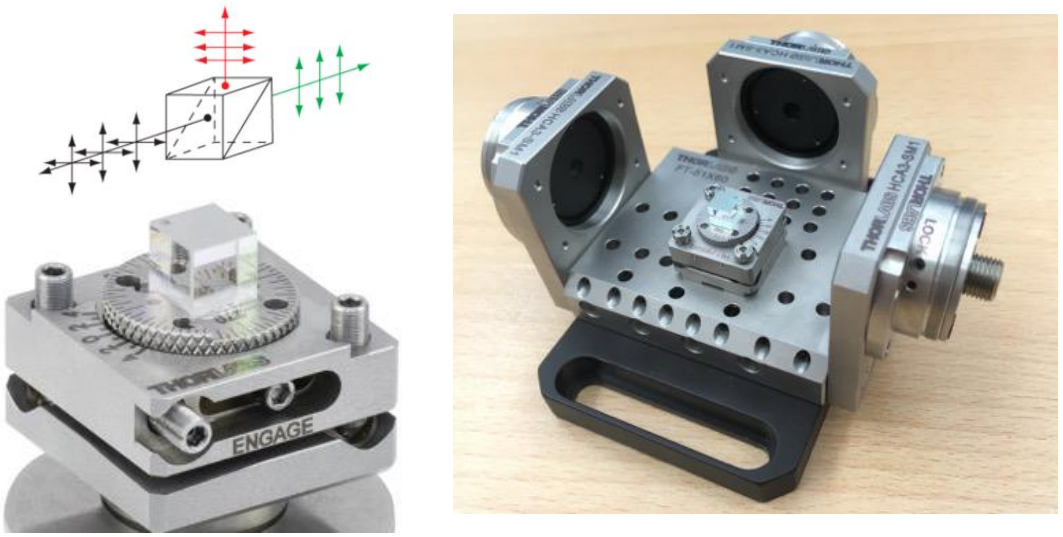

Figure 4.13.: Photograph of the fiber-coupled, self-built beam splitter with the birefringent crystal in the center.

5. Influence of irradiation on the silicon vacancy optical properties

A crucial property of a V_{Si} defect ensemble suitable for quantum sensing are its optical properties. A high PL emission leads to a low signal-to-noise ratio of the ODMR spectrum for given integration time. Since the magnetic field, temperature, etc. are derived from the ODMR spectrum, a low signal-to-noise ratio is required to perform quantum sensing within reasonable time scales. The intensity of the PL of the generated ensemble must therefore be considered and planned before the creation process.
It turned out that at low V_{Si} defect densities the PL intensity increases with the absolute number of V_{Si} defects and hence with the fluence of the chosen irradiation particle. Above a certain limit of the V_{Si} defect density, however, the PL emission is not only connected to the V_{Si} defect density. The behaviour is more complex and the number of active PL emitters is not monotonically increasing with the irradiation fluence.
In order to enable the prediction of the PL emission of a V_{Si} defect ensemble created by particle irradiation a systematic analysis of the emitter density as a function of the irradiation fluence is presented in 5.1. The density of optically active emitters is investigated for a wide range of electron and neutron fluences via PL spectroscopy and quantitative EPR. The results show an optimal fluence with a maximum density of optically active emitters.
Additionally, the targeted creation of V_{Si} defects by proton beam writing is investigated, necessary for e.g. the targeted creation of V_{Si} defects in nano scale electronic structures in 5.2. This offers the potential for quantum sensing on the nano scale featuring electrical read-out.
The results in this chapter allow the prediction of the V_{Si} defect location and emitter density created by particle irradiation for quantum sensing and related quantum applications. They were published in [80] and [90].

5.1. Emitter density in neutron and electron irradiated silicon carbide

In order to systematically analyze the influence of the V_{Si} density on the V_{Si} coherence for the three different irradiation particles, it is necessary to first determine the V_{Si} densities in the samples. To do so, it is assumed that the PL emitted by a sample is proportional to the number of created V_{Si} defects. However, most, but not all emitters are V_{Si}. Therefore, the obtained values are denoted as emitter density N_V. With the geometry of the defined collection volume of the confocal setup, the emitter density was subsequently derived.
In the following the emitter density as a function of the fluence is determined. In general, a higher irradiation fluence leads to more crystal damage. Naturally, it is expected that this results in a higher number of emitters and a higher PL emission. Already viewed with the naked eye, the crystal damage after irradiation is apparent: Fig. 5.1 shows neutron irradiated SiC samples of S1 for different irradiation fluences. The crystals irradiated with a lower fluence are transparent, while the crystals irradiated with a higher fluence are opaque due to the presence of optically active, absorbing crystal defects. In the next two sections, the determination of the emitter density by PL and EPR measurements is presented.

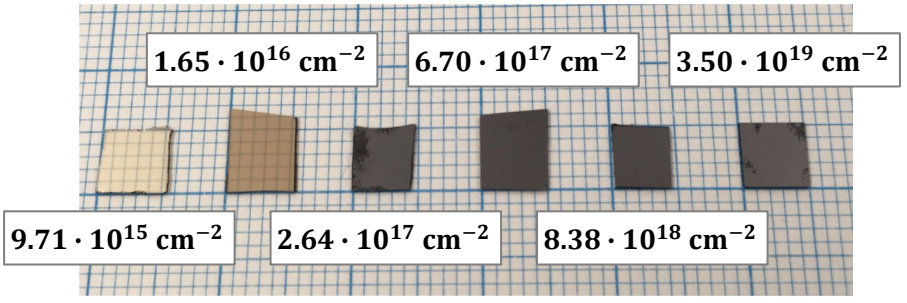

Figure 5.1.: Photographs of SiC samples irradiated with different neutron irradiation fluences. Samples irradiated with high fluences become opaque due to the creation of optically active defects.

5.1.1. Photoluminescence emission

In this section, the emitter density N_V in all samples determined from their PL emission is outlined. In order to do so, PL spectra were recorded at the LabRam setup with 633 nm excitation and compared to a reference sample. The basic principle here is that

the emitted PL is proportional to the number of emitting defects. For the integrated PL intensity, only the spectral range of the phononic side band (PSB) of the V_{Si} defects is considered.

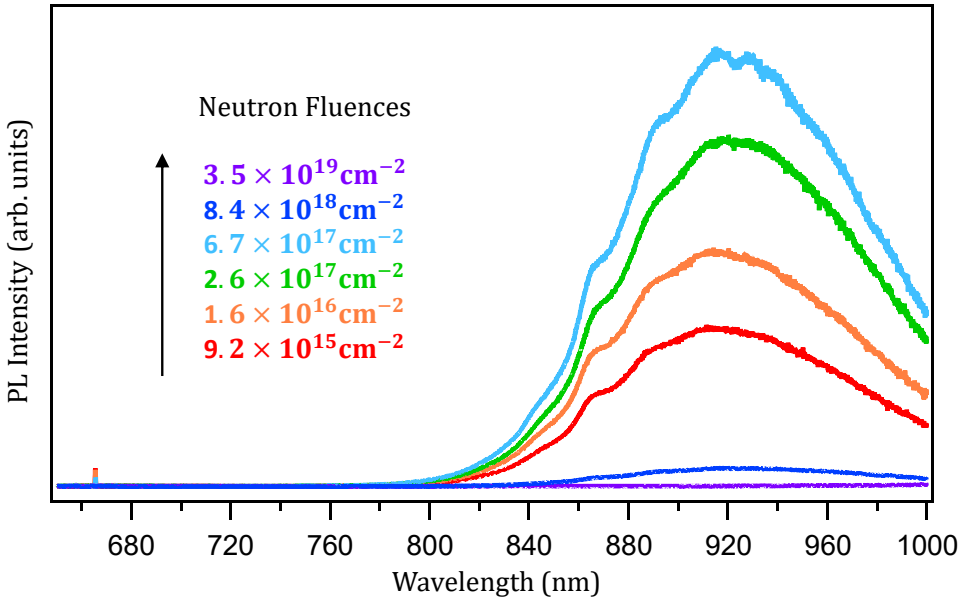

Figure 5.2.: PL spectra of V_{Si} defects for different neutron irradiation fluences. The PL emission increases with the fluence due to creation of emitters. From a certain emitter density on, non-optical relaxation becomes dominant and the PL decreases.

Fig. 5.2 shows the PL spectra of several neutron irradiated samples with different fluences. For low fluences, the emission is low due to only marginal crystal damage and corresponding low N_V. With increasing fluence, the PL increases as well, proving an increase of the generated emitter number. For very high fluences, the PL intensity drops rapidly. As indicated by this drop of PL at high fluences and is backed up by the results in 5.1.2, the assumption of a direct proportionality between created emitters and PL emission only holds for low fluences. For high fluences and defect densities the PL is reduced by non luminescent relaxation of potential emitters induced by spin-spin interactions. The spin-spin interactions also govern the spin coherence of the V_{Si}. As will be presented in 6.3, reasonably long spin coherence of V_{Si} created with neutron irradiation was only given in samples with $N_V < 10^{16}\,\mathrm{cm}^{-3}$. The experiments on the spin coherence were therefore performed in a range, where N_V and PL emission are assumed to be proportional and the determination of N_V via PL is valid. However, for the sake of completeness, the behaviour of the PL at high fluences is investigated in this section as well.

In previous works of our group, F. Fuchs et al. established a formula to calculate N_V as a funtion of the neutron irradiation fluence [53]:

$$N_V = C \cdot (\Phi_N)^{\alpha} \tag{5.1}$$

Here C is a constant and $\alpha \approx 0.8$. A sample from this work with known N_V was used as reference to calibrate the PL intensity. All PL measurements, including the one of the reference sample, were done in the confocal LabRam in one run.

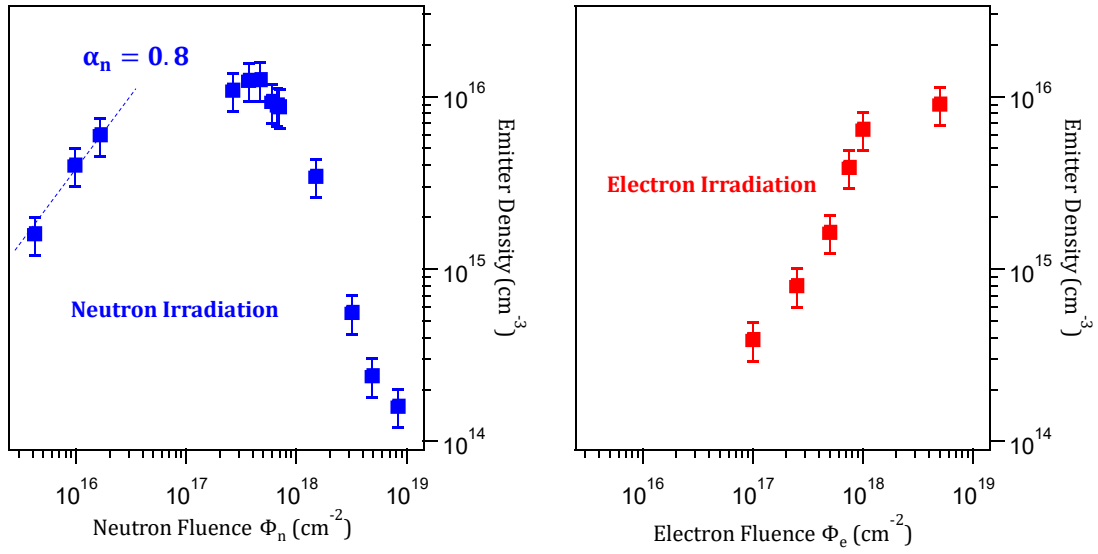

Figure 5.3.: left: Variation of the PL intensity and corresponding emitter density as a function of the irradiation fluence with epithermal and fast neutrons. **right:** Same as left, but for 2 MeV electrons. The dashed line is a fit of the form presented in eq. 5.1.

Figure 5.3 shows the integrated PL as a function of the neutron or electron irradiation fluence, measured in the sample sets S1 and S2. The blue dashed line is a fit to eq. 5.1. As pointed out in 3.2.1, only epithermal and fast neutrons are considered in the fluence. The energy of the electrons was $E_e = 2\,\mathrm{MeV}$.
For neutron irradiation, $\alpha_n = 0.8$ (dashed line) is in accordance with [53]. The maximum PL can be observed at $\Phi_{n,m} = 6.7 \cdot 10^{17}\,\mathrm{cm}^{-2}$ and the corresponding maximum emitter density is $N_{V,m} = 1.3 \cdot 10^{16}\,\mathrm{cm}^{-3}$. For increasing fluence, the aforementioned rapid collapse of the PL intensity is readily apparent due to the increasing density of defects other than V_{Si}. During irradiation, a plethora of defect types with many of them providing non-luminescent relaxation paths for the V_{Si} is created. This is called quenching and can be observed in all fluorescent materials. With high defect densities, the probability for another kind of defect to be in the vicinity of a V_{Si} defect increases

and thus the probability of quenching. This results in low PL emission for heavily irradiated samples. The density of potential emitters is therefore underestimated by the value of N_V determined via PL. In order to determine by how much, additional quantitative EPR experiments were performed on several samples. The results are presented in 5.1.2.
The samples irradiated with electrons demonstrate a qualitatively similar behaviour for low fluences, but no PL drop at high fluences occurs. The maximum PL is reached at the highest fluence of $\Phi_{e,m} = 4.0 \cdot 10^{18}\,\mathrm{cm}^{-2}$ and a corresponding emitter density $N_V = 1.0 \cdot 10^{16}\,\mathrm{cm}^{-3}$. From this it can be deduced that more electrons than neutrons are needed to cause the same crystal damage. This lower creation yield of electrons is to be expected due to their lower mass and preferred interactions with crystal electrons rather than crystal atoms, while the uncharged, heavy neutrons lose most of their energy in collisions with the atoms [91] [92].

5.1.2. Quantitative electron paramagnetic resonance

In order to examine the conformity of N_V determined via PL reduced due to quenching in strongly neutron irradiated samples with the actual density of potential emitters, quantitative EPR was measured on several samples. The typical EPR reference 1,3-bis(diphenylene)-2-phenylallyl (BDPA) – a molecular radical with one spin per molecule was used. The molecular weight is known and the sample weight was carefully measured for achieving an absolute spin standard. Fig. 5.4 shows the EPR spectra of the BDPA reference sample and the low field transitions of one neutron and one electron irradiated SiC sample. The spectra were obtained at room temperature in the dark with the same setup and same conditions to provide comparability. The low field transition was used, as at this magnetic field range no other EPR transitions were present which resulted in undistorted, background-free spectra. Both the transitions of the neutron irradiated SiC as well as the one of electron irradiated SiC show satellite peaks originating from hyperfine interaction of the V_{Si} defects with surrounding ^{29}Si and ^{13}C isotopes [55].

The absorption is proportional to the absolute number $n_{V_{Si}}$ of spins in the sample. It is given by the integral of the absorption spectrum $\xi_{V_{Si}}(B)$. By comparing it to a reference with known spin number, the absolute number can thus be determined. When considering the spin $S = 3/2$ of the V_{Si} defects, the spin number $n_{V_{Si}}$ is found by comparing the integrated absorption of the SiC sample to the integrated absorption spectrum $\xi_0(B)$ of the BDPA reference sample:

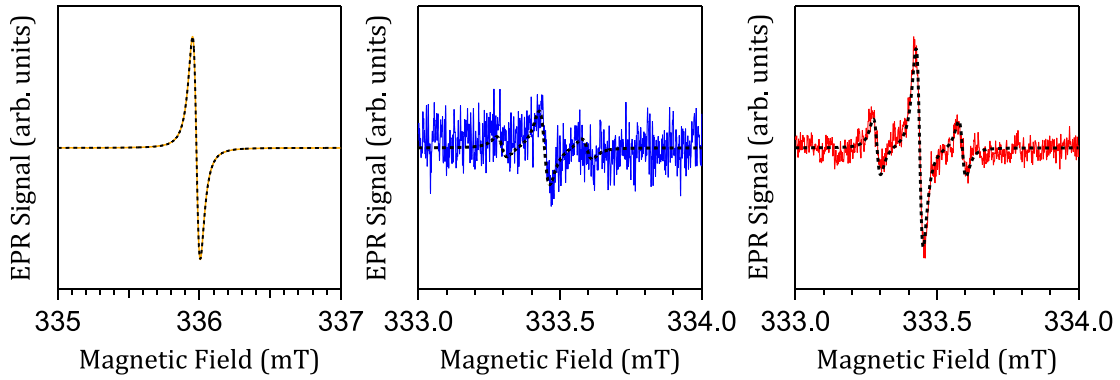

Figure 5.4.: Determination of the defect density $N_{V_{Si}}$ from quantitative EPR spectra at room temperature. **left:** Reference sample of molecular BDPA radicals with known absolute spin number $n_{\mathrm{BDPA}} = 3.6 \times 10^{17}$. **middle:** Low-field EPR transition of the V2 defect for a neutron irradiated sample irradiated with a fluence of $\Phi_n = 1.6 \times 10^{16}\,\mathrm{cm}^{-2}$ and corresponding defect density of $N_{\mathrm{V_{Si}}} = 4.5 \times 10^{15}\,\mathrm{cm}^{-3}$. The ratio of the double integrated spectral fits (dashed lines) yields absolute V2 defect numbers. **right:** Same as **middle** for an electron irradiated sample with $\Phi_e = 1 \times 10^{18}\,\mathrm{cm}^{-2}$ and $N_{\mathrm{V_{Si}}} = 8.6 \times 10^{15}\,\mathrm{cm}^{-3}$. The dashed lines are fits as described in the text.

$$n_{V_{Si}} = \frac{\int \xi_{V_{Si}}(B)\,dB}{3\int \xi_0(B)\,dB} \cdot n_0 \tag{5.2}$$

Since the EPR signals Ξ are recorded as the derivative of the absorption, they need to be integrated twice to find the total absorption:

$$n_{V_{Si}} = \frac{\int\int \Xi_{\mathrm{V_{Si}}}(B)\,dB^2}{3\int\int \Xi_0(B)\,dB^2} \cdot n_0 \tag{5.3}$$

The integral $\int\int \Xi_{V_{Si}}(f)\,dB^2$ was carried out with the fits of $\Xi_{V_{Si}}(B)$ represented by the black dashed lines in the spectra. The fits also consider the hyperfine peaks. From the total number of spins $n_{V_{Si}}$, the V_{Si} density $N_{V_{Si}}$ can be calculated as:

$$N_{V_{Si}} = \frac{n_{V_{Si}}}{V} \tag{5.4}$$

with V being the sample volume.

Figure 5.5 shows the emitter densities determined by PL, extended by the emitter densities obtained via quantitative EPR for both neutron and electron irradiated samples. The values for electron irradiated samples and samples irradiated with low neutron fluences correspond well. The values of $N_{V_{Si}}$ determined by quantitative EPR are higher than those of N_V determined via PL measurements for high neutron fluences. This is due to the fact that EPR directly measures the MW absorption. Effects such as PL absorption and especially quenching have no influence on the results. Therefore it

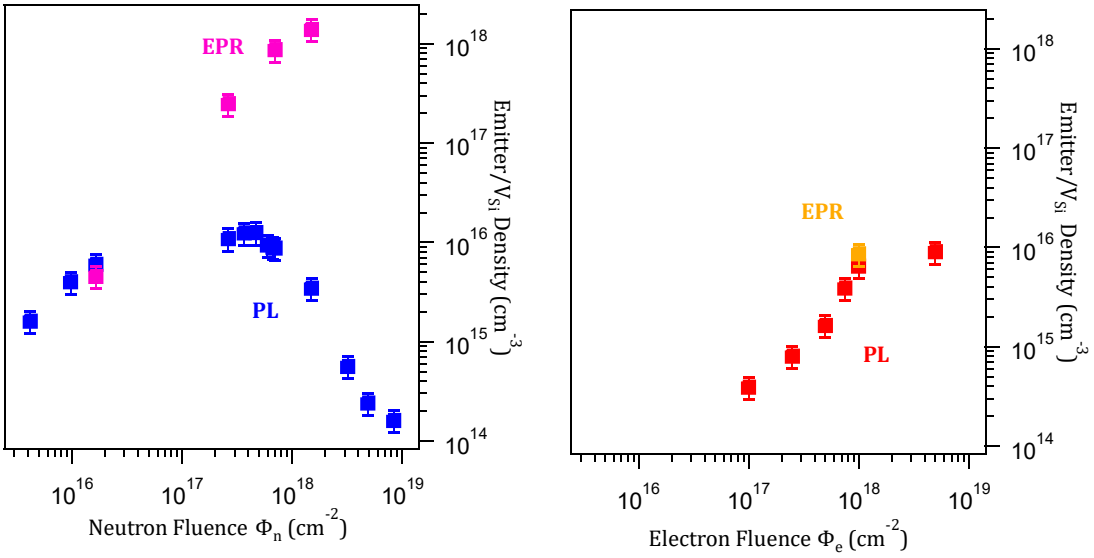

Figure 5.5.: N_V and $N_{V_{Si}}$ as a function of the irradiation fluence in samples irradiated with neutrons or electrons.

could also be expected that only the values of the densities at high neutron fluences differ. Only for these samples the quenching becomes such a dominant factor, that the density of potential emitters is dramatically underestimated in PL experiments. However, the density of actual emitters N_V is always precisely determined by PL measurements.

These findings are taken into account in the later chapters when comparing the coherence properties. The majority of the neutron irradiated samples examined with pODMR, however, were irradiated with low fluences in the regime where the emitter densities determined via PL and EPR show good correspondence.

5.2. Targeted creation of silicon vacancies

The production of hybrid quantum systems with V_{Si} defect spins integrated into electronic or opto-electronic circuits for on-chip manipulation is a goal of ongoing research. It is indispensable for the production of reasonably sized and electrically adressable sensors and devices that use the V_{Si} spin [23]. Spin-opto-electronic interfaces as well as electric control and read-out of V_{Si} have been demonstrated in recent years [93] [78] [94] [23]. In all these demonstrations the V_{Si} were created randomly in a crystal, with some being created inside an already existing electronic or photonic structure. It is rather a gamble whether a V_{Si} is generated at the desired position in the structure

or not. Many iterations are necessary to finally obtain a few structures where V_{Si} are generated at the right location. A method in which the generation of a few or even single V_{Si} is targeted is therefore highly desirable. The approach in this work is the displacement of Si atoms, not with electrons or neutrons as before, but with a focused ion beam, in this case protons. While the two transverse dimensions are controlled by the x-y position of a proton beam (PB), the lateral position can be controlled by the energy of the protons according to 3.2.3. This allows a deterministic, three-dimensional control of defect generation at the nanoscale. Furthermore, it provides a high degree of scalability from a high proton fluence creating a dense ensemble down to a small number of protons capable of creating isolated spins. The control of the location and the spin density are both prequisites for facilitating a targeted V_{Si} generation for the fabrication of spin-based quantum hybrid interfaces.
In 5.2.1 the creation of luminescent spots written with a PB is verified. Luminescent layers and a pattern were written into an ultrapure epitaxially grown SiC layer and revealed by confocal PL xy-scans. The PL of these was identified to be the one of V_{Si} defects. In 5.2.2 PB written V_{Si} spots with varying fluence and emitter density were scanned with nm resolution and the existence of single photon emission of an isolated V_{Si} was verified by means of a Hanbury-Brown-Twiss experiment. The results of this chapter were published in [80].

5.2.1. Three-dimensional proton beam writing.

In order to provide the possibility of V_{Si} creation at a desired position, controlled defect generation in all three spatial dimensions must be achieved. Thus, the first step from bulk to defect engineering was the creation of defect layers in a SiC crystal. For this purpose, a HPSI wafer was cut and irradiated with protons. Three pieces were irradiated with $E_1 = 1\,\mathrm{MeV}$ and the doses $\Phi_H = 1 \times 10^{11}\mathrm{cm}^{-2}$, $\Phi_H = 1 \times 10^{12}\mathrm{cm}^{-2}$ or $\Phi_H = 1 \times 10^{13}\mathrm{cm}^{-2}$ (samples P1−P3). Another piece was irradiated with two different energies $E = 1\,\mathrm{MeV}$ and $E = 2\,\mathrm{MeV}$ and dose $\Phi_H = 1 \times 10^{13}\mathrm{cm}^{-2}$ (sample P4). The samples were scanned in x-direction (transversal to the surface) and z- direction (lateral to the surface) after irradiation. The xz-scans of the three proton irradiated samples P1−P3 with $E_1 = 1\,\mathrm{MeV}$ are presented in fig. 5.6.

The scans show the formation of luminescent layers in all three samples at the same depth. The PL spectrum on the right side of fig. 5.6 of such an emitting layer shows the typical V_{Si} PL emission in the NIR. It is safe to say that the majority of emitters in the layers are V_{Si} defects. In that sense the PL scans with the APD show accurate mappings of the V_{Si} distribution, which will be verified by a cwODMR spectrum in section 6.4. Nonetheless, the emitted PL is filtered by a band pass before detection so that no light

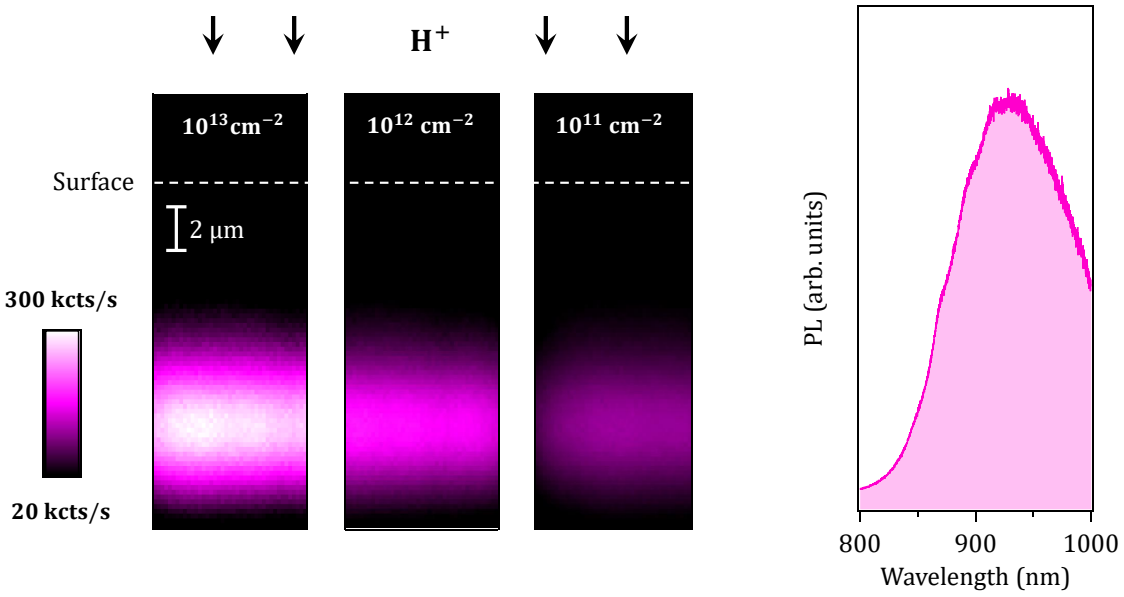

Figure 5.6.: Depth-dependent V_{Si} creation with PB writing. **left:** PL xz-scan of three SiC crystals irradiated with 1 MeV protons and decreasing fluence from left to right. **right:** PL spectrum of the emissive layer created with the highest fluence $\Phi_p = 10^{13}\,\mathrm{cm}^{-2}$. It emits the typical NIR PL spectrum of the V_{Si} defects.

of emitters in other spectral ranges is detected.
The connection between irradiation dose and induced crystal damage and hence brightness of the emitting layer is also evident from the xz-scans. It is recognizable that a stronger irradiated sample shows higher PL emission due to a higher number of irradiation induced emitters. In order to validate the predictability of the layer depth, sample P4 was irradiated with two proton energies. Additionally, the sample was coated with a 1 μm thin layer of the luminescent organic molecule poly-3-(hexylthiophene) (P3HT) to identify the sample surface. The PL xz-scan of sample P4 is presented on the left side of 5.7.

The irradiation with two proton energies resulted in the formation of two individual emitting layers of V_{Si} defects. The theoretical depths of the protons' Bragg peaks, obtained with Monte Carlo simulations used in the software SRIM, are calculated to $\mathcal{Z}_{\mathrm{sim}}(1\,\mathrm{MeV}) = 10.8\,\mu\mathrm{m}$ and $\mathcal{Z}_{\mathrm{sim}}(2\,\mathrm{MeV}) = 31.9\,\mu\mathrm{m}$. The depth of the layers in the experiment is derived from the profile of the PL xz-scan, as shown on the right of fig. 5.7 by measuring the distance of the V_{Si} layers to the P3HT-layer. It has to be mentioned, that the z-axis needs to be adjusted in all z-scans. When the motor of the stage moves 1 μm in z-direction, the laser focus travels 2.6 μm due to the refraction index $n = 2.6$ of SiC. The depth in the graph shows the travel distance of the laser focus and thus shows the actual position in the crystal. The layer positions obtained from the pro-

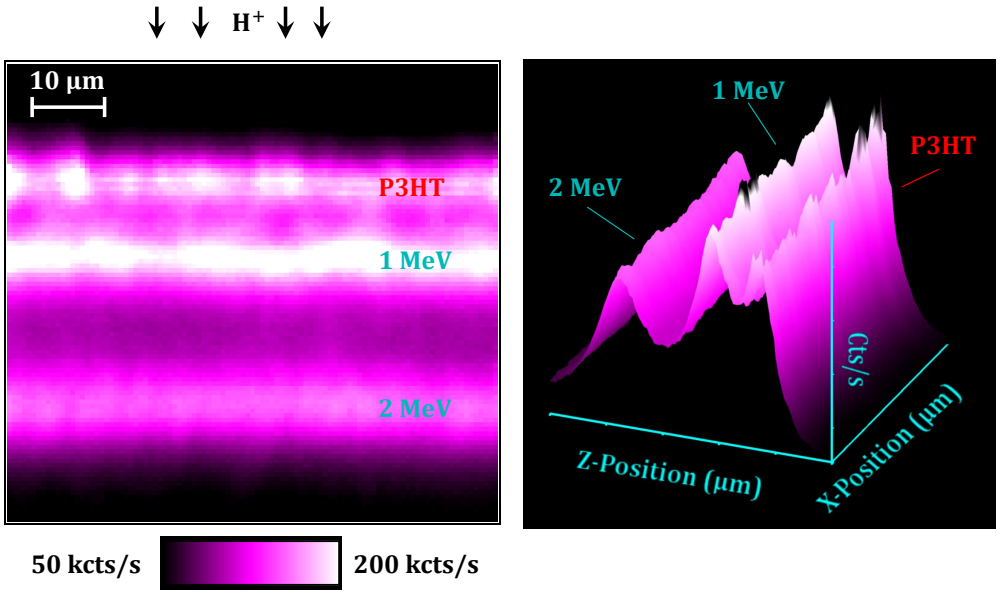

Figure 5.7.: Multi-energy V_{Si} layer creation with PB writing. **left:** PL xz-scan of a SiC crystal irradiated with 1 MeV and 2 MeV protons and coated with a layer of P3HT. **right:** Profile of the PL scan on the left to determine the depth and FWHM of the layers.

file of the PL scan are $\mathcal{Z}(1\,\text{MeV}) = 12 \pm 5\,\mu\text{m}$ and $\mathcal{Z}(2\,\text{MeV}) = 34 \pm 9\,\mu\text{m}$. These depths are in good agreement with the Monte Carlo simulations. The layers can therefore be attributed to crystal damage and V_{Si} creation at the depths of the Bragg peaks. This provides predictability of the depth of the created V_{Si}, which is a crucial factor for sample production.

The FWHM of the layers in the xz- scans is broadened due to the resolution limit of the objective. The layers are, in reality, much thinner. With the numerical aperture N.A. of the objective and the excitation wavelength λ, the optimal axial resolution of a confocal microscope can be calculated as

$$R_z = \frac{0.88\lambda}{n - \sqrt{n^2 - \text{N.A.}^2}}.$$

Here, n is the refraction index of the sample. For the ZfODMR confocal setup this gives an optimal resolution of $R_z = 4.9\mu\text{m}$. The FWHMs of the layer created with lower energy in the PL scans is $\mathcal{Z}_H(1\,\text{MeV}) \approx 11\,\mu\text{m}$ and the one of the layer created with higher energy is $\mathcal{Z}_H(2\,\text{MeV}) \approx 17\,\mu\text{m}$. This suggests that the confocal resolution of our setup in z-direction is approximately a factor of three above the theoretically achievable. The resolution in lateral direction can be calculated as

$$R_{xy} = \frac{0.51\lambda}{\text{N.A.}}.$$

This gives a lateral resolution of $R_{xy} = 0.5\,\mu$m for our setup.
After control in one dimension has been shown, the second step from bulk ensemble creation to defect engineering is the lateral control of the V_{Si} creation. This was achieved by using a focussed proton microbeam with a spot size of $1\,\mu$m and a position resolution of 15 nm. In such way, very detailed defect structures were created. A pattern was written in an ultrapure epitaxially grown SiC layer (sample P5). The proton energy was $E = 1.7$ MeV resulting in a calculated Bragg peak at $\mathcal{I}(1.7\,\text{MeV}) = 26\,\mu$m. The pattern design is shown in fig. 5.8.

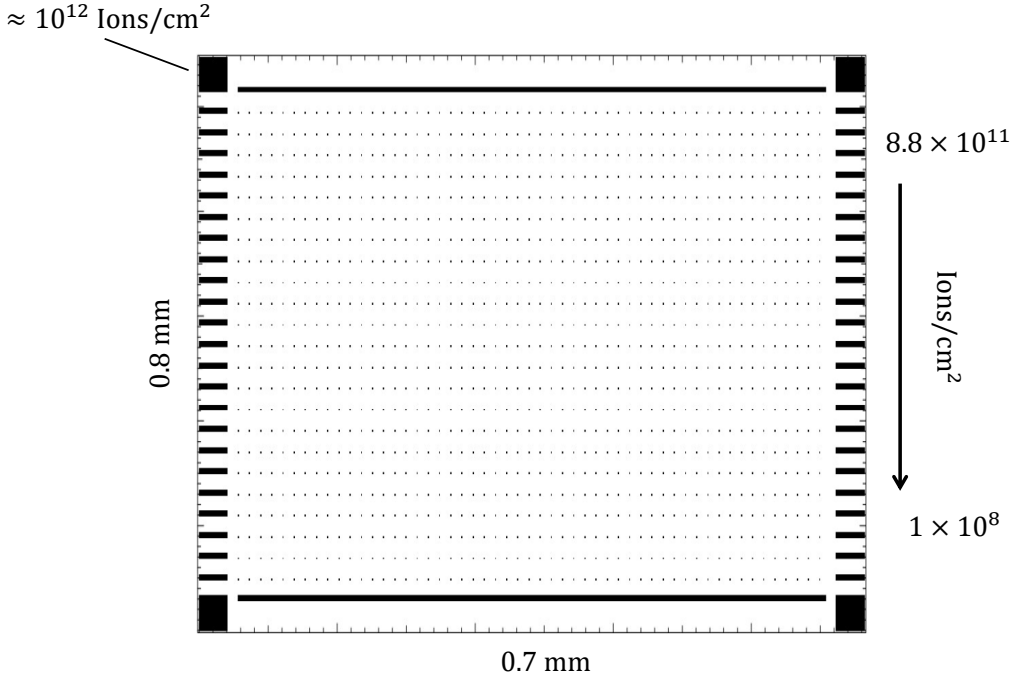

Figure 5.8.: Layout of the PB written pattern in sample P5. The black dots represent the irradiation sites. The sites at the top are irradiated with a higher fluence compared to the sites at the bottom. Markers with higher fluence are added for orientation.

It consists of several rows of proton beam written V_{Si} spots with a fluence gradient along the columns in each pattern. The patterns differ in the absolute values of the fluences. They are in the range of $1 \times 10^8 - 8.8 \times 10^{11}\,\text{cm}^{-2}$. Large markers with higher fluence $\approx 10^{12}\,\text{cm}^{-2}$ are written on the edges of the patterns for orientation.
An overview xy-scan of a complete pattern at the depth of the Bragg peak is shown in fig. 5.9.

An array of clearly separated spots emitting PL in the NIR is visible. The gradient of fluence and hence defect density along the rows is also readily apparent. After demonstrating 3D writing of V_{Si} ensemble spots, the structure of the actual irradiation sites is examined. The bright spots in the scan, like the one on the right, show a normal distribution with high PL emission, hinting at a high number of V_{Si} at these sites. The partic-

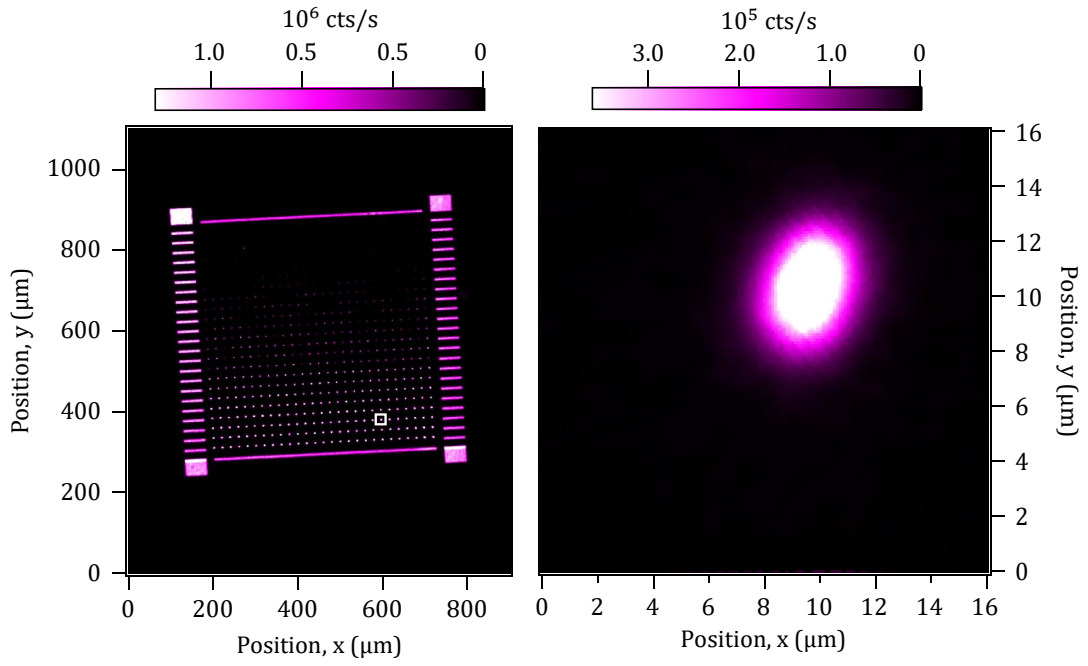

Figure 5.9.: PL xy-scan of the pattern written in sample P5. **left:** xy-scan of the complete pattern. The gradient in fluence of the irradiation sites is readily apparent. **right:** close up xy-scan of one of the stronger irradiated spots.

ular one shown in 5.9 was written with a fluence of $\approx 5 \times 10^{11}\,\mathrm{cm}^{-2}$, which corresponds to ≈ 5000 protons per site. Consequently, the sites irradiated with lower fluences were scanned to find spots with single V_{Si}.

5.2.2. Single silicon vacancies

Close up xy-scans of high fluence spots, as presented in fig. 5.9, suggest that the number of created defects in these spots is too high to observe single defects. To detect single V_{Si} defects, a number of irradiation sites with lower fluences was scanned. Fig. 5.10 shows xy-scans of this type.

As expected, the maximum PL drops with the number of protons per site. For 1000 protons, the maximum of the scan is at 12000 cts/s, for 200 protons, it is at 2000 cts/s. In contrast to the spot shown in fig. 5.9, the spots irradiated with a low fluence show a structure: Additional small, darker spots are present in the vicinity of the actual irradiation site. The maxima at the center of the sites consist of a conglomerate of these small spots. In order to explore the nature of these small spots, photon correlation was measured on a site with even lower fluence. The chosen spot was in the vicinity of an irradiation site, irradiated with 100 protons. The spot, as well as the time-correlated photon detection are presented in fig. 5.11.

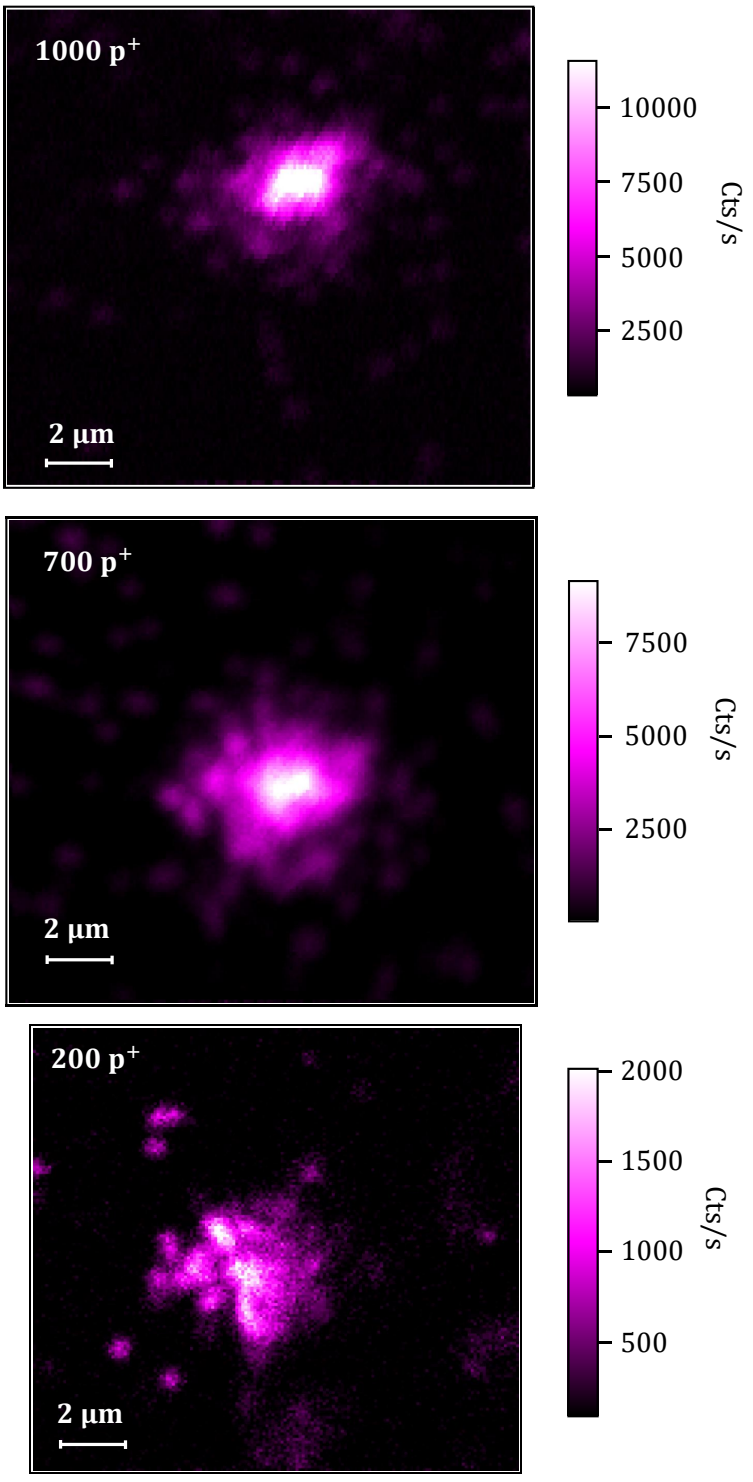

Figure 5.10.: High resolution xy-scans of irradiation sites irradiated with low fluences. In all cases, the maximum is at the center of the site. However, they consist of smaller, darker spots, which are additionally scattered around the center. These are single V_{Si} defects, as will become evident in the following.

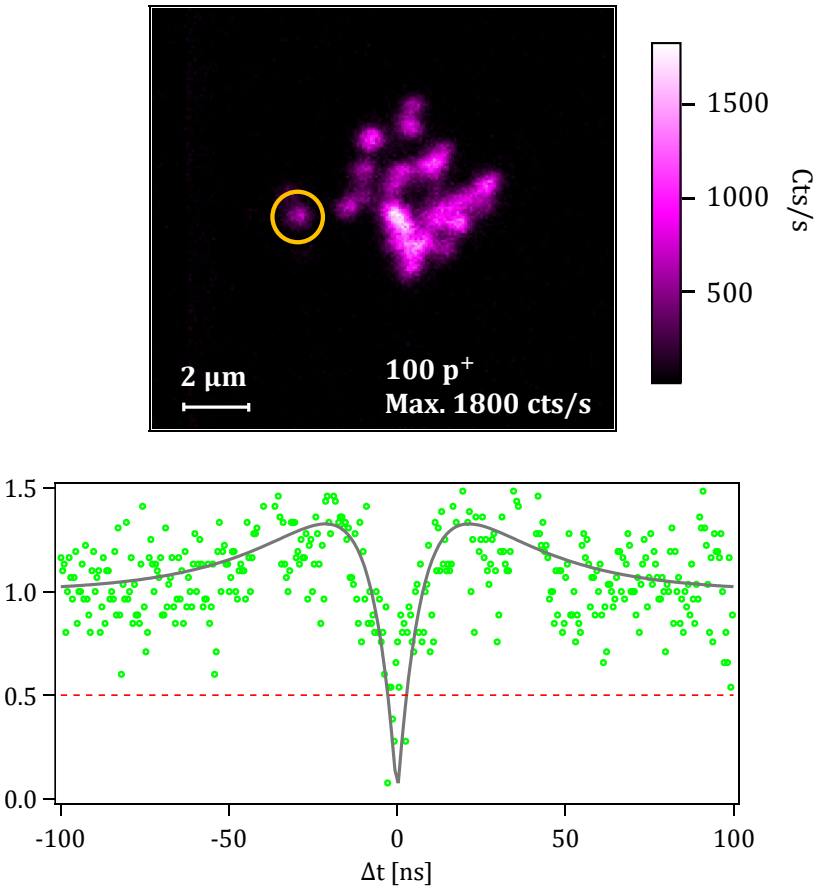

Figure 5.11.: Conglomerate of single V_{Si} defects. **top:** PL xy-scan of an irradiation site irradiated with ≈ 100 protons. The small, individual spots are single V_{Si} defects. **bottom:** Photon correlation measurement of the orange circled center, with $g^{(2)}$ function fit (solid line).

It is no surprise that the maximum count rate is lower than the ones in fig. 5.10. Interestingly, the emitters are only concentrated in the center, unlike in the case of the irradiation sites with higher fluences, where single dots are scattered around the actual sites. This phenomenon was observed in several scans of irradiation sites with low fluences. It is assumed that this is a statistical effect. The more protons enter the crystal, the higher is the probability for a proton to be significantly distracted from the straight path. These protons can then create defects in a lateral distance from the center. This is also supported by the decreasing emitter density as a function of the fluence in the immediate vicinity of the more strongly irradiated spots in fig. 5.10.
The $g^{(2)}$ function was measured on the small PL spot marked with the orange circle in fig. 5.11. The $g^{(2)}$ function clearly indicates anti-bunching with $g^{(2)}(0)$ well below 0.5, identifying the dot as a single photon emitter. Furthermore, the $g^{(2)}$ function shows

bunching. As eludicated in 4.2, this is characteristic for single photon emitters involving a shelving state. With this and the NIR PL spectrum, it is safe to say that the small dots are PB written single V_{Si} defects. This is backed up in the following by a cwODMR spectrum recorded on a PB written PL spot in 6.4, which shows the characteristic fingerprint of the V_{Si} defect.
In order to investigate the z-profile of the irradiation sites, a confocal PL xyz-scan was conducted on several irradiation sites. The xy confocal scans of one of these xyz-scans are exemplary presented in fig. 5.12. Taking into account the z-resolution of the setup, they give proof that most of the single V_{Si} defects are localized within a few μm at the depth of the Bragg peak.

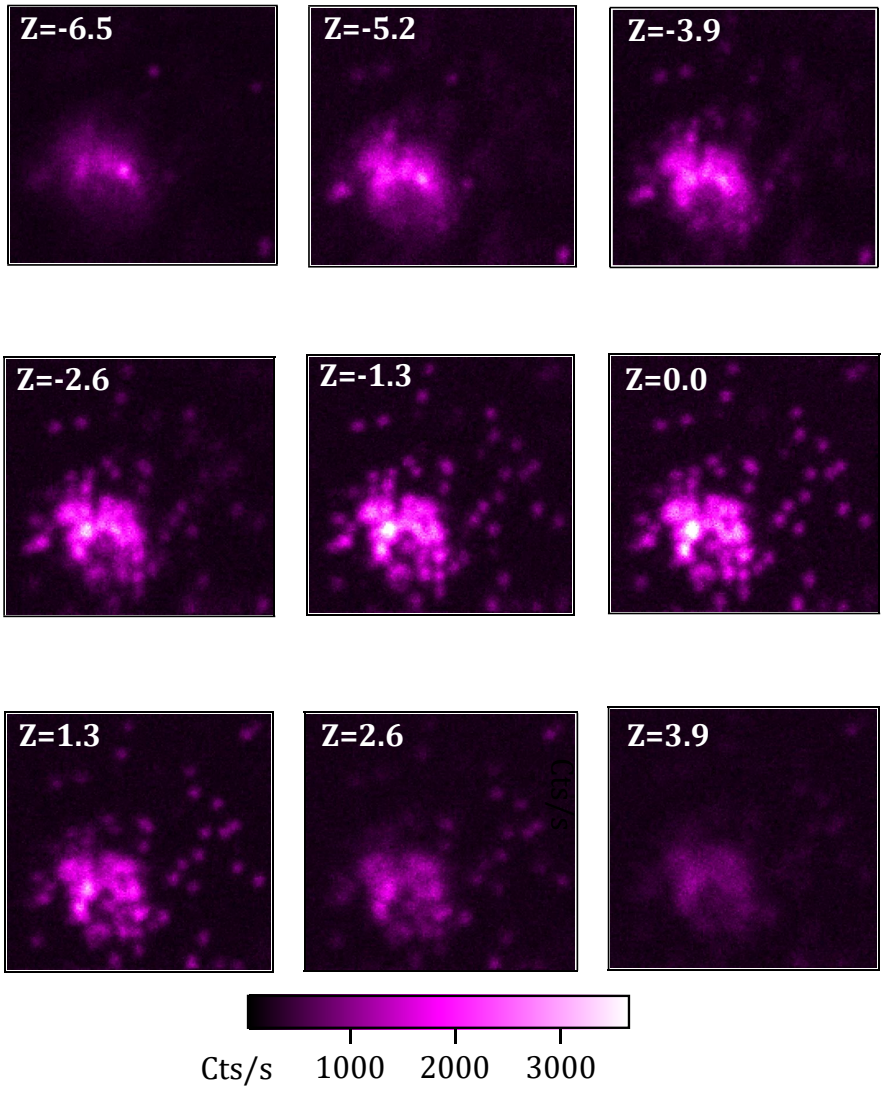

Figure 5.12.: PL xy-scans of an xyz-scan of a PB written spot of V_{Si}. The depth Z is in μm. Almost all V_{Si} are located at one depth, the depth of the Bragg peak.

The numbers are multiples of 1.3 μm because the motor steps of 0.5 μm were corrected by the refraction index. The highest V_{Si} density occurs around the depth of the Bragg peak at $z = 0$. Below the Bragg peak, at positive z, a drastic drop in PL can be observed. Above the Bragg peak, closer to the sample surface, some V_{Si} defects were created. This is in accordance with the results of the SRIM simulation.
In a systematic analysis of the irradiation sites of the pattern, a creation yield of 0.1 V_{Si}/H^+ was determined (for further information see SI of [80]). In theory, this allows downscaling to nearly deterministic production of single defects. Combined with the irradiation of low energy protons this enables engineering of isolated defects on the nanoscale. The use of a pierced atomic force microscope tip can push the lateral control even further, providing a lateral resolution down to 10 nm, similar to that demonstrated for nitrogen implantation into diamond [95]. PB writing of V_{Si} in SiC hence paves the way for a targeted positioning of single defect spins in SiC with nanometer precision in three dimensions without the need of pre- or post-sample-treatment.

6. Influence of irradiation on the silicon vacancy coherence properties

A decisive characteristic of material platforms suitable for quantum applications is their coherence. For example, quantum information processing heavily relies on qubits coherently controllable for a sufficiently long time. Further the sensitivity of quantum sensors is limited by the linewidth of the ODMR resonance peaks [96] and therefore ultimately by the spin coherence of the system [28]. Hence, the usability of the V_{Si} defects in room-temperature SiC-based quantum sensing devices rises and falls with their spin coherence [97].
With that being said, different applications lead to different demands. As discussed in the last chapter, a high density of V_{Si} defects resulting in a higher signal-to-noise ratio is desirable for sensing applications. Similar applies to the use of V_{Si} defects in SiC as gain material for a MASER. In certain cases, targeted creation of V_{Si} defects is required. For each type of application there is therefore a trade-off between the optical properties the V_{Si} defects or a device needs to possess on the one hand and their coherence properties on the other hand. In order to decide how to create the V_{Si} with these desired properties, it is indispensable to have a guideline of how their coherence is affected by their creation method, commonly particle irradiation.
Hence, in this chapter the coherence properties of V_{Si} defects created by electron, neutron or proton irradiation with regards to the emitter density are explored. By using the pulsed optically detected magnetic resonance (pODMR) technique, the spin-lattice relaxation time (T_1) and spin coherence time (T_2) of V_{Si} defects created by neutron, electron or proton irradiation in a broad range of fluences from dense ensemble down to isolated defects are investigated. In 6.1 the pulses used in the pulse sequences for measuring T_1 and T_2 are calibrated. The frequency of the pulses is calibrated by cwODMR and the length by measuring Rabi oscillations with pODMR. Subsequently, T_1 and T_2 are measured as a function of the emitter density via pODMR in 6.2 and 6.3, respectively. The spin coherence of a small ensemble created by proton beam irradiation is

presented in 6.4. This chapter gives a broad overview over the effects of irradiation and the interplay of the emitter density on the spin coherence of V_{Si} defects with the result of a universal formula for the T_2 time for all investigated irradiation particles. The results were published in [90].

6.1. RF pulse calibration

In order to measure the T_1 and T_2 time with pODMR, certain pulse sequences well known from NMR and consisting of RF and laser pulses were applied to the V_{Si} defects. The frequency of the RF waves equals a resonance between the spin sublevels of the ground state and their lengths were calibrated very carefully in order to get the desired spin manipulation and extract T_1 and T_2. The frequency f_R was determined by means of cwODMR for the V_{Si} in each sample. The crucial lengths of a $\pi/2$, π and $3\pi/2$ pulse were calibrated on the basis of Rabi oscillations.

6.1.1. Pulse frequency calibration via cwODMR

The relaxation times T_1 and T_2 were determined by means of pODMR. In the experiments presented in this work, a laser pulse was used to initialize the V_{Si} defects, RF pulses to manipulate them and again a laser pulse to read out the spin polarization via PL (see 4.5). The laser wavelength of 787.5 nm is chosen close to the center of the absorption band of the V_{Si} defects. It is necessary to apply the RF pulses with a frequency f_R according to one of the resonance transitions between the spin sublevels of $|GS\rangle$ of the V_{Si} defects. Only in that case the chosen transition can be RF driven and the spin polarization manipulated.
In zero magnetic field $B_0 = 0$ mT the RF pulses are in resonance if f_R corresponds to the ZFS. In the pODMR experiments presented in this work, a moderate magnetic field of $B_0 \approx 15$ mT along the c- axis of the SiC crystal was applied in order to suppress interactions with the surrounding spin bath of nuclei. A discussion regarding this topic follows in 6.3. In a magnetic field, the spin sublevels split due to Zeeman interaction according to 2.2.6, resulting in two resonances ν_1 and ν_2, which are eligible for the RF pulses in pODMR. The frequency f_ν of a resonant transition can be calculated as [8]:

$$f_{\nu_1} = \left| \frac{ZFS - g_e \mu_B B_0}{h} \right|$$
$$f_{\nu_2} = \left| \frac{ZFS + g_e \mu_B B_0}{h} \right| \tag{6.1}$$

However, B_0 might marginally change during a switch of samples due to a slightly different positioning. Since slight changes in the external magnetic field B_0 lead to a change of the frequencies of the resonances, the RF pulse frequencies were recalibrated prior to each T_1 or T_2 protocol. The frequencies of the resonance transitions were derived from cwODMR spectra. The deviation of B_0 for all measurements was determined as $B_0 = 15 \pm 0.4\,\mathrm{mT}$.

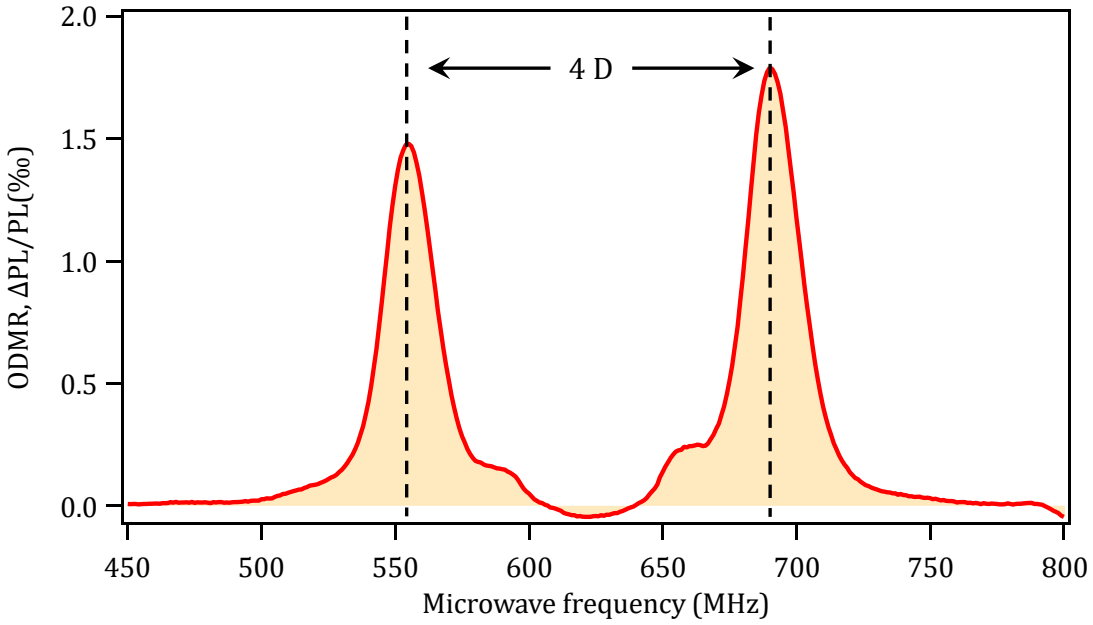

Figure 6.1.: Room temperature cwODMR spectrum of V_{Si} in an external magnetic field of $B_0 = 15\,\mathrm{mT}$. The peaks correspond to the resonant transitions ν_1 and ν_2. The distance between the peaks in a magnetic field equals double the ZFS.

Fig. 6.1 shows an ODMR spectrum measured on neutron irradiated SiC in such an external magnetic field of $B_0 = 15\,\mathrm{mT}$. The two resonance peaks at 550 MHz and 690 MHz show a gap of $\Delta_f = 4D \approx 140\,\mathrm{MHz}$ between them, equaling the double energy of the ZFS.

In addition to the calibration of f_R, the position of the resonance peaks in the spectra serve another function. As described in 2.2.4, the ZFS can be seen as fingerprint of the V_{Si} defect type. Thus, the spectra are clear evidence that the crystals contain V_{Si} defects created by irradiation.

Having calibrated the RF frequency f_R for the pulses in the pulse sequences applied to obtain T_1 and T_2, the pulse lengths were derived from the measurement of Rabi oscillations. This is explained in the next two subsections.

6.1.2. Rabi oscillations

In order to measure the relaxation times of any spin system some prior knowledge of the system is necessary. For the measurements in this work this means, that the lengths of a $\pi/2$-, π- and $3\pi/2$-RF pulse are needed for the pulse sequences for measuring T_1 and T_2. The lengths of these pulses can be derived from RF driven Rabi oscillations between the spin sublevels of the V_{Si} defects. As already mentioned, pulse sequences well known from the field of NMR were adapted and carried out via pODMR. In that way it is possible to coherently control and read out the spin state of V_{Si} defects.
For measuring Rabi oscillations, the pulse sequence shown in the upper part of fig. 6.2 was applied. The evolution of the spin polarization over time with constantly applied resonant RF waves is presented in the middle and lower part.

In the applied external magnetic field of $B_0 = 15$ mT, $|\pm 1/2\rangle$ and $|\pm 3/2\rangle$ are energetically split due to Zeeman interaction. All pODMR measurements shown in this chapter were conducted either on the ν_1 or ν_2 transition. In the following, the Rabi oscillations on the ν_2 transition between the $|+1/2\rangle$ and $|+3/2\rangle$ spin sublevels are considered.
The first laser pulse initializes the V_{Si} defects into the $|+1/2\rangle$ sublevel. Hereafter, the population of the $|+1/2\rangle$ sublevel is higher than the one of the $|3/2\rangle$ sublevel. The population difference can be estimated to be below 1% at room temperature [55] from EPR experiments. Only this population difference contributes to the signal.
Position I schematically shows the situation immediately after a laser pulse is switched off. If a resonant RF pulse is applied, the RF waves induce transitions from $|+1/2\rangle$ to $|+3/2\rangle$ and from $|+3/2\rangle$ to $|+1/2\rangle$. Since the population of $|+1/2\rangle$ is higher at position I, statistically more transitions from $|+1/2\rangle$ to $|+3/2\rangle$ are induced until the populations are equal (position II). However, the polarization flips into the $|+3/2\rangle$ sublevel due to a kind of overshoot (Position III) [98]. With RF waves still applied, a spin polarization flip back from $|+3/2\rangle$ to $|+1/2\rangle$ is induced (position IV). In this manner, the spin ensemble polarization is flipped between $|+1/2\rangle$ and $|+3/2\rangle$ as long as the RF waves are applied. This phenomenon is referred to as Rabi oscillations.
The final spin polarization after an RF pulse depends on the pulse length τ, which is consequently the variable in this kind of experiment. A complete pulse sequence consists of many of the segments shown in the top part of fig. 6.2, with the pulse length τ being iteratively increased. The spin state after an RF pulse was read out subsequently via the spin state dependent PL of the V_{Si} defects during the first μs of the next laser pulse. The ODMR contrast $\Delta PL/PL$ is calculated after each RF pulse with iteratively increasing RF pulse lengths τ. The ODMR contrast directly corresponds to the spin state and consequently shows the Rabi oscillations when plotted as a function of τ. A plot of

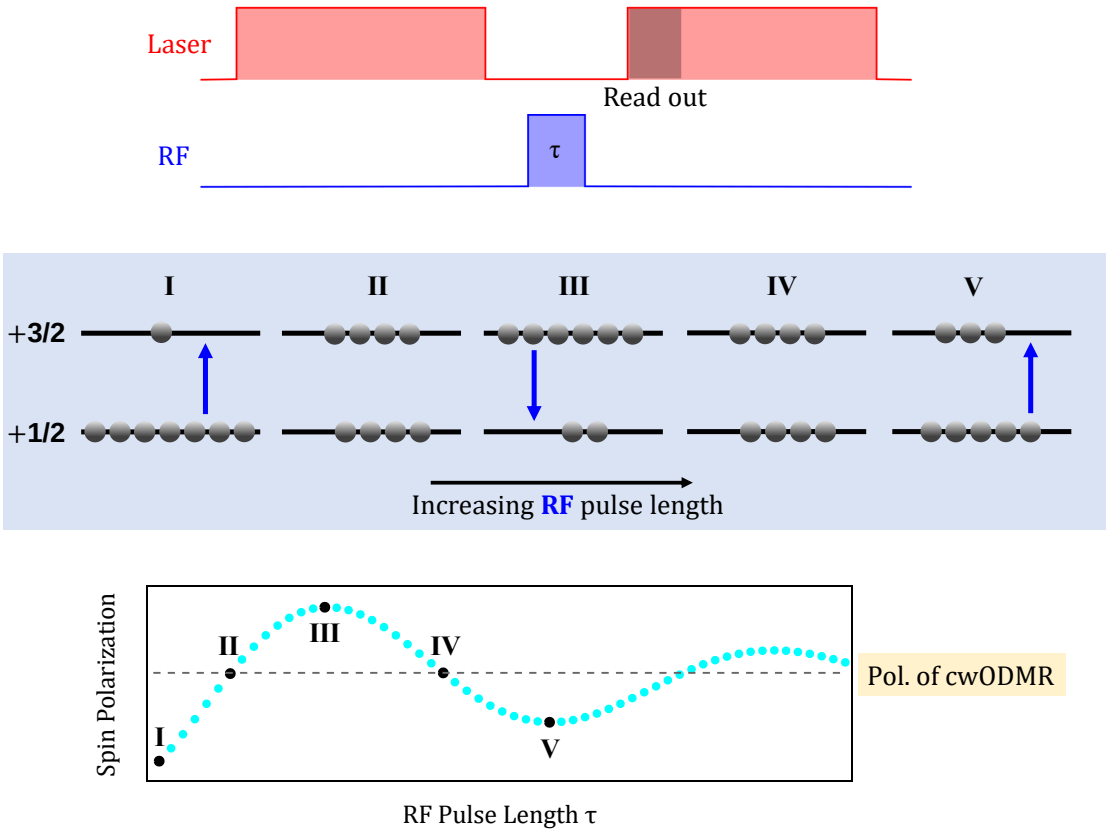

Figure 6.2.: Principle of Rabi oscillations of a V_{Si} ensemble **top:** Single segment of the pulse sequence to measure Rabi oscillations with pODMR. The first laser pulse initializes the spin ensemble. Spin manipulation is carried out by an RF pulse, while the pulse length is iteratively increased at every second segment (One reference signal; see 4.5). **middle:** Schematic representation of the spin polarization due to the RF induced resonant transitions as a function of the pulse length. The gray circles located at a spin sublevel represent one V_{Si} defect in that particular sublevel. Position I represents the polarization of an optically pumped spin ensemble immediately after the laser is switched off. **bottom:** Resulting Rabi oscillations of the spin polarization. The oscillations can be measured by means of pODMR. Each data point corresponds to the ODMR contrast measured after one destinct pulse length τ.

this kind, measured on a V_{Si} ensemble created by neutron irradiation, is presented in fig. 6.3.

Additionally to the oscillation, the polarization exponentially decays due to spin-spin decoherence [98]. The spin polarization ultimately saturates at an equal population of $|+1/2\rangle$ and $|+3/2\rangle$, which is none other than the spin polarization achieved with cwODMR.

The oscillations can be fitted to:

$$S(\tau) = -\frac{\Delta PL}{2PL} e^{-\tau/T_R} cos(\Omega_R \tau) + C. \tag{6.2}$$

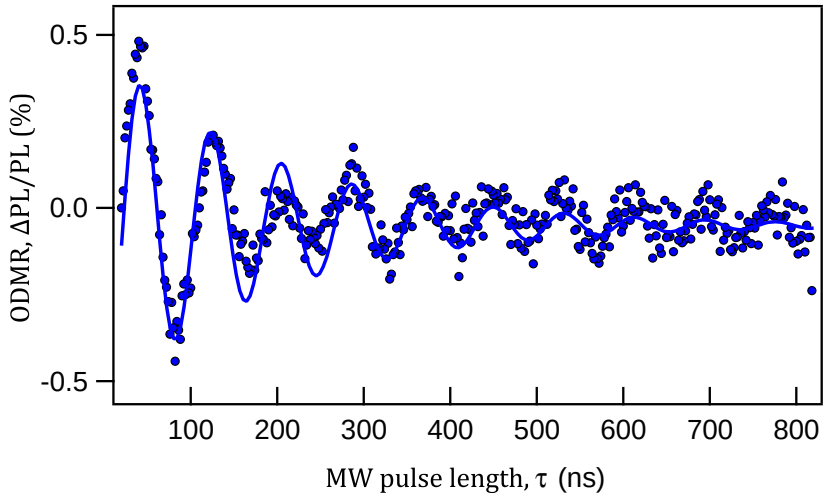

Figure 6.3.: RF driven Rabi oscillations of the V_{Si} ensemble in a sample from S1, irradiated with a neutron fluence of $\Phi_n = 4.2 \times 10^{15}\,\mathrm{cm}^{-2}$ and corresponding $N_V = 1.6 \times 10^{15}\,\mathrm{cm}^{-3}$ and measured with pODMR. The spin polarization levels off at the cwODMR contrast for long RF pulses.

Here, T_R is the decay time of the Rabi oscillations, Ω_R is the angular Rabi frequency and C is a constant.

The spin manipulation processes in the protocols used to measure T_1 and T_2 in this thesis are more complex than the one for Rabi oscillations. Therefore, it is favorable to view the spin polarization with the help of a more abstract model. Every quantum mechanical two-level system can be described by using a Bloch Sphere. Hence, Bloch Spheres have proven themselves practical and are commonly used for illustrating and understanding the processes in NMR experiments, as well as in pODMR [99]. The Bloch Sphere model is also accurate for an ensemble of V_{Si} defects. The poles of the sphere represent the eigenstates of a system, in case of ν_2 this is $|+1/2\rangle$ and $|+3/2\rangle$. The polarization of the system is described by a vector, originating at the center of the sphere. Its z-component represents the population ratio between $|+1/2\rangle$ and $|+3/2\rangle$. Fig. 6.4 shows the effect of the pulse sequence applied to measure Rabi oscillations on the spin polarization of a V_{Si} defect spin ensemble with the RF waves in resonance to ν_2. The corresponding polarization is represented by the brown arrow. If the arrow points up, the spins are polarized in the $|+1/2\rangle$ sublevel, if it points down, in $|+3/2\rangle$. Other directions symbolize the V_{Si} ensemble in a superpostition of $|+1/2\rangle$ and $|+3/2\rangle$.

After laser excitation, the spins of the V_{Si} ensemble are optically pumped and the polarization points up. Subsequently, the first RF pulse rotates the spin away from the z-axis by a certain angle, depending on τ. The second laser pulse again initializes the spin system (arrow up) and the second RF pulse induces a reference rotation of the polarization.

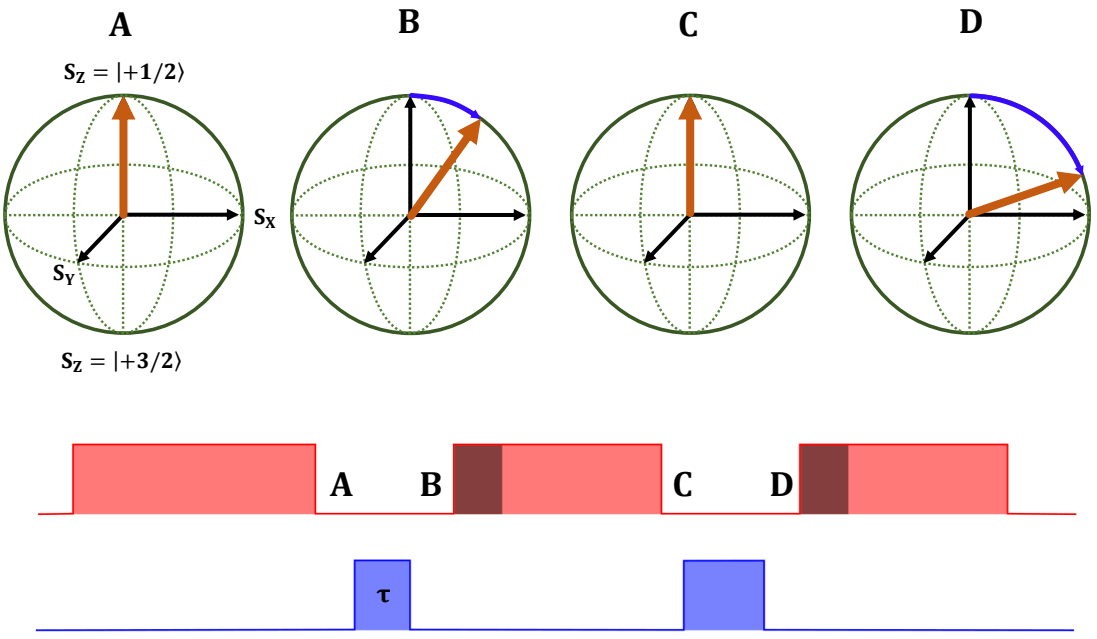

Figure 6.4.: Spin polarization of a V_{Si} ensemble, resonantly driven with RF waves. The Bloch spheres A – D represent the spin polarization at different stages of the pulse sequence used to measure Rabi oscillations. The polarization (brown arrow) is rotated by the resonant RF waves and reinitialized into $S_z = |+1/2\rangle$ by the laser pulses.

This very vivid picture of the spin polarization in the Bloch sphere is used in the following to explain the calibration of $\pi/2$-, π- and $3\pi/2$-RF pulses.

6.1.3. Calibration of the pulse lengths

The $\pi/2$, π and $3\pi/2$ RF pulses are named after the rotation angle they inflict on the polarization. It is remarkable that the spin polarization in fig. 6.4 oscillates around zero and also tends towards zero for long pulses. Looking again at the pulse sequence for Rabi measurements and the corresponding spin rotation in the Bloch sphere, it becomes evident, that this is not a matter of course, but a special case. Since the read-out of the spin polarization with a laser pulse is represented by a projection of the polarization onto the S_Z axis, an oscillation around zero can only occur if the reference pulse rotates the spins exactly into the $S_x - S_y$ plane. As mentioned, a pulse of this length is called $\pi/2$-pulse, since it rotates the spin around the angle $\pi/2$, as depicted in fig. 6.5. In analogy with that, the π-pulse flips the spin polarization around π and the $3\pi/2$ pulse around $3\pi/2$.

Thus, to determine the length of a $\pi/2$- pulse, several Rabi measurements were conducted before each T_1 and T_2 measurement and the reference pulse was calibrated so that the oscillation tends towards zero. In this case, the reference pulse creates the

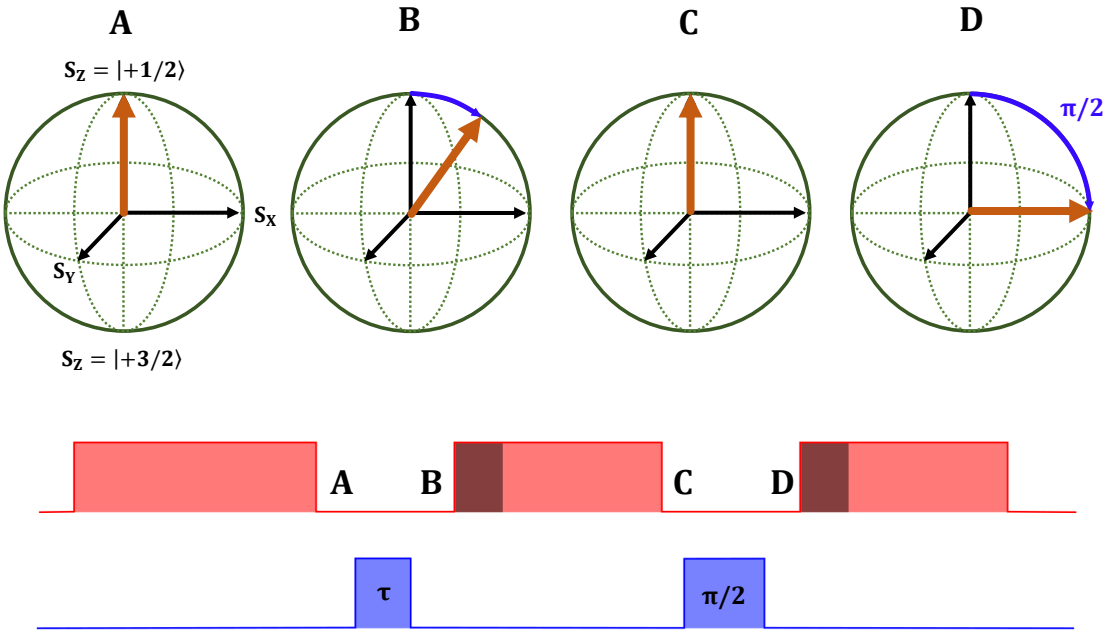

Figure 6.5.: Spin polarization induced by the Rabi pulse sequence with a $\pi/2$-pulse as reference pulse. If the reference pulse is calibrated to a $\pi/2$-pulse, the spin polarization in the resulting plot of the form as presented in fig. 6.3 oscillates around zero.

same spin polarization as cwODMR and has the length of a $\pi/2$ pulse. The π- and $3\pi/2$-pulse were derived from the first maximum and the second inflection point in fig. 6.3. The $\pi/2$-pulse can - in principle - also be derived from the first inflection point in this graph. However, the length of the $\pi/2$-pulse is crucial and the aforementioned method more accurate.

The pulse lengths are highly dependent on various measurement parameters, above all the B_1 field of the RF waves. The Rabi frequency Ω_R is proportional to B_1 and hence depending on the RF power P_{RF}:

$$\Omega_R \propto B_1 \propto \sqrt{P_{\mathrm{RF}}} \tag{6.3}$$

The RF emission characteristic of the strip line can be inhomogeneous, leading to a different RF power and therefore B_1 at different illumination spots. Hence, the pulses were calibrated before each measurement of T_1 or T_2.

To avoid any relaxation mechanisms during the pulses, it is preferable to select short pulses. Therefore, according to eq. 6.3, the RF power was chosen as high as possible. The maximum output power of the RF amplifier used is 44 dBm. As a precautionary measure to protect the microwave components, such as the stripline and the terminating resistor, a lower power was applied. At ≈ 5 W output power, the achieved spin polarization amplitude was high enough to conduct measurements in acceptable time

scales, but low enough to not cause damage to the RF components or the stripline. The pulse lengths were in the order of 100 ns.
With the RF pulse lengths and frequency calibrated, the preperations for the pulse sequences to extract T_1 and T_2 were made.

6.2. Spin lattice relaxation time T_1

The ability to coherently control a spin system, e.g. by means of Rabi oscillations, is not the only attribute that is required for applications such as quantum sensing, quantum computing or quantum information processing. It is also necessary that the interactions with the environment are weak, as this leads to a long lifetime of the spin states in which the spin system can be controlled and ultimately worked with. The lifetime of spin systems, like the V_{Si} defect, is well described by the relaxation times T_1 and T_2.
The relaxation process related to the T_1 time is called spin-lattice relaxation. In case of a V_{Si} defect ensemble pumped into the $|\pm 1/2\rangle$ state, intrinsic, irreversible processes like interactions with lattice phonons cause spin lattice relaxation back to thermal equilibrium. The time constant T_1 describes the time until the spin polarization has reached $1/e$ of the initial polarization. Since the spin polarization is completely erased by spin lattice relaxation, it imposes the absolute limit of coherent control.
In the Bloch sphere, the T_1 time describes the decay of the projection of the polarization onto the S_Z axis. Hence, it is also called longitudinal relaxation time. Fig. 6.6 shows the spin lattice decay of the spin polarization after optical pumping into the $|+1/2\rangle$ state for different delay times τ.

Immediately after optical pumping, the polarization is in the $|+1/2\rangle$ state. With time elapsing, the polarization decays, illustrated by a reduction of the S_Z component of the polarization (cyan arrow). For measuring the T_1 time, the pulse sequence shown in Fig. 6.7 was applied to the V_{Si} defects.

In analogy to the measurement of the Rabi oscillations, one laser pulse polarizes the V_{Si} defect ensemble and is also used to read out the final polarization. In the T_1 sequence, the spin system decays freely during a delay time τ inbetween two laser pulses. This delay time is iteratively increased and the remaining polarization for each destinct value of τ is read out via PL. To obtain a reference signal for ΔPL/PL, the polarization was allowed to evolve freely twice for each τ. After the first of these two delay times, it was flipped by a π pulse right before read-out. This not only creates a reference signal, but also maximizes the amplitude of the measured spin polarization difference for a better signal-to-noise ratio.

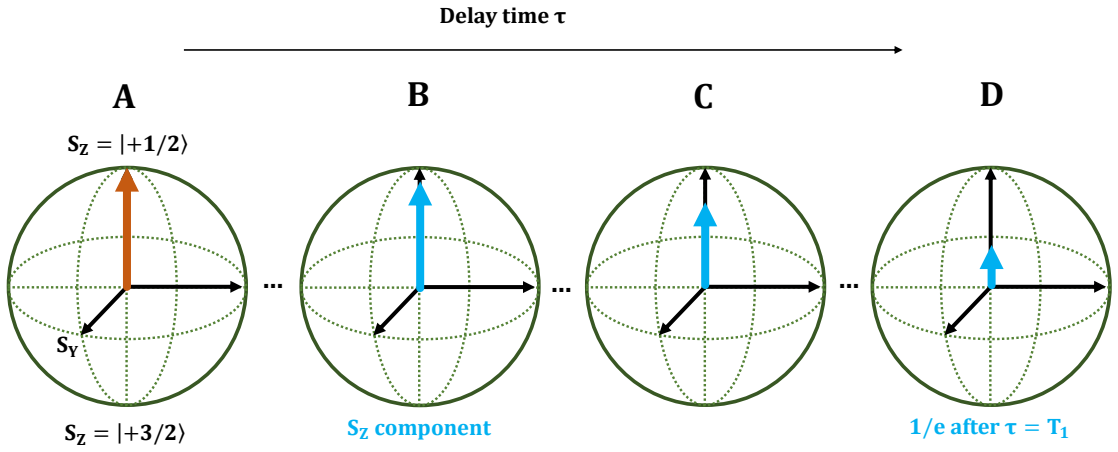

Figure 6.6.: Decay of the V_{Si} spin polarization after optical pumping, represented by the cyan arrows. At position **A**, the polarization (brown arrow) is maximal. The time constant, after which the polarization decayed to $1/e$ of the initial polarization, as shown in **D**, is called T_1.

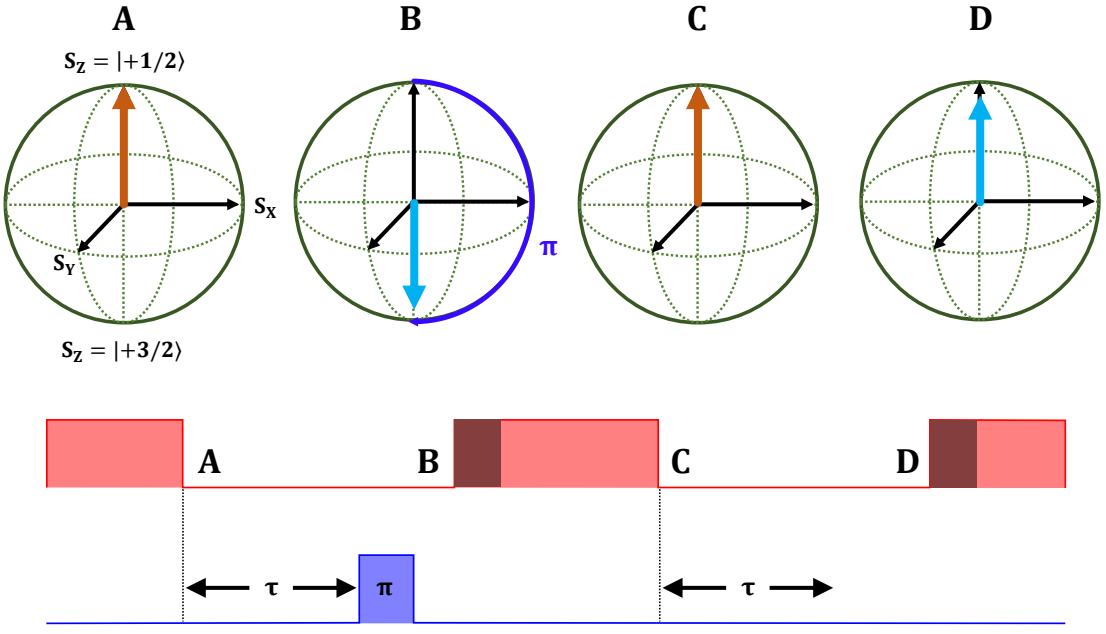

Figure 6.7.: Pulse sequence and corresponding spin polarization during the measurement of the T_1 time as conducted in this work. The polarizations at A – D correspond to the stages marked in the pulse sequence. At **A** and **C**, the system is initialized by the laser pulse. **B** and **D** show the polarization right before read-out.

The result of such a measurement on a neutron irradiated ($N_V = 5.8 \cdot 10^{15}\,\mathrm{cm}^{-3}$) sample from sample set S2 is displayed in fig. 6.8. The exponential decay is fitted in the form [26]:

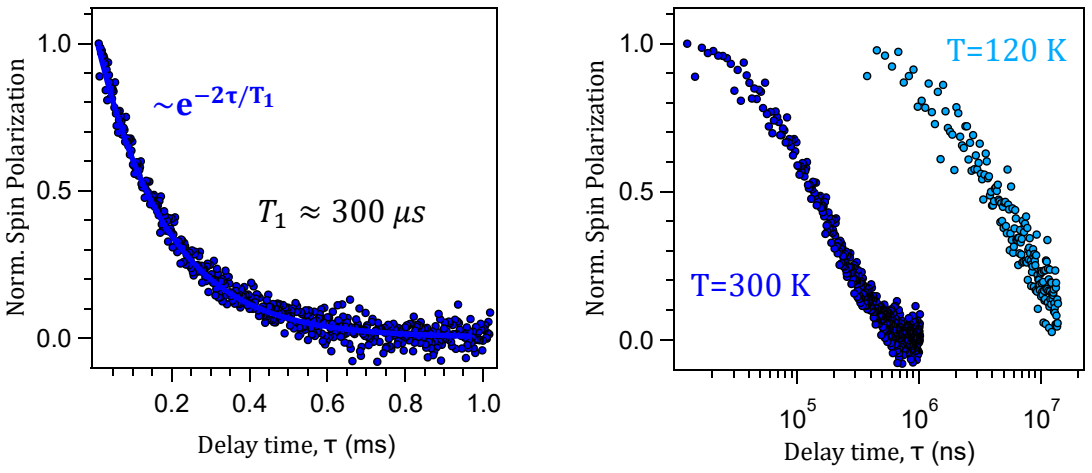

Figure 6.8.: Spin polarization as a function of the delay time τ at RT and cryogenic temperature. **left:** Decay of the spin polarization fitted with an exponential fit to extract $T_1 \approx 300\,\mu$s. **right:** Prolongation of T_1 at low temperature due to a reduction of phonon density.

$$\mathscr{P}_Z(\tau) = \mathscr{P}_{Z,0} exp\left(\frac{2\tau}{T_1}\right) \tag{6.4}$$

From a fit of this kind, T_1 can be extracted. In comparison the T_1 time at $T = 120\,$K is enormously prolonged. The dependency of the temperature T on T_1 has been exstensively studied by our group [22], which lead to the establishment of a power law function

$$\frac{1}{T_1(T)} = A_0 + A_1 T + A_5 T^5 + \frac{R}{e^{\Delta/k_B T} - 1} \tag{6.5}$$

to describe the involved processes: It takes into account two phonon-Raman scattering ($A_5 T^5$), an eventual Orbach-like process via a vibrational state ($1/e^{\Delta/k_B T} - 1$) and single phonon Raman scattering ($A_1 T$). Each of these processes is dominant in different temperature regimes. The limit of T_1 is defined by the temperature independent cross relaxation with intrinsic defects (A_0). It is only significant for low phonon densities at cryogenic temperatures and, naturally, in samples with high defect densities.
In the following, the effect of the irradiation method and fluence on T_1 is considered. Fig. 6.9 shows the T_1 times of V_{Si} defects in samples irradiated with various fluences of neutrons (S1) or electrons (S2) and a neutron irradiated sample before and after annealing. The achieved emitter densities N_V determined via PL are in the range of $3.9\cdot10^{14} - 9.04\cdot10^{15}\,cm^{-3}$ in the electron irradiated samples and $2\cdot10^{15} - 1.28\cdot10^{16}\,cm^{-3}$ in the neutron irradiated samples.

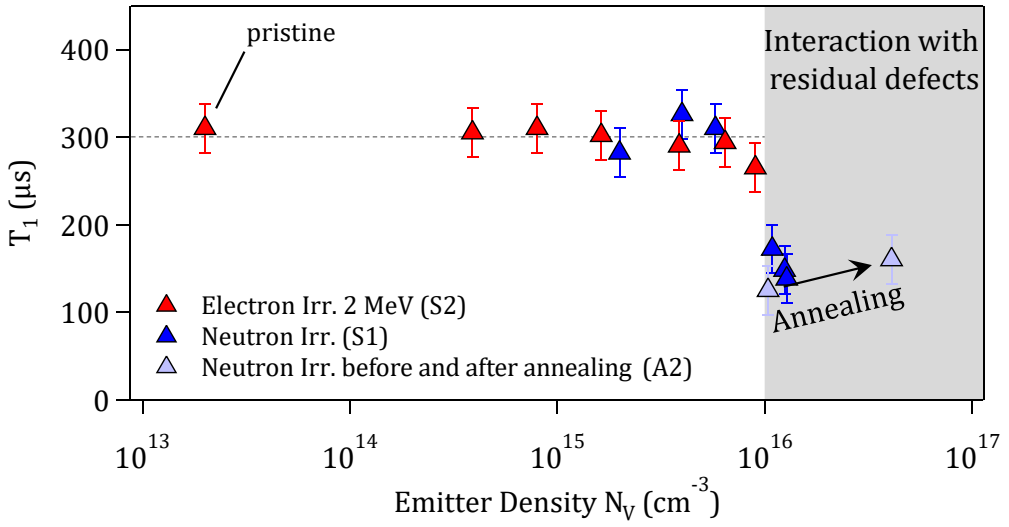

Figure 6.9.: T_1 of V_{Si} ensembles created with neutrons or electrons in the sample sets S1 and S2 and in sample A2 as a function of the emitter density. It is constant up to a defect density at which the cross relaxation between spin defects becomes significant. Additionally, T_1 of a strongly neutron irradiated ($\Phi_n = 1 \times 10^{18}\,\mathrm{cm}^{-2}$ and $N_V = 1 \times 10^{16}\,\mathrm{cm}^{-3}$) sample before and after sample annealing is presented. This is discussed in detail in 7.3.

The values of T_1 in both electron and neutron irradiated samples are distributed around $T_1 \approx 300\,\mu$s, which corresponds well with previously measured T_1 times in V_{Si} ensembles [22]. T_1 turns out to be quite robust against N_V. This can be expected, since the processes mainly contributing to the spin lattice relaxation at RT are phonon assisted and hence not depending on N_V [22]. The only mechanism involving defect-defect interaction is the cross relaxation described by A_0.

The effect of cross relaxation is observable in neutron irradiated samples with high N_V, where a drop of T_1 occurs for $N_V > 10^{16}\,\mathrm{cm}^{-3}$. At these high emitter densities, the interaction with other defect spins becomes a relevant process for spin relaxation. This leads to the observed decrease of T_1. By sample annealing it was possible to increase, but not completely recover T_1 of V_{Si} defects in a heavily neutron irradiated sample with a fluence of $\Phi_n = 1 \times 10^{18}\,\mathrm{cm}^{-2}$ and corresponding $N_V = 1 \times 10^{16}\,\mathrm{cm}^{-3}$. This is discussed in detail in 7.3.

In the electron irradiated samples, the T_1 time of the sample with the highest emitter density also shows first signs of a decline. The T_1 time of V_{Si} defects in electron irradiated samples with higher emitter density is expected to be shortened as well.

The results obtained with two systematically irradiated sample sets, S1 and S2, provide good insight into the effect of the irradiation fluence and corresponding emitter density on the T_1 time . To get an even broader overview, the T_1 time of a proton irradiated

sample (P5), two neutron irradiated samples (N1 and N2) of a different wafer and electron irradiated samples (E1 and E2) with varying energies were measured. They are plotted together with the data points of S1 and S2 from fig. 6.9 in fig. 6.10.
All of these samples show the same $T_1 \approx 300\,\mu s$, which underpins the previously discussed dominant influence of phonon-assisted mechanisms on the spin lattice relaxation and an independence from N_V up to a certain emitter density limit.
Furthermore, the results are compared to $T_1 = 500\,\mu s$ of a single V_{Si} defect reported in a sample with $N_V \approx 10^{11} - 10^{12}\,cm^{-3}$ [26]. Although the T_1 time is slightly higher than the ones obtained in this work, the results are still fairly close and hence can be considered to be in good agreement.

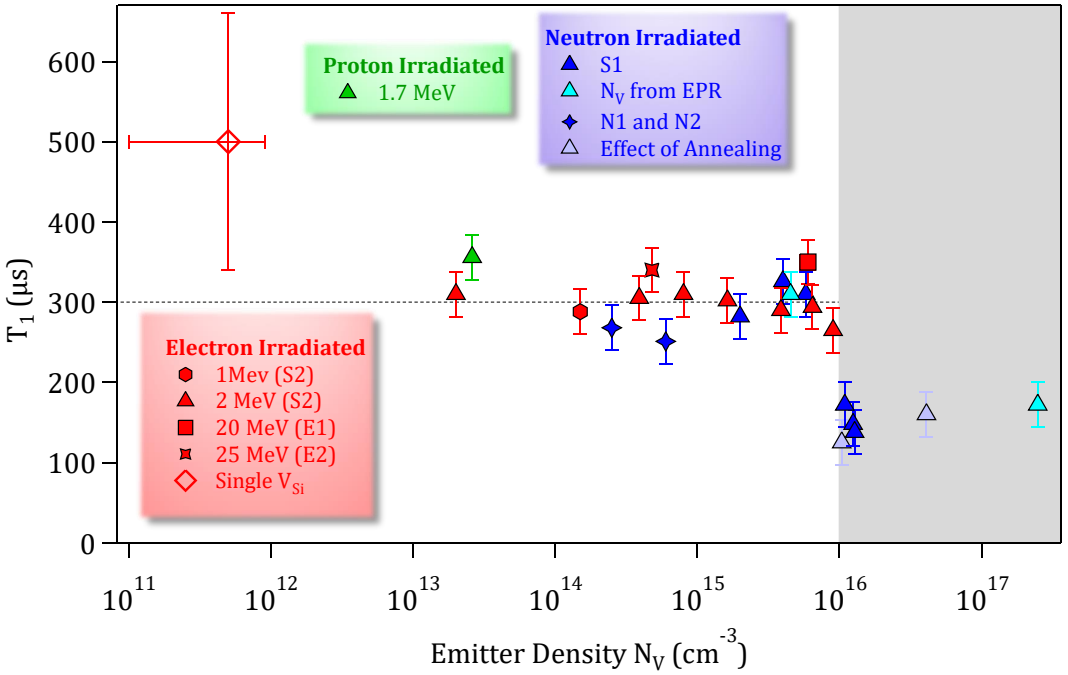

Figure 6.10.: T_1 of V_{Si} defects in various samples irradiated with different particles, fluences and energies. T_1 proves to be robust against all these parameters. Only at high N_V the T_1 time diminishes.

In order to take into account the information obtained in ch. 5.1.2 about the deviations of the emitter density determined from PL measurements and EPR, the T_1 times of the two neutron irradiated samples from ch. 5.1.2 with the corresponding N_V from EPR are additionally included in fig. 6.10. The two data points again confirm that for emitter densities in the lower regime the determination of N_V via PL is a viable method, whereas for high densities it seems to be less precise. It can be further concluded, that the observed drop of T_1 for $N_V > 10^{16}\,cm^{-3}$ is likely to be less steep and to set in at a

higher limit of N_V.
The results obtained in this chapter reveal a constant T_1 time $T_1 \approx 300\,\mu$s of V_{Si} defects in samples with $N_V < 10^{16}\,\mathrm{cm}^{-3}$. At higher N_V, T_1 is shorter, which eventually impedes the performance of the V_{Si} with regards to quantum sensing and other applications. Ultimately it can be concluded, that when aiming for V_{Si} with long spin lifetime, the emitter density should be chosen to be $N_V < 10^{16}\,\mathrm{cm}^{-3}$.

6.3. Spin coherence time T_2

Next, the influence of N_V on the spin coherence time T_2 is examined. The T_2 time is also called transverse relaxation time, because, in contrast to the T_1 time, it describes the decay of the transverse component of the spin polarization in the S_x-S_y-plane of the Bloch sphere. It is in general shorter than T_1 and hence poses the limit of spin manipulation in most material systems. Its dependence on the emitter density N_V is of great interest for all related quantum applications.
To access the T_2 time of the V_{Si} defects in SiC, the spin echo pulse sequence is applied. It is schematically presented in fig. 6.11.

After initialization, a resonant $\pi/2$ pulse is applied, inducing a rotation of the spin polarization into the S_x-S_y-plane. Due to local differences in the immediate vicinity of the defects, the individual spins dephase from each other and the spin polarization decays. A variety of processes can cause dephasing, e.g. a deviating frequency of single spins in the S_x-S_y-plane due to a slight difference in the B_1 field.
After a free evolution time $\tau/2$, during which the spins dephase, a π pulse is applied. The processes that caused dephasing are now rephasing the spins and the spin polarization is restored. The restored spin polarization, called spin echo, has its maximum at $\tau/2$ after the π pulse.
Apart from the reversible processes causing dephasing, however, there are also irreversible processes hindering a complete restoration of the spin polarization in the S_x-S_y-plane. The most important irreversible processes involve interactions with other spin defects, leading to "jumps" of the spins in the S_x-S_y plane. When the spins are flipped by the π pulse, these jumps prevent some spins from rephasing at $\tau/2$ after the π pulse and the amplitude of the spin-echo diminishes. The longer the free evolution time τ is, the more spins are subject to irreversible processes leading to a smaller amplitude of the spin-echo. The time constant, after which the echo is damped to $1/e$ of the initial polarization, is the spin coherence time T_2.
In order to read out the remaining spin polarization of the spin echo via PL it must be projected onto the S_z axis. This was achieved by a $\pi/2$ pulse at the end of each

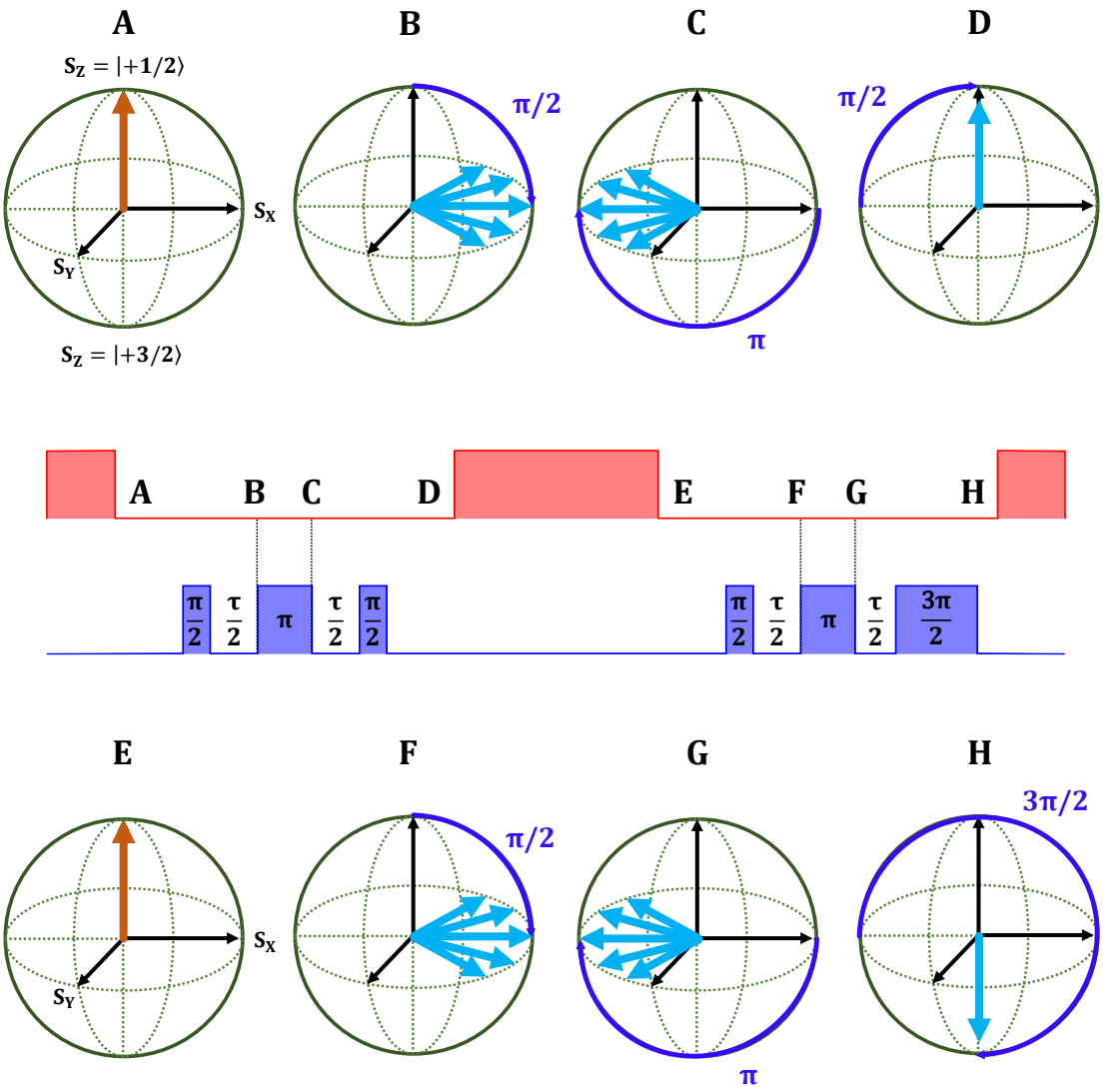

Figure 6.11.: Spin-echo pulse sequence and corresponding spin polarization. The sequence with a free evolution time $\tau/2$ is well known from NMR experiments. A $\pi/2$-pulse transfers the spin polarization into the S_x-S_y-plane, where it dephases with the time constant T_2 due to inhomogeneties in the vicinity of the individual spins. A subsequent π-pulse reverses the dephasing and causes a spin echo. The echo is projected onto the S_z-axis and read out via PL. For reference, a $3\pi/2$-pulse is applied at the end of a second segment for each $\tau/2$.

segment. In order to generate a reference signal, the PL is additionally recorded after a $3/2\pi$ pulse at the end of a second segment for each $\tau/2$. In analogy to the T_1 sequence, $\tau/2$ is iteratively increased and the polarization extracted from the two spin dependent PL values recorded for each $\tau/2$. The result obtained by a measurement of this type is presented in fig. 6.12. The decays were recorded in an external magnetic field $B_0 = 15\,\mathrm{mT}$ to suppress interactions of the spins with the surrounding nuclear spin

bath [100]. The two upper graphs show the spin polarization as a function of τ for the ν_1 (top) and ν_2 (middle) transition. They were measured on an electron irradiated sample from S2, irradiated with a fluence of $\Phi_e = 1 \times 10^{17}\,\mathrm{cm}^{-2}$ with a corresponding emitter density $N_V = 3.9 \times 10^{14}\,\mathrm{cm}^{-3}$. The lower graph shows the same at the ν_2 transition for a neutron irradiated sample of S1, irradiated with a fluence of $\Phi_n = 3.7 \times 10^{17}\,\mathrm{cm}^{-2}$ with corresponding $N_V = 1.3 \times 10^{16}\,\mathrm{cm}^{-3}$.

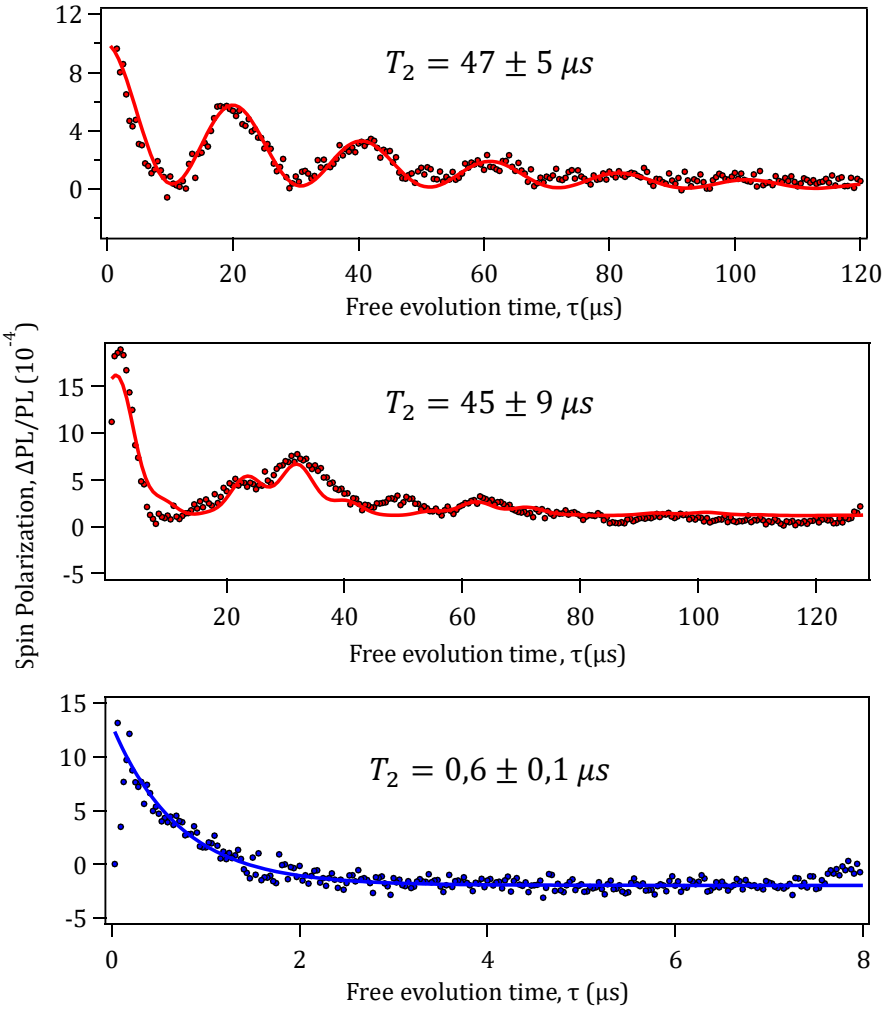

Figure 6.12.: Decay of the spin polarization of a V_{Si} ensemble due to decoherence. **top:** Decay measured on the ν_1 transition in an electron irradiated sample with a fluence of $\Phi_e = 1 \times 10^{17}\,\mathrm{cm}^{-2}$ and corresponding emitter density $N_V = 3.9 \times 10^{14}\,\mathrm{cm}^{-3}$. **middle:** Same as top but measured on the ν_2 transition. **bottom:** Decay measured on the ν_2 transition in a neutron irradiated sample with a fluence of $\Phi_n = 3.7 \times 10^{17}\,\mathrm{cm}^{-2}$ and corresponding $N_V = 1.3 \times 10^{16}\,\mathrm{cm}^{-3}$.

In the case of the electron irradiated sample, the evolution of the spin polarization not only shows an exponential decay, but also a periodic modulation of the signal. This effect is typical for experiments of this kind and is called electron spin echo envelope

modulation (ESEEM) [54] [26] [101]. The collapse and following revival of the spin polarization is caused by interactions of the V_{Si} spins with the spins of naturally abundant ^{29}Si and ^{13}C nuclei in the sample. The Larmor precession of the nuclei in the external magnetic field induces the defect spins to periodically dephase and rephase, resulting in the observed modulation of the spin-echo amplitude. In case of the ν_2 transition, the frequencies of both nuclei can be observed, while in case of the ν_1 transition, only the interactions with the more abundant ^{29}Si show a significant influence on the signal. The solid lines represent fits to

$$\mathscr{P}_Z(\tau) = \mathscr{P}_{Z,0} exp\left(\frac{\tau}{T_2}\right) \prod_{i=a,b} \left(1 - K_i sin^2\left(\pi f_i \tau\right)\right) \tag{6.6}$$

with a constant K_i and the two Larmor frequencies f_a and f_b of the isotopes. In case of ν_1, one frequency ESEEM is fitted with only f_a, in case of ν_2, the fit contains both frequencies.
This varying appearence of the ESEEM shape for the two transitions is still under investigation [21]. The comparison of the measurements on ν_1 and ν_2 in several samples in this work revealed no significant difference between the T_2 times extracted from the ESEEM fits. Therefore, the exact origin of the difference in shape of the ESEEM signal is neglectable for the T_2 time measurements in this work.
In contrast to the electron irradiated samples, the measurement of the T_2 time of V_{Si} defects in the neutron irradiated sample does not show ESEEM. The decay of the spin echo is too fast to observe the ESEEM modulations. In case of T_2 times significantly shorter than the periods of the ESEEM an exponential fit is therefore sufficient.
In the following, the influence of irradiation particle type and emitter density on T_2 is discussed. For a better overview, at first only the sample series S1 and S2, as well as the neutron irradiated sample A2 before and after annealing are presented. Their T_2 times extracted from ESEEM or exponential fits as a function of N_V are plotted in fig. 6.13.

For the investigated range of N_V, the T_2 time of V_{Si} created with electron irradiation is significantly longer than that of neutron irradiated samples. As described in 3.2, the main interaction of the penetrating electrons in the crystal is with crystal electrons, while the main interactions of the neutrons are collisions with lattice atoms. The decelarated electrons and secondary electrons possess lower energies than the neutrons when colliding with crystal atoms and hence create less severe crystal damage and a higher percentage of small defects like V_{Si}. The neutrons, on the other hand, create a significant percentage of defects other than V_{Si}. This leads to an increase of spin-spin interactions of V_{Si} with other spin active defects, resulting in irreversible processes during de- and rephasing and a diminishing of T_2.

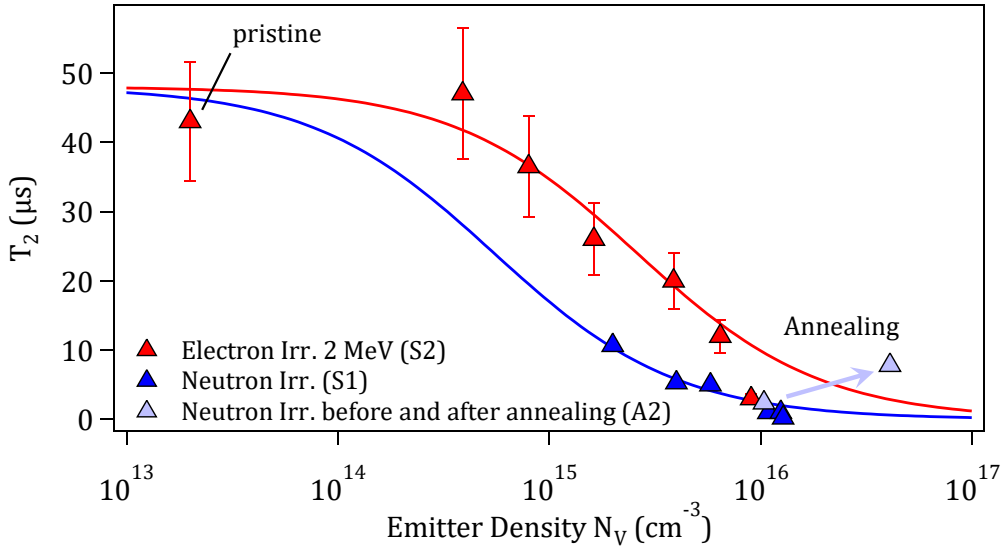

Figure 6.13.: Spin coherence time T_2 as a function of the emitter density N_V in the sample sets S1 and S2 and in sample A2 before and after annealing. The solid lines are fits to eq. 6.7.

The second cause that is evident from fig. 6.13 is that the T_2 time in both neutron and electron irradiated samples depends heavily on N_V. This is consistent with the results in other related material systems, such as NV^- centers in diamond. A detailed look at the exact causes of decoherence is necessary to understand this behaviour.
The spin decoherence is governed by interactions with the surrounding spin bath of nuclei (^{29}Si,^{13}C) $1/T_2^{(n)}$, paramagnetic centers (particularly ^{14}N) $1/T_2^{(p)}$ as well as residual (particularly carbon vacancies) $1/T_2^{(r)}$ and irradiation induced defects $1/T_2^{(i)}$ [100], [21], [102]. The resulting spin decoherence rate is then $1/T_2 = 1/T_2^{(n)} + 1/T_2^{(p)} + 1/T_2^{(r)} + 1/T_2^{(i)}$. It was shown that $1/T_2^{(n)}$ is supressed by applying a moderate magnetic field. In case of V_{Si} defects in 4H SiC 15 mT are sufficient [22],[100]. The rate $1/T_2^{(i)}$ takes the density N_Ω of all irradiation induced spin active defects into account. In the following, it is assumed that N_Ω scales with N_V in both electron and neutron irradiated samples for $N_V < 10^{16}\,\mathrm{cm}^{-3}$, which is backed up by the results of the EPR measurements in 4.3. Under this assumption, T_2 as a function of N_V can be described by

$$T_2 = \frac{T_2^{(\mathrm{pristine})}}{1 + T_2^{(\mathrm{pristine})} \kappa N_V} \tag{6.7}$$

with the spin coherence time $T_2^{(\mathrm{pristine})}$ in a non irradiated crystal given by the presence of paramagnetic centers $1/T_2^{(p)}$ and residual defects $1/T_2^{(r)}$. Hence, $T_2^{(\mathrm{pristine})}$ is only depending on the intrinsic properties and quality of a wafer. The assumed proportionality $T_2^i = \kappa N_V$ is in theory universally valid for a certain irradiation particle

type.
For low emitter densities $N_V < 7 \times 10^{14}\,\mathrm{cm}^{-3}$ in the electron irradiated samples, T_2 does not show any notable dependence on N_V. In the range $7 \times 10^{14}\,\mathrm{cm}^{-3} < N_V < 7 \times 10^{15}\,\mathrm{cm}^{-3}$ the change of T_2 is well described by the fit (solid line) according to eq. 6.7. For $N_V > 7 \times 10^{15}\,\mathrm{cm}^{-3}$ a deviation from the fit towards lower values is observed which correlates with the T_1 shortening in fig. 6.10. The data is well fitted with $T_2^{(\mathrm{pristine})} = 48\,\mu\mathrm{m}$ for electron and neutron irradiated S1 and S2 samples. As fit parameters κ_e and κ_n for the electron and neutron irradiated samples

$$\kappa_e = 0.8 \times 10^{-11}\mathrm{s}^{-1}\mathrm{cm}^3 \quad \text{and} \quad \kappa_n = 3.8 \times 10^{-11}\mathrm{s}^{-1}\mathrm{cm}^3$$

are obtained, respectively, from the fits in fig. 6.13. A very positive result occured in the heavily neutron irradiated and subsequently annealed sample A2. The spin coherence of the V_{Si} was increased by a factor of more then 3. The exact procedure as well as a detailed discussion of the results of sample annealing follows in 7.
To put the results obtained in S1 and S2 into perspective, the T_2 times in fig. 6.13 are compared to the T_2 times of V_{Si} in a variety of samples with different properties to investigate the validity of equation 6.7 with regards to changes of the manufacturing parameters, like particle energy or wafer quality. For this purpose T_2 of a proton irradiated sample (P5), two neutron irradiated samples (N1 and N2) of a different wafer and electron irradiated samples (E1 and E2) with varying energies were measured. The results are further compared to the results of other groups, including $T_2 \approx 100\,\mu\mathrm{s}$ of a single V_{Si}, $T_2 = 81 \pm 4\,\mu\mathrm{s}$ in an ensemble in another HPSI 4H-SiC wafer irradiated with an electron fluence of $\Phi_e = 5 \times 10^{17}\,\mathrm{cm}^{-2}$ and $T_2 = 22 \pm 5\,\mu\mathrm{s}$ in a proton irradiated sample with a fluence of $\Phi_p = 1 \times 10^{14}\,\mathrm{cm}^{-2}$ [21],[26],[103]. The results are presented in fig. 6.14.

As in case of the T_1 time, no significant dependence of T_2 on the electron energy can be observed. This suggests that the interactions between electrons and crystal and therefore the ratio of created defect types does not change with the electron energy. This is of importance when aiming for high emitter densities with electron irradiation, because it enables faster defect creation with the same fluence. Furthermore, this provides the possibility to create defect ensembles with homogeneous defect distribution in large samples with electron irradiation due to the higher penetration depth of fast electrons.
The spin coherence was reported to be longer for the single V_{Si} defect. In an epitaxial 4H-SiC layer with $N_V \approx 10^{11} - 10^{12}\,\mathrm{cm}^{-3}$, the isolated V_{Si} showed coherence for $T_2 \approx 100\,\mu\mathrm{s}$ [26]. Another HPSI 4H-SiC wafer after electron irradiation $\Phi_e = 5 \times 10^{17}\,\mathrm{cm}^{-2}$ gives $T_2 = 81 \pm 4\,\mu\mathrm{s}$ [21]. As N_V was not reported for this wafer, the same creation

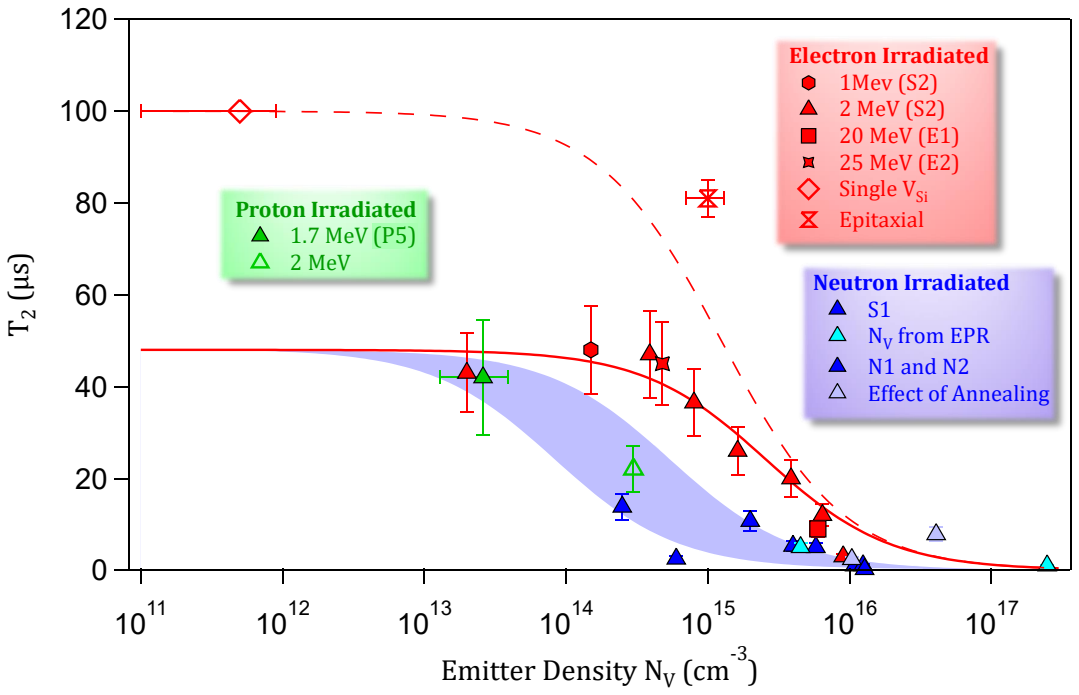

Figure 6.14.: T_2 of V_{Si} in various samples irradiated with different particles, fluences and energies. The red solid line, the red dashed line and the blue area are fits to eq. 6.7.

yield as in fig. 5.3 is assumed, which gives $N_V \approx 10^{15}\,\mathrm{cm}^{-3}$. The longer coherence time is likely related to a lower concentration of intrinsic paramagnetic centers and hence longer $T_2^{(\mathrm{pristine})}$ compared to that in the non-irradiated wafer in this work. The effect of a prolonged $T_2^{(\mathrm{pristine})}$ is indicated by a fit, represented by the red dashed line, with the same κ_e as for sample set S1.

The neutron irradiated samples from another SiC wafer are not in agreement with the fit parameter κ_n for neutrons obtained from sample set S2. They are well fitted with $\kappa_n = 25.2 \times 10^{-11}\mathrm{s}^{-1}\mathrm{cm}^3$, which is one order of magnitude higher than κ_n of S2. Therefore, the fit of the T_2 times of the V_{Si} defects generated by neutron irradiation is shown as a light blue area limited by the fitting curves with $\kappa_n = 3.8 \times 10^{-11}\mathrm{s}^{-1}\mathrm{cm}^3$ and $\kappa_n = 25.2 \times 10^{-11}\mathrm{s}^{-1}\mathrm{cm}^3$, representing a regime in which κ_n is presumed.

Now, the aforementioned results are compared to the spin coherence time in proton irradiated samples. Due to their small mass it is expected that the irradiation induced damage of the crystal is weaker when compared to ions of heavier atoms. From this point of view, it is advantageous to use protons to create highly coherent V_{Si} defects, since a less severe damage is likely to lead to less non V_{Si} defects capable of shortening T_2.

The T_2 time was measured on a spot of ≈ 70 V_{Si} defects that was proton beam writ-

ten in sample P5. The measurement of T_1 and T_2 on this sample is discussed in detail in 6.4. From the geometry of the written spot, the emitter number and the shape of the collection volume, an emitter density of $N_V \approx 3 \times 10^{13}\,\mathrm{cm}^{-3}$ was calculated, which is in the regime of a very moderately electron irradiated sample. The coherence time $T_2 = 42 \pm 20\,\mu\mathrm{s}$ consequently approaches that in the pristine wafer $T_2^{(\mathrm{pristine})} = 48\,\mu\mathrm{s}$ [80]. It was found in another work that T_2 decreases with increasing Φ_p and N_V. For $\Phi_p = 1 \times 10^{14}\,\mathrm{cm}^{-2}$ with estimated emitter density $N_V = 3 \times 10^{14}\,\mathrm{cm}^{-3}$, a spin coherence time of $T_2 = 22 \pm 5\mu\mathrm{s}$ from a stretched exponential fit was reported [103].

In fact, the process of defect generation by ions poses an obstacle with regards to the establishment of a universal equation similar to eq. 6.7 for one complete sample. As described in 3.2.3, ions create defects at a certain penetration depth in the crystal, at the position of the Bragg peak. This consequently leads to a gradient in the defect and the V_{Si} density. The V_{Si} defects at the Bragg peak have the shortest T_2 time due to the high local N_V. However, V_{Si} defects at more shallow depths show longer T_2 times [104]. This requires a more complex description of the dependence of the spin coherence on the proton (or any other ion) irradiation fluence compared to electron or neutron irradiation. Nonetheless it is expected that eq. 6.3 can still be used for ion irradiation, athough the parameter κ should depend on the ion type and energy as well as on the depth under the irradiated surface.

The last two chapters were dedicated to the influence of the three most common methods used for the creation of crystal defects in SiC - namely particle irradiation with neutrons, electrons or protons - on the emitter density and the V_{Si} coherence properties in a wide range of irradiation fluences. When aiming for an ensemble with homogeneous, high N_V created in a reasonble amount of time, neutron irradiation should be the method of choice. The neutrons' higher creation yield compared to the one of electrons allows faster defect creation with homogeneous distribution in large bulk samples. In fact, the creation yield in the experiments presented in this work is even underestimated, as shown by the analysis via quantitative EPR. If the coherence properties are crucial for the planned application, electron irradiation represents the better alternative. It creates highly coherent V_{Si} with longer T_2 for given N_V compared to neutron irradiation. It further turned out that an increase of the electron energy is not detrimental to T_2, giving potential for faster creation of V_{Si} with long spin coherence and the creation of a homogeneous distribution in thick samples with electron irradiation. When both the emitter density and the spin coherence are beneficial for an application, as is the case for quantum sensing, a compromise between both methods has to be found. In order to be able to find a suitable combination of N_V and the spin coherence, T_1 and T_2 were measured as a function of the emitter density. While T_1 is

robust up to high fluences, T_2 shows strong dependence on the emitter density. By using eq. 6.7, T_2^{pristine} is sufficient information to create a V_{Si} ensemble with predictable N_V and T_2. This provides the opportunity of custom made V_{Si} fabrication for a specific task.
Further, it was shown that proton irradiation is a viable method for the creation of highly coherent V_{Si} at a desired location. It hence offers the option of controlled and targeted V_{Si} creation in already existing electronic or optic structures.
The results in chapters 5 and 6 can be used as a manual for all research groups or companies aiming for V_{Si} in SiC with destinct properties for a specific application. Knowledge of this kind is essential and of great value for everyone involved with or depending on irradiation induced V_{Si} defects in SiC for quantum applications.

6.4. Spin coherence of silicon vacancies created via proton beam writing

As could be shown above, neutrons create more crystal damage than electrons due to their higher mass. Furthermore, they create a higher percentage of non V_{Si} due to the nature of their interaction with the crystal: While electrons primarily interact with the crystal electrons because of their charge, the uncharged neutrons mainly collide with the lattice atoms and considerably damage the crystal, resulting in all kinds of defects. This results in a significantly shorter T_2 time of V_{Si} created by neutron irradiation. Since protons are charged on the one hand, but also have a mass comparable to that of neutrons on the other hand, it is not trivial to predict the spin coherence of V_{Si} defects created by proton irradiation. Nonetheless, this is a crucial property when aiming for spin-active defects in an opto-electronic structure, which is the purpose of ion irradiation in the first place.
Therefore, T_1 and T_2 of V_{Si} in a PB written spot were measured by means of pODMR. In contrast to the measurements of T_1 and T_2 in large ensembles in the electron or neutron irradiated samples in 6, here only a small number of $\approx 70 V_{Si}$ is probed. Therefore, the ZfSetup was modified as explained in 4.6. The results of this section are shown as data points for protons in figs. 6.10 and 6.14 (green closed triangles).
Before measuring T_1 and T_2, cwODMR was measured to ultimately verify that the PB written defect spots consist of V_{Si} and to calibrate the frequency of the RF pulses. Fig. 6.15 shows the cwODMR spectrum of the PB written spot at $B = 0\,\text{mT}$ and at $B = 15\,\text{mT}$.

At $B = 0\,\text{mT}$, the fingerprint resonance peak at the ZFS = 70 MHz of the V_{Si} can be observed. As expected, the peak splits into two resonance peaks, ν_1 and ν_2, due to

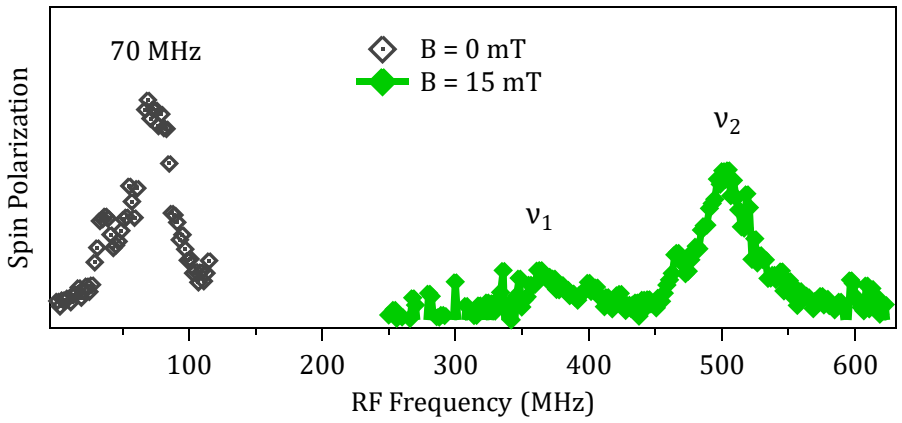

Figure 6.15.: cwODMR spectrum measured on a spot of ≈ 70 V_{Si} at $B = 0\,\mathrm{mT}$ and $B = 15\,\mathrm{mT}$. The spectrum at zero field shows the characteristic ZFS of the V_{Si} at 70 MHz. With a magnetic field, the peak splits due to Zeeman interaction.

Zeeman interaction.

Rabi oscillations at the ν_1 transition are measured by means of pODMR using the pulse sequence presented in 6.1.2. The resulting graph is shown in fig. 6.16.

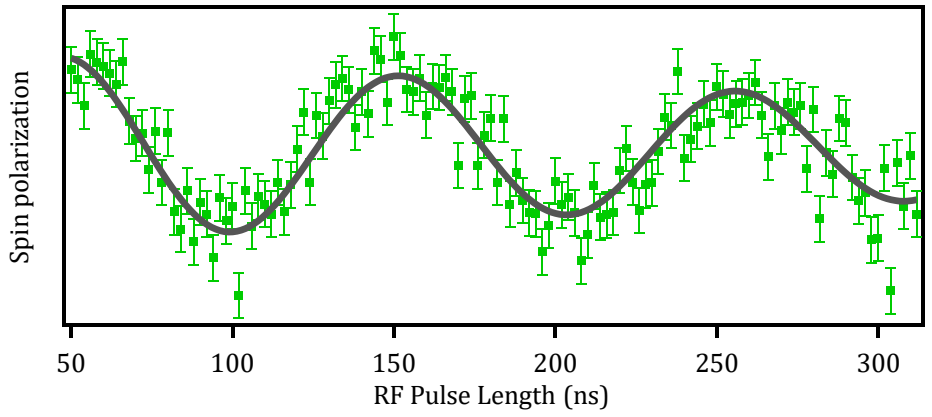

Figure 6.16.: Coherent control of a spot of ≈ 70 V_{Si} at $B = 15\,\mathrm{mT}$ performing RF driven Rabi oscillations.

From the Rabi oscillations, the length of the $\pi/2$-, π- and $3\pi/2$-pulse were derived. Subsequently, T_1 and T_2 were measured. The plots are presented in fig. 6.17.

The T_1 time is only marginally shorter than for an intact crystal. Interestingly enough, $T_2 = 42 \pm 20\,\mu\mathrm{s}$ is comparable to that of a pristine crystal as described in 6.3, although the protons are still in the direct vicinity of the V_{Si}. For the estimation of the emitter

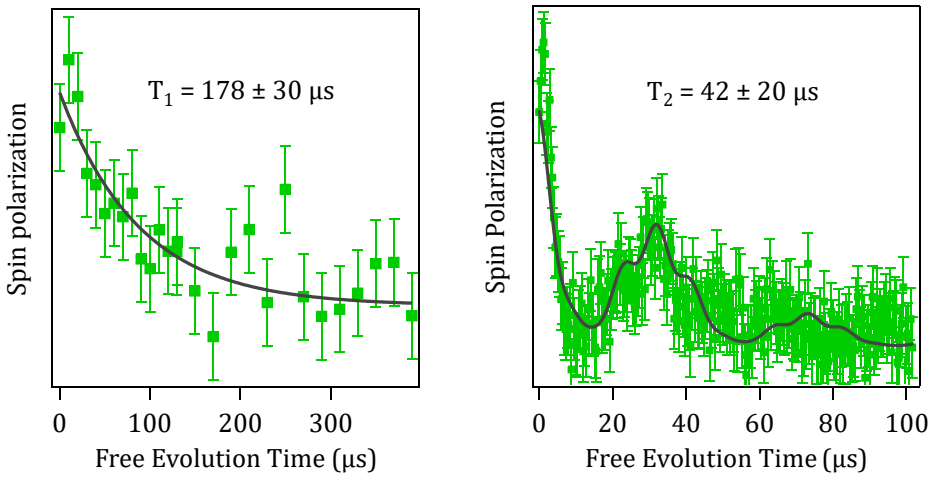

Figure 6.17.: Measurement of T_1 and T_2, measured on a spot of ≈ 70 V_{Si} at $B = 15$ mT. **left:** Exponential decay of the spin polarization with T_1. Although the V_{Si} density is close to that in a pristine crystal, the T_1 time is slightly shortened compared to T_1 of a pristine crystal. **right:** Decay of the spin polarization due to decoherence. The black solid line is an ESEEM fit.

density in the spot, the laser focus geometry and the number of observed emitters was taken into account. Based on this $N_V = 2.6 \pm 1.2 \times 10^{13}\,\mathrm{cm}^{-3}$ was determined. When put into perspective, this corresponds to the density in a very moderately electron-irradiated, almost pristine commercial crystal. The long spin coherence is likely to be related to that very low defect density. Strikingly, the naturally created proton impurities have no discernable influence on the coherence.

These results show, that targeted PB writing can create highly coherent V_{Si} spin defects in a simple, point-and-shoot fashion. This can be utilized for the application-oriented manufacturing of hybride spin-electronic, spin-photonic, and spin-mechanic quantum nanodevices based on the technologically friendly SiC platform.

7. Influence of annealing on the silicon vacancy optical and spin properties

Crystal annealing has been proven to be able to heal certain types of defects, thereby reducing the spin-spin interactions of V_{Si} with the environment and ultimately slowing down their dephasing [53]. As previously mentioned, a high V_{Si} density combined with long spin coherence is desirable for various applications. In an effort to prolong T_2 while maintaining N_V, several irradiated samples were annealed in the course of this work to explore the influence on both N_V and T_2 of the contained therein V_{Si} defects. The results of this chapter were published in [90].

In general, the term "annealing" describes a process in which a material is heated and then cooled down again. This can help to achieve certain material properties, like higher ductility or in the case of tempering, a change of the distribution of mechanical stresses in a component. In addition to these applications, it is also well established in semiconductor technology for the healing of unwanted crystal defects. Here, the increased mobility of the crystal atoms causes them to return to the energetically most favorable configuration, which is in most cases the perfect crystal. In practice, this means, for example, that a wrongly positioned atom moves through the crystal due to the thermal energy provided by annealing until it meets its correct lattice site, thus wiping out two defects at once.

Although in the case of quantum applications in SiC crystal defects are not unwanted, but explicitly desired, not all crystal defects are necessary. Quite the opposite: Since crystal defects represent deviations from the ideal lattice and can be spin active, they have an impact on the coherence of the V_{Si} defects, as was demonstrated in the last chapter in the case of V_{Si} created by neutron irradiation. Especially the spin-spin interactions can result in a deterioration of the T_2 time. To fathom the effect of a reduction of non V_{Si} defects on the coherence properties of a V_{Si} ensemble, two heavily neutron irradiated samples, A1 and A2, with $\Phi_n = 1 \times 10^{18}\,\mathrm{cm}^{-2}$ and corresponding $N_V = 1 \times 10^{16}\,\mathrm{cm}^{-3}$ were annealed with two different annealing protocols. Addi-

tionally, an electron irradiated sample A3 with $\Phi_e = 1 \times 10^{18}\,\mathrm{cm}^{-2}$ and corresponding $N_V = 6.1 \times 10^{15}\,\mathrm{cm}^{-3}$ was annealed. In a systematic analysis, the emitter density N_V, the absorption α as well as T_1 and T_2 were determined after each annealing step.
The selective healing of individual crystal defect types is only possible because different defect types heal in different temperature regimes. In the case of the V_{Si} defects this temperature regime starts above 500 °C [53]. At around 750 °C, the majority of V_{Si} goes over into the more stable $C_{Si}V_C$ defect pair, where a next neighbour carbon atom moves onto the V_{Si} defect and occupies it, while the carbon lattice site stays vacant [78]. This temperature dependent healing of different defect types provides the possibility of selective defect healing. However, it is only possible to anneal defects possessing a lower annealing temperature than the V_{Si} defects while remaining N_V.
Taking this into account, annealing protocols with destinct annealing times t_{ann} and annealing temperatures T_{ann} were applied to the samples A1 – A3: In the protocol for A1, the sample was annealed several times at a constant temperature of 500 °C, while sample A2 was annealed in several steps with increasing temperature during the protocol for sample A2. Electron irradiated sample A3 was annealed in two steps. The three protocols are shown in fig. 7.1.

7.1. Emitter density and absorption

First, the influence of sample annealing on N_V was examined via PL measurements. The upper left graph in fig. 7.2 shows the PL spectrum of sample A1 before and after the complete annealing protocol.

The PL intensity in A1 increases drastically after annealing. However, the annealing procedure does not create additional emitters, but the PL of already existing potential emitters is "exempted", which leads to an increased N_V. As mentioned earlier, defects other than V_{Si} can provide non-radiative recombination paths for the V_{Si} defects, especially in neutron irradiated samples. By healing of some of these irradiation induced and intrinsic defects, the V_{Si} can subsequently recombine radiatively and N_V increases. The lower left and right plots in fig. 7.2 show the corresponding emitter density N_V as a function of the annealing time t_{ann} and temperature T_{ann}, respectively. Astoundingly, an increase by a factor of 4 after optimum annealing conditions was achieved, already hinting at the huge potential of sample annealing in terms of removing unwanted crystal defects, which will be extended in the following sections.
No increase in PL was observed in the annealed electron irradiated sample (upper right plot in fig. 7.2). This supports the previous observation in 6.3 that neutrons produce a higher percentage of non V_{Si} defects which can lead to quenching. Since these de-

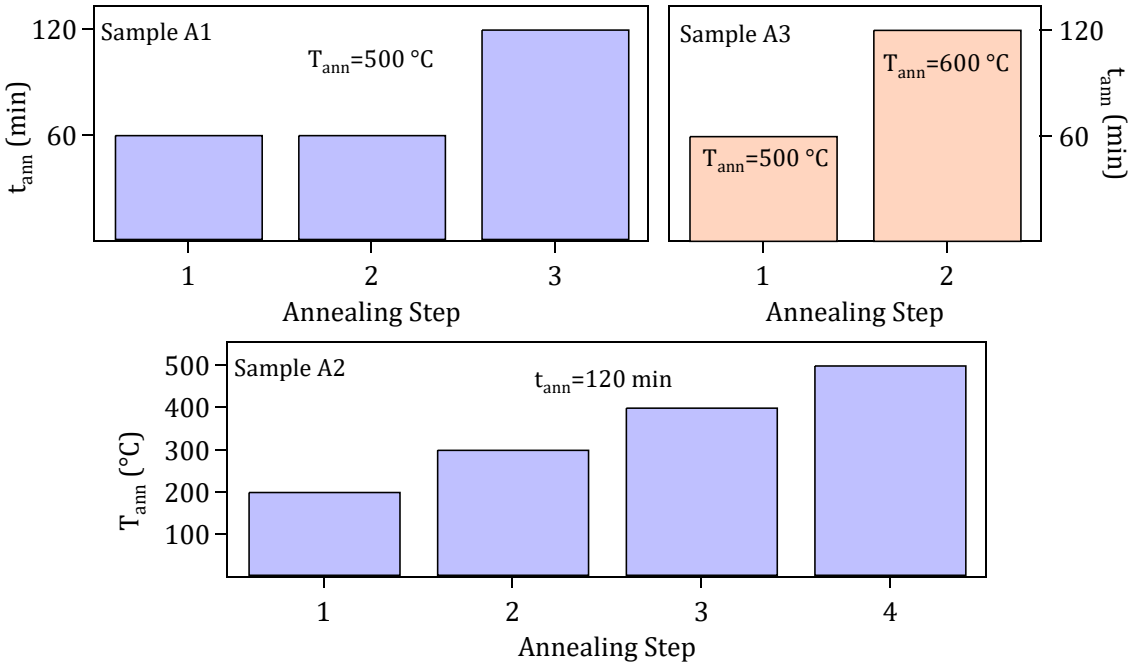

Figure 7.1.: Annealing protocols of samples A1–A3. Samples A1 and A2 were prior irradiated with a neutron fluence of $\Phi_n = 1 \times 10^{18}\,\mathrm{cm}^{-2}$, resulting in an emitter density of $N_V = 1 \times 10^{16}\,\mathrm{cm}^{-3}$. Sample A3 was irradiated with an electron fluence of $\Phi_e = 1 \times 10^{18}\,\mathrm{cm}^{-2}$ with corresponding $N_V = 6.1 \times 10^{15}\,\mathrm{cm}^{-3}$. **top left:** Sample A1 was annealed with constant annealing temperature $T_{\mathrm{ann}} = 500\,^{\circ}\mathrm{C}$ **bottom:** Sample A2 was annealed with gradually increasing temperature. **top right:** Sample A3 was annealed in two steps of $T_{\mathrm{ann}} = 500\,^{\circ}\mathrm{C}$ and $T_{\mathrm{ann}} = 600\,^{\circ}\mathrm{C}$.

fects were not present in significant numbers in the electron- irradiated sample from the outset, no difference in PL after annealing is apparent. The PL of the electron irradiated sample in this work even dropped slightly after annealing, as can be seen in the lower part of fig. 7.2. This hints at a healing of some V_{Si} defects already at 500 °C [105]. This effect must also be assumed in the neutron-irradiated sample, which, however, is overlaid by the much more significant healing of PL-quenching defects.

Another consequence of sample annealing is the reduction of the absorption due to the healing of optically active, absorbing defects. In order to investigate the extent of the absorption decrease, absorption profiles of the samples were measured by conducting a confocal z-scan at the LabRam setup. In such a z-scan, the laser light is absorbed on its path to the focus, as well as the PL from the focus back to the objective. The profile of sample A1 before and after the complete annealing protocol are presented on the left of fig. 7.3.

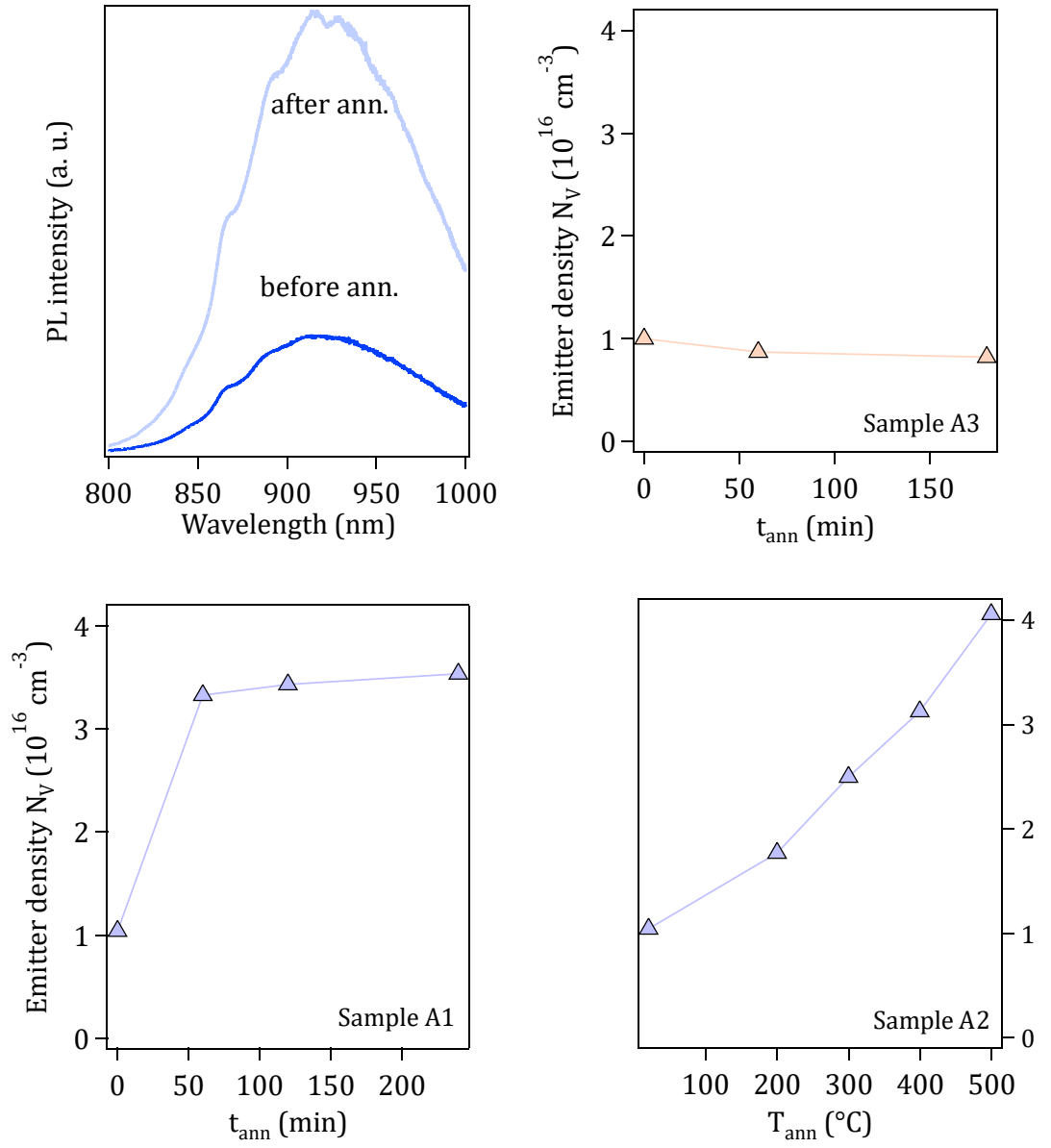

Figure 7.2.: Effect of annealing on the PL emssion of three V_{Si} ensembles. **top left:** PL spectrum of sample A1 before and after annealing. **top right:** Variation of N_V obtained from the integrated PL intensity in sample A3 induced by annealing. **bottom left:** N_V in A1 as a function of the annealing time at $T_{ann} = 500\,°C$. **bottom right:** N_V in A2 as a function of the annealing temperature for $t_{ann} = 120\,min$.

The absorption coefficient α can be deduced from an exponential fit of the form $PL(z) = PL_0 e^{-\alpha z}$. The absorption coefficient α is a combination of the absorption coefficient of the laser light and the absorption coefficient of the emitted PL. Nevertheless,

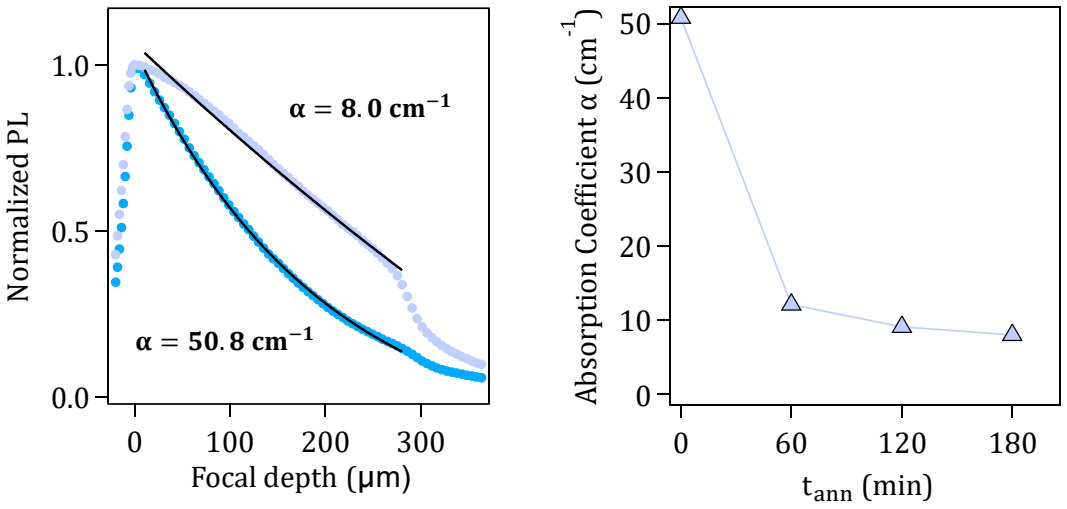

Figure 7.3.: Influence of sample annealing on the optical absorption **left:** Absorption profiles of sample A1 before and after the complete annealing protocol. The absorption coefficient drops from $\alpha = 50.8\,\mathrm{cm}^{-1}$ to $\alpha = 8.0\,\mathrm{cm}^{-1}$. **right:** Absorption coefficient of sample A1 as a function of the annealing time t_{ann}.

α provides a valid method to compare the absorption before and after annealing.
By healing of optically active, light absorbing defects other than V_{Si} during annealing, the absorption coefficient dropped from $\alpha = 50.8\,\mathrm{cm}^{-1}$ to $\alpha = 8.0\,\mathrm{cm}^{-1}$. This underpins the impact of sample annealing on the density of non V_{Si} defects. The coefficient α as a function of the annealing time is presented on the right side of fig. 7.3. It shows that the absorption coefficient saturates already after one hour of annealing.
The reduction of absorption in this reasonable time is a positive side effect of annealing. In various applications, optical accessability of V_{Si} deep below the sample surface is required. A high absorption coefficient is a huge hurdle for applications of this kind, which, however, can be conveniently removed by annealing the sample. In chapter 5, proton beam written defects in greater depth were examined. Small ensembles or even single defects emit low PL intensity. Losses due to light absorption can therefore hamper the perfomance of optically read out quantum sensors or qubits. Also here sample annealing provides a convenient method to reduce the absorption and is a valid approach to enable and improve optical access of defects in 3D structures, even in greater depths.
After exploring the impact of annealing on the optical properties of the SiC crystal and the V_{Si} defects the next three sections cover the influence on the spin properties.

7.2. ODMR spectrum

In order to verify the existence of V_{Si} after annealing and to calibrate the frequency of the RF pulses for the pODMR with the goal of obtaining T_1 and T_2, cwODMR spectra of sample A1 were recorded after each annealing step. The ODMR spectra are presented in fig. 7.4.

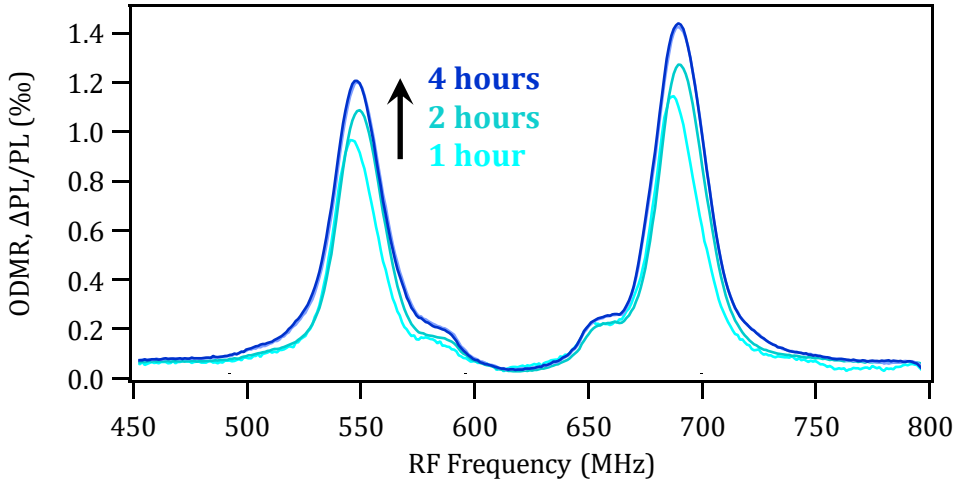

Figure 7.4.: cwODMR spectrum of sample A1 after each annealing step. A slight increase in contrast is observable. The position of the resonance peaks is unchanged.

The ODMR contrast slightly increases. This is probably associated with the healing of NIR emitters other than V_{Si}. A reduction in total PL maximizes $\Delta PL/PL$ and leads to an increased ODMR contrast. This effect is much weaker than the effect of annealing on the PL emission or the absorption, suggesting that the majority of defects responsible for quenching or absorption do not emit PL in the NIR themselves. On the other hand, the position and general shape of the spectrum does not change significantly, hinting at a negligible influence of the annealing on the V_{Si} defects. With the verification of the existence of V_{Si} after annealing and the determination of the transition frequency for pODMR pulses, the preparations for exploring the coherence properties have been completed.

7.3. Spin lattice relaxation

As a next step the impact of sample annealing on the spin lattice relaxation time T_1 is studied. For this purpose the same pulse sequence as in 6.2 was utilized. The T_1 time

measured on the ν_2 transition of the V_{Si} defects in sample A3 as a function of t_{ann} is presented in fig. 7.5.

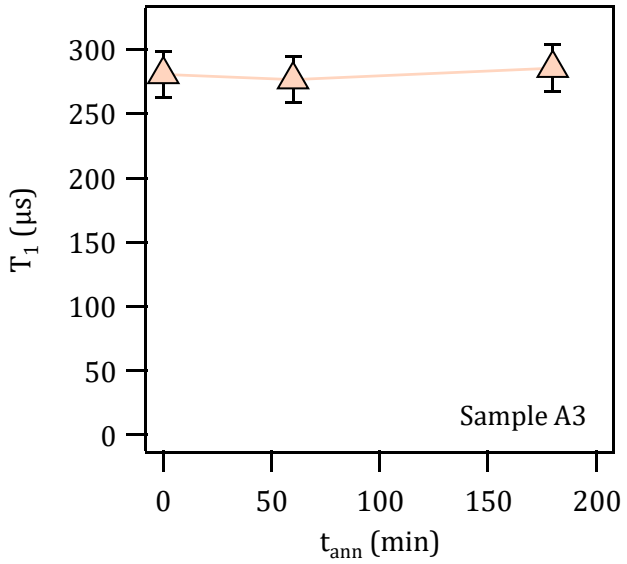

Figure 7.5.: T_1 as a function of t_{ann} in the electron irradiated sample A3. No apparent change in T_1 can be observed. The T_1 time is in accordance with the one measured in the samples with $N_V < 10^6\,cm^{-3}$ in 6.10.

In case of the electron irradiated sample no significant change in T_1 could be observed. This can be expected, since the T_1 time of the sample was in the range of an intact crystal ($\approx 300\,\mu s$, see 6.2) already before annealing. The density of intrinsic defects is so low, that the influence of cross relaxation A_0 (see eq. 6.5) on T_1 is insignificant and a further reduction has no effect. Hence, crystal healing did not prolong the T_1 time in the electron irradiated sample A3.
In the neutron irradiated samples A1 and A2, the T_1 time is significantly shortened by severe crystal damage caused by the irradiation. Fig. 7.6 shows T_1 in both samples as a function of t_{ann} or T_{ann}.

The T_1 time of the V_{Si} in these samples was substantially prolonged. In the case of sample A1, T_1 could be increased by 25 % from $124 \pm 14\,\mu s$ to $158 \pm 15\,\mu s$ after 4 hours at a temperature of 500 °C. In case of sample A2, an increase of even 35 % from $124 \pm 14\,\mu s$ to $171 \pm 16\,\mu s$ was achieved. Although T_1 increases, it is not completely restored to the value of $300\,\mu s$ as in the case of a pristine or moderately irradiated crystal. However, a part of the crystal damage leading to a reduction of the spin lifetime is recovered. Another finding of these results is that a slow increase in temperature is preferable to an abrupt strong heating with regards to the restoration of T_1. It should be noted, that T_1 saturates in sample A1, annealed at constant temperature, but not in sample A2, which was annealed with iteratively increasing temperature. For higher annealing tempera-

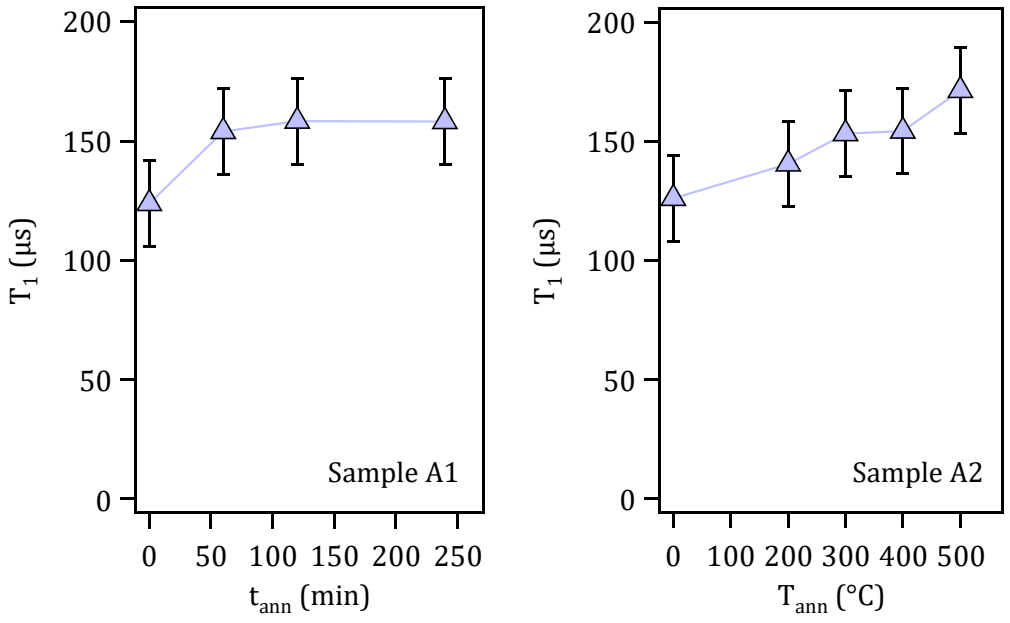

Figure 7.6.: T_1 of V_{Si} in the strongly neutron irradiated samples A1 and A2 as a function of t_{ann} or T_{ann}. In both cases, the T_1 time is partly restored, hinting at the healing of severe crystal damage and non V_{Si} defects.

tures, T_1 might increase further, but N_V would drop due to the healing of the V_{Si} defects.
In order to get even further insight, a sample of S1 moderately irradiated with neutrons and corresponding $N_V = 4 \times 10^{15}\,\mathrm{cm}^{-3}$ was annealed. The corresponding change of T_1 is displayed in fig. 7.7.

Although T_1 is already close to that of a pristine crystal, it is possible to even further prolong it, which means that before annealing defects were present that resulted in a diminishing of T_1. However, T_1 in fig. 6.10 is constant around $300\,\mu$s for neutron fluences way below the fluence this sample was irradiated with. This indicates, that the defects that cause a shorter T_1 before annealing are not irradiation induced. It rather suggests that the quality of the wafer was inferior and that the T_1 time of defects created in the wafer was shortened already from the beginning.
The T_1 time determines the limit of spin control. In order to discover the absolute potential of sample annealing, its influence on the spin coherence is investigated in the following.

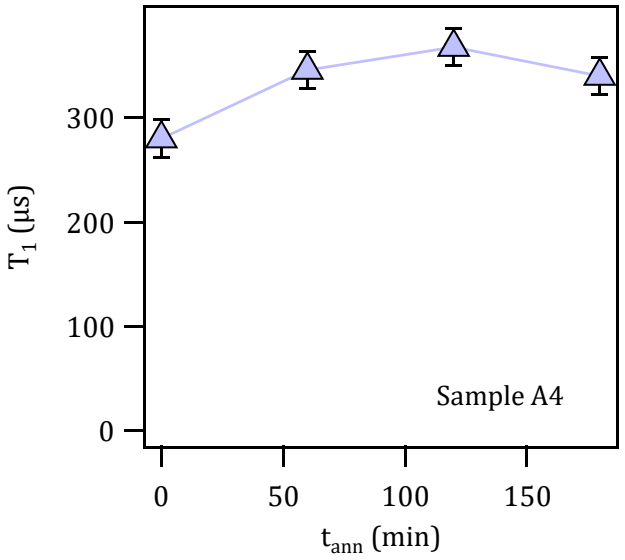

Figure 7.7.: T_1 as a function of t_{ann} in a sample of S2 irradiated with a neutrons and $N_V = 4 \times 10^{15}\text{cm}^{-3}$. A slight increase in T_1 is observable.

7.4. Spin coherence

As stated before, T_2 poses the time limit in which a spin state can be controlled and is in general much shorter than T_1. Hence, in order to actually have a positive impact on the usability of V_{Si} spins for quantum applications, the annealing process needs to result in a prolongation not only of T_1 but most importantly of T_2.
The T_2 times were obtained with the spin-echo-sequence, also used in 6.3. In analogy to the T_1 measurements, the RF pulses were resonant to the ν_2 transition of the V_{Si} defects. First, the influence of annealing on T_2 of the V_{Si} defects in the elctron irradiated sample A3 is discussed. The T_2 time as a function of t_{ann} is presented in the left plot of fig. 7.8.

As in the case of T_1, no significant change of T_2 can be observed. Since the projectile electrons, as mentioned before, mostly interact with crystal electrons and preferably create small defects like the V_{Si}, the percentage of defects other than V_{Si} is low compared to e.g. neutron irradiation. Hence, the spin coherence is mainly governed by interactions between V_{Si} and not by interactions of V_{Si} with other types of defects. A reduction of the already low density of non V_{Si} defects therefore has no noticable influence on the spin-spin- interactions responsible for decoherence. Therefore, an impact of annealing on the T_2 time of V_{Si} created by electron irradiation in this fluence regime cannot be observed. In principle, annealing can have an influence on the interactions between the V_{Si} defects, if the annealing temperature exceeds 500 °C and the density of V_{Si} is reduced. However, the goal of the annealing experiments in this work is to restore

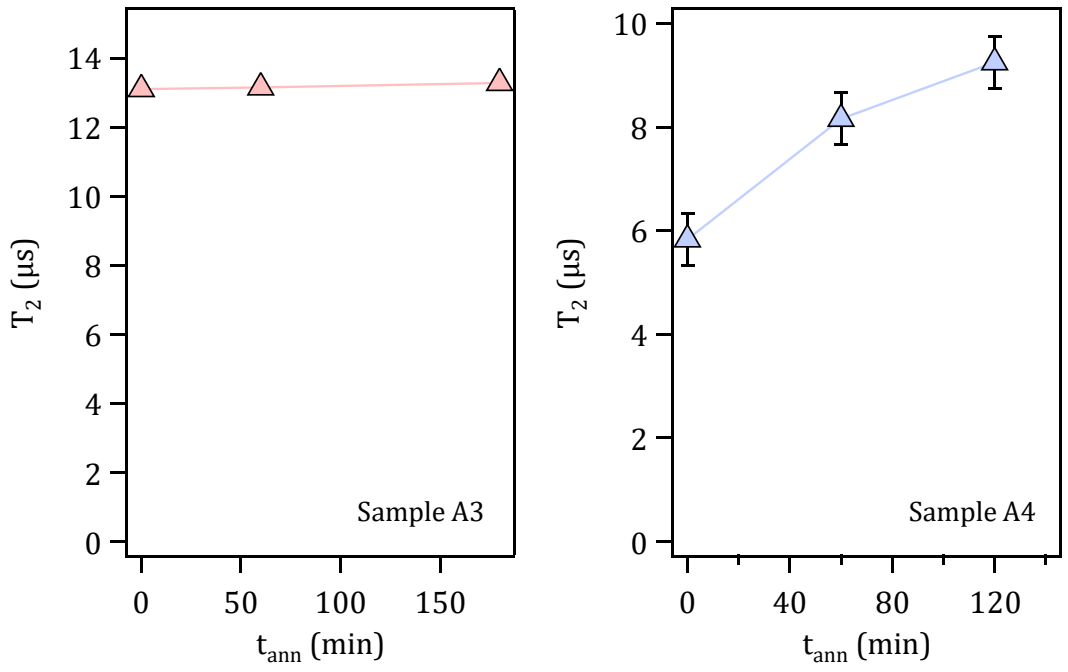

Figure 7.8.: Spin coherence time T_2 of V_{Si} as a function of t_{ann} in the electron irradiated sample A3 and the moderately neutron-irradiated sample A4. The annealing has no impact on the electron irradiated sample due to the low percentage of non V_{Si} defects created by electron irradiation. The T_2 time in the neutron irradiated sample increases by 50% due to the healing of some non V_{Si} defects.

the spin lifetime in samples with high emitter density, i.e. the density of V_{Si} should be preserved. A reduction of N_V by annealing and in this way the weakening of the interactions between V_{Si} to prolong T_2 is therefore not in the spirit of this approach.
Next the influence of annealing on the T_2 time in the mildly neutron irradiated sample A4 is examined. The right plot in fig. 7.8 shows T_2 as a function of the annealing time. In contrast to the electron irradiated sample, the T_2 time of the V_{Si} in the sample that was mildly neutron irradiated increases by 60% from $T_2 = 5.8 \pm 0.4\,\mu$s to $T_2 = 9.3 \pm 0.4\,\mu$s. As in the case of T_1, this is related to the different ways in which the defects are created by different types of irradiation particles. Due to the higher percentage of non V_{Si} defects created by neutron irradiation, interactions of these defects with the V_{Si} are a significant factor responsible for decoherence of the V_{Si} spins. Hence, the removal of a part of these defects prolongs T_2. The annealing procedure removes a part of spin defects with a healing temperature below 500 °C and eliminates interactions of V_{Si} with these defects. However, defects with a healing temperature higher than 500 °C are not removed and still cause decoherence. Thus, even after annealing, the neutron irradiated sample does not reach the T_2 time of an electron irradiated sample with similar

N_V, where T_2 of the hosting V_{Si} defects is mainly caused only by interactions between the V_{Si} spins.
Following this logic, the greatest effect of annealing on the spin coherence of V_{Si} should be expected in samples with a large amount of defects other than V_{Si}. This is the case in heavily neutron irradiated samples, like the samples A1 and A2. Fig. 7.9 shows the decay of the spin coherence of V_{Si} spins in sample A2 before and after the complete annealing protocol, fitted with ESEEM.

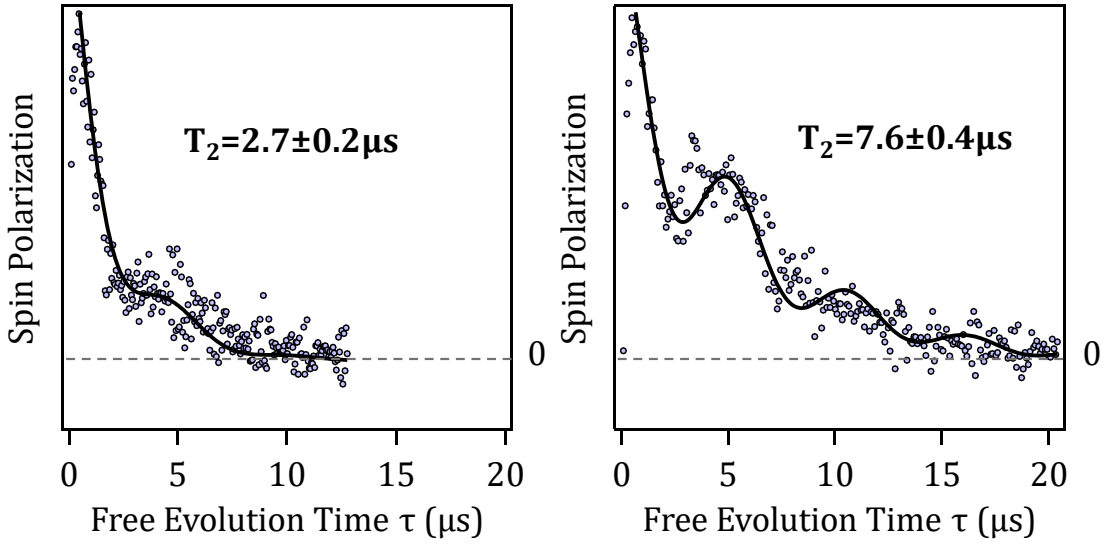

Figure 7.9.: Spin polarization as a function of the free evolution time τ in the strongly neutron irradiated sample A2 before and after annealing. T_2 was extracted from the ESEEM fit (black solid line).

The data clearly indicates an improvement of the spin coherence properties of the V_{Si} by annealing. An astonishing increase of the T_2 time by a factor of more than three from $T_2 = 2.7 \pm 0.4\,\mu$s to $T_2 = 7.6 \pm 0.4\,\mu$s was achieved. Compared to the moderately neutron-irradiated sample, the factor of increase is one order of magnitude higher. This can again be attributed to the higher number of non V_{Si} defects, that are healed below 500 °C. Fig. 7.10 shows T_2 as a function of annealing time or annealing temperature for the samples A1 and A2.

It becomes evident that, in analogy to the impact on T_1, a step-by-step increase of the temperature is preferable compared to an immediate annealing with 500 °C. This can be attributed to the fact, that for some defect types there exists an optimum annealing temperature regime [106]. When gradually increasing the temperature, at each temperature step there are defect types that are annealed most efficiently at that exact temperature. Thus, a larger number of defects other than V_{Si} is healed out compared to annealing with only one temperature.

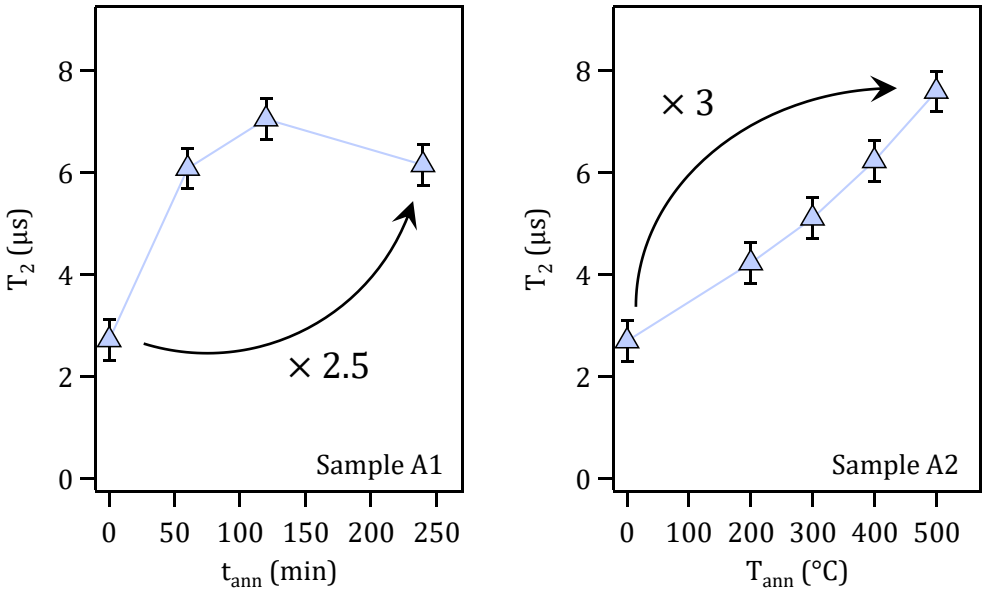

Figure 7.10.: T_2 of the V_{Si} in the strongly neutron irradiated samples A1 and A2 as a function of annealing time t_{ann} or annealing temperature T_{ann}. By healing out of non V_{Si} defects in both samples, T_2 could be significantly increased.

In case of sample A2 annealed with gradually increasing temperature, T_2 is not saturating in the presented data. However, similar to the case of T_1, a further temperature increase would lead to the healing of V_{Si} defects and would not satisfy the goal of high N_V with decent spin coherence. However, there is still room for improvement and some open questions to be solved in the future. One starting point can be the neutron irradiation of a sample to a N_V beyond the required value with subsequent annealing with temperatures higher than 500 °C. This would enable healing of more types of defects, while also healing out a calculated and bearable amount of V_{Si}.

In general, the results show a very positive effect of sample annealing on the V_{Si} in the neutron irradiated samples. A higher N_V, as well as prolongations of T_1 and T_2 were observed, showing a clear reduction of the interactions of the V_{Si} with other types of spin defects. Annealing did not only have an effect on V_{Si} in samples with high N_V, but also in the moderately irradiated sample A4, where annealing was advantageous for both the optical and coherence properties. Especially for sensing applications, requiring both a high N_V and a long spin coherence, sample annealing offers a significant enhancement of the V_{Si} properties.

These effects make sample annealing a universal tool, which, in combination with the results of ch. 5 and 6, provides manufacturers with additional options for optimization of the V_{Si} for specific tasks.

8. Coherent manipulation of silicon vacancies with sub-MHz spectral resolution

One of the challenges in the field of quantum sensing is to selectively address and coherently manipulate highly-homogeneous quantum systems subject to external perturbations. However, inhomogeneous broadening is a major bottleneck for the application of solid state spin systems, like the V_{Si} defect, for quantum sensing.
In this chapter spectral hole burning is used to spectrally isolate and coherently manipulate homogeneous spin packets in an ensemble of V_{Si} defects. The experiments were performed on a 6H-SiC (sample: H1) and 4H-SiC (sample: H2) with modified (^{29}Si 1 %, ^{13}C 1.1 %) isotope abundance. This was achieved by sample growth by means of the seeded physical vapour transport method with a ^{28}Si enriched precursor material [107].
In 8.1 the origin of inhomogeneous broadening is examined by means of two RF frequency ODMR and a model to describe the mechanisms of inhomogeneous broadening is developed. In 8.2 coherent control of a highly coherent V_{Si} spin packet is presented. The packet was selected and coherently driven by using two RF frequency pulsed ODMR. Finally, two-frequency Ramsey interferometry is performed to demonstrate absolute dc magnetometry, which is immune to thermal noise and strain inhomogenity. The results in this chapter were published in [108].

8.1. Origin of inhomogeneous broadening

In order to investigate the origin of inhomogeneous broadening in sample H1 two-frequency cwODMR was performed. In addition to the modulated probe RF frequency ν_{probe} a strong RF pump field at a fixed frequency ν_{pump} was applied. A cwODMR spectrum in the ^{28}6H-SiC sample H1 with and without pump RF field is presented in fig. 8.1.

The spectrum without ν_{pump} shows two inhomogeneously broadened ODMR lines. They are associated with the V3 and V2 V_{Si} defects in 6H-SiC and reveal the finger-

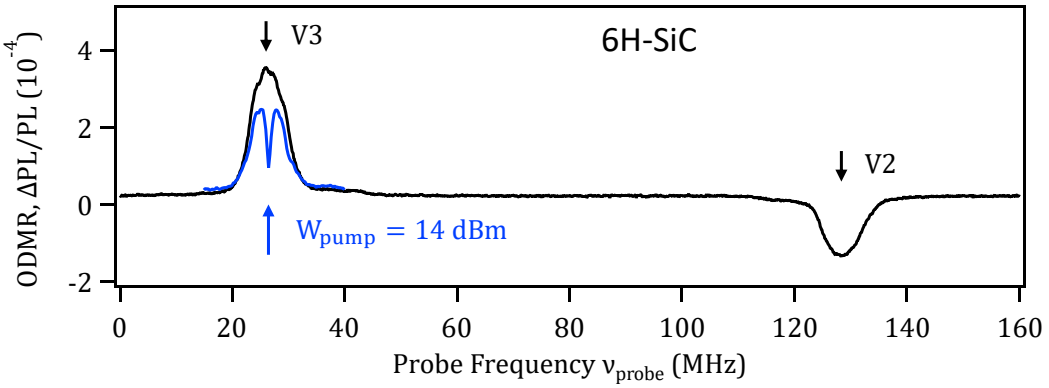

Figure 8.1.: ODMR spectrum of V_{Si} defects in 6H-SiC with one and two RF frequencies. The ODMR spectrum without a second frequency at ν_{pump} reveals the ZFS of the V2 and V3 V_{Si} defect. The pump RF field at $\nu_{pump} = 26.8\,MHz$ burns a hole into the resonance. The pump and probe powers are $W_{probe} = 7\,dBm$ and $W_{pump} = 14\,dBm$ correspondingly.

print ZFS of $2D_{V3} = 26.8\,MHz$ and $2D_{V2} = 128\,MHz$ between the $|\pm 3/2\rangle$ and $|\pm 1/2\rangle$ spin sublevels [78] [109]. In the spectrum with applied RF pump field a sharp minimum at ν_{pump} is present. This effect is well known as spectral hole burning [110] and is owed to the fact that the ODMR resonance is inhomogeneously broadened and agregates many homogeneous spin packets with different resonance frequencies. The pump RF field saturates the transition of the particular spin packet that is in resonance at ν_{pump}, which results in a reduction of the ODMR contrast $\Delta PL/PL$ at this frequency. The pump power (W_{pump}) dependence of the spectral hole is presented in 8.2.

With higher pump power, the hole at ν_{pump} becomes more pronounced. The pump-induced reduction of the ODMR contrast as well as the full width at half deep δ_{HB} increases with W_{pump}. The optimum power is found at $W_{pump} = 14\,dBm$. At this W_{pump} the depth of the spectral hole is approximately 30 % of the maximum ODMR contrast without second RF frequency, while the width is minimal at $\delta_{HB} = 1\,MHz$. This value of δ_{HB} is one order of magnitude lower than the linewidth of the inhomogeneously broadened ODMR resonance $\delta_{ODMR} = 7\,MHz$.
As a next step, the detection scheme is modified. For an increase of the sensitivity, the pump RF field was on/off modulated instead of the probe field in the following experiments. The frequency ν_{pump} was chosen at the resonance of the ZFS of the V3 V_{Si} defect. A resulting spectrum of this kind with ν_{probe} swept in the range of $2-60\,MHz$ is presented in fig. 8.3.

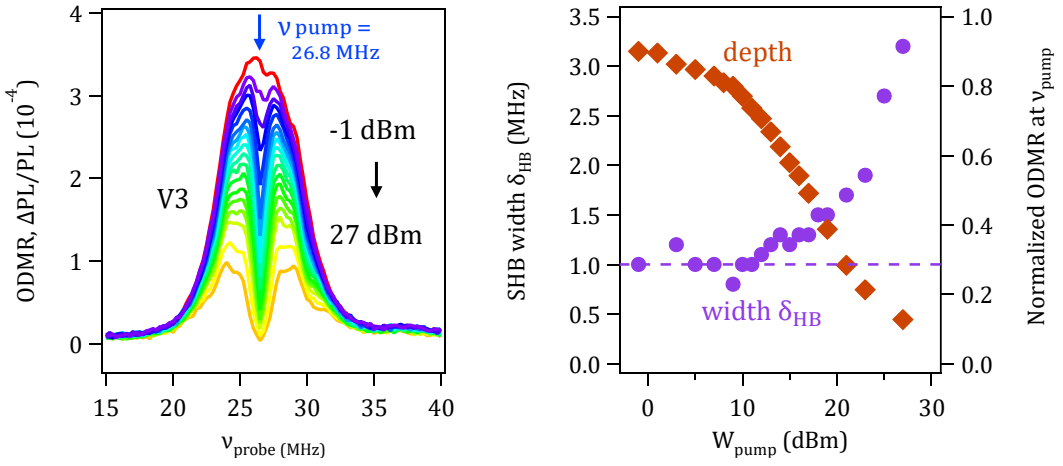

Figure 8.2.: Pump power dependency of SHB. **left:** SHB at the V3 spin resonance for different W_{pump}. **right:** Pump power dependency of the SHB width δ_{HB} and the normalized ODMR signal at $\nu_{\text{pump}} = 26.8\,\text{MHz}$. The horizontal dashed line indicates the limit of δ_{HB} for low W_{pump}.

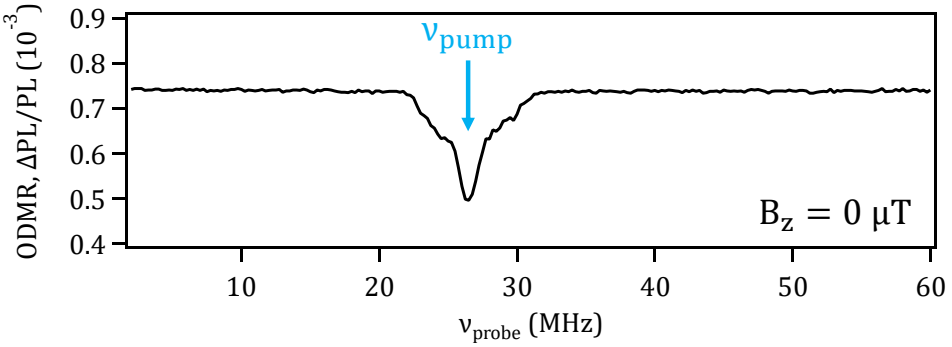

Figure 8.3.: Two RF frequency ODMR spectrum in 6H-SiC with on/off modulated ν_{pump}. The measurement was performed without external magnetic field. The pump frequency ν_{pump} is chosen at the center of the zero-field-transition corresponding to the V3 V_{Si} defect.

The ODMR contrast $\Delta PL/PL$ with $\Delta PL = PL_{\text{on}} - PL_{\text{off}}$ is derived from PL_{on} (PL when ν_{pump} is switched on) and PL_{off} (PL when ν_{pump} is switched off). The resonant transition at 26.8 MHz is saturated when ν_{pump} is switched on.

If ν_{probe} is **off resonant**: ν_{probe} does not have an influence on the detected ODMR contrast. The contrast is then governed by ν_{pump}. This manifests itself as a constant ODMR contrast baseline offset at 0.75×10^{-3}. If ν_{probe} is **in resonance**: PL_{off} is increased by ν_{probe}, which results in a minimum of the ODMR contrast at $\nu_{\text{pump}} = 26.8\,\text{MHz}$.

To further investigate the origin of inhomogeneous broadening of the resonances, a

small magnetic field B_z along the c-axis is applied. The behaviour of the ODMR spectrum in B_z gives information about the mechanism responsible for broadening. The most probable sources of inhomogeneous broadening are magnetic fluctuations (for instance, due to nuclear fields) and variations of the zero-field splitting (for instance, due to local strain). Fig. 8.4 shows two frequency ODMR spectra with modulated pump RF field on the V3 vacancy in sample H1 for several B_z.

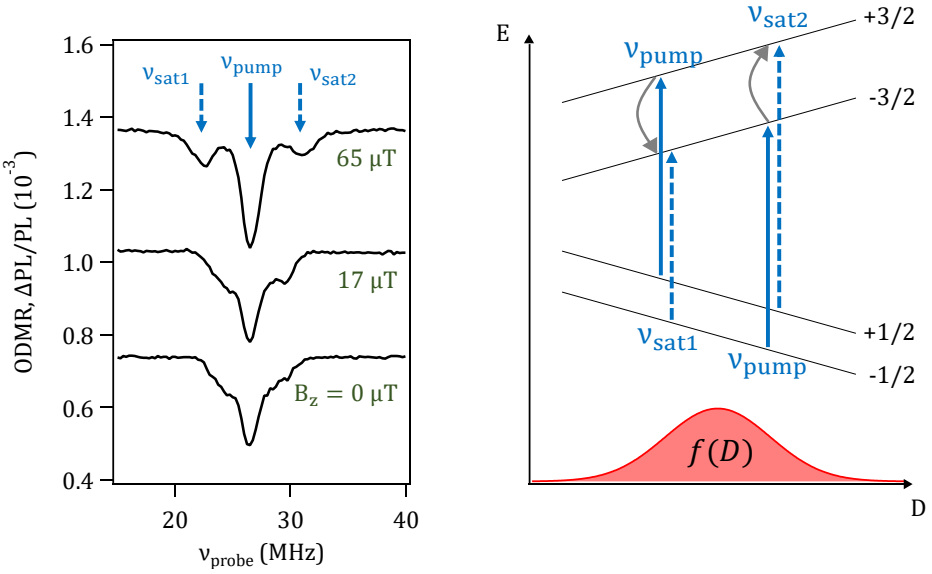

Figure 8.4.: Evolution of the satellite positions in a magnetic field B_z. **left:** Two RF frequency ODMR spectrum in 6H-SiC with on/off modulated ν_{pump} in several magnetic fields B_z. **right:** Schematic explanation of the SHB satellites, appearing at ν_{sat} due to the spin relaxation between different spin sublevels.

A spectral hole at $\nu_{\mathrm{pump}} = 26.8\,\mathrm{MHz}$ and two related satellites are observable. The origin of the satellites can be explained with the energy scheme presented in fig. 8.4. It shows the spin sublevels of a V_{Si} defect ensemble with variations of the zero-field-splitting $2D$. The variations of D are described by a distribution function $f(D)$.
Now it is assumed that the pump RF field saturates the spin transition from -1/2 to -3/2 with the particular value of the ZFS $2D^* = h\nu_{\mathrm{pump}} + \gamma B_z$, as depicted by the right solid arrow in fig. 8.4. Because of the spin relaxation, this also effects the transition from +1/2 to +3/2 (right dashed arrow) of the V_{Si} defects with the same ZFS, resulting in a satellite at $\nu_{\mathrm{sat2}} = \nu_{\mathrm{pump}} + 2\gamma B_z$. The other satellite occurs if the inhomogeneous broadening due to ZFS fluctuations is larger than the Zeeman splitting and ν_{pump} also saturates the transition from +1/2 to +3/2 in V_{Si} defects with different ZFS. Correspondingly, this effects the transition from -1/2 to -3/2 in these centers, resulting in another satellite at $\nu_{\mathrm{sat1}} = \nu_{\mathrm{pump}} - 2\gamma B_z$.

The satellite positions shift with the strength of B_z. In case of inhomogeneous broadening due to nuclear fields, the positions are independent from B_z, as previously observed for the N_V centres in diamond [110]. Thus, it can be concluded that magnetic fluctuations are not the main source of inhomogeneous broadening in sample H1, but that it is rather caused by ZFS fluctuations.
The above explanation of the satellite peaks is a simplified one. In the following a general theory of the satellite peak origin and positions in an inhomogeneously broadened V_{Si} spin ensemble is developed. The effective spin Hamiltonian of the V_{Si} defect in a simple axial model reads

$$\hat{H} = D\left(S_x^2 - \frac{5}{4}\right) + \gamma \mathbf{SB} \tag{8.1}$$

with the Spin operator **S** and the magnetic field **B**. In the small magnetic field $\gamma B_z << D$ considered here the energies of the spin eigenstates are given by

$$\begin{aligned} E_{"\pm 3/2"} &= D \pm \frac{3}{2}\gamma B_z \\ E_{"\pm 1/2"} &= -D \pm \frac{1}{2}\gamma\sqrt{B_z^2 + 4B_p^2} \end{aligned} \tag{8.2}$$

where B_z and B_p are the components of the magnetic field parallel and perpendicular to the c-axis respectively. For nonzero B_p, the states labeled "±3/2" ("±1/2") are in fact mixtures of the +3/2 and -3/2 (+1/2 and -1/2) spin states. Due to this mixing and also due to the low trigonal pyramidal local symmetry of the center [40] all four spin transitions between the states "±1/2" and "±3/2" are allowed. When the pump saturates one of these transitions, spin relaxation leads to the intensity change of the other transitions leading in turn to the appearance of satellite spectral holes. Their positions read

$$h\nu_{s,s'} = h\nu_{\text{pump}} + s\frac{3}{2}\gamma B_z + s'\frac{1}{2}\gamma\sqrt{B_z^2 + 4B_p^2} \tag{8.3}$$

where $s' = 0, \pm 1$ enumerates the holes. This equation yields the positions of the main spectral hole ($s = s' = 0$) and 8 satellites. The intensity of the satellites is determined by the details of the spin relaxation. In the spherical approximation, spin relaxation can be described by the relaxation times of spin dipole (T_p), quadrupole(T_d), and octupole (T_f) [111]. In the simplest case when $T_p = T_d = T_f$ only 4 out of 8 satellites that correspond to either $s = 0$ or $s' = 0$ are manifested.

8.2. Coherent control of an isolated spin packet

In this section coherent control of an isolated, spectrally selected spin packet is presented. First, a moderate magnetic field was applied to the V_{Si} defects in the isotopically purified 6H-^{28}SiC sample H1, so that the Zeeman splitting is larger than inhomogeneous broadening. The black curve in the lower part of fig. 8.5 shows the corresponding ODMR spectrum.

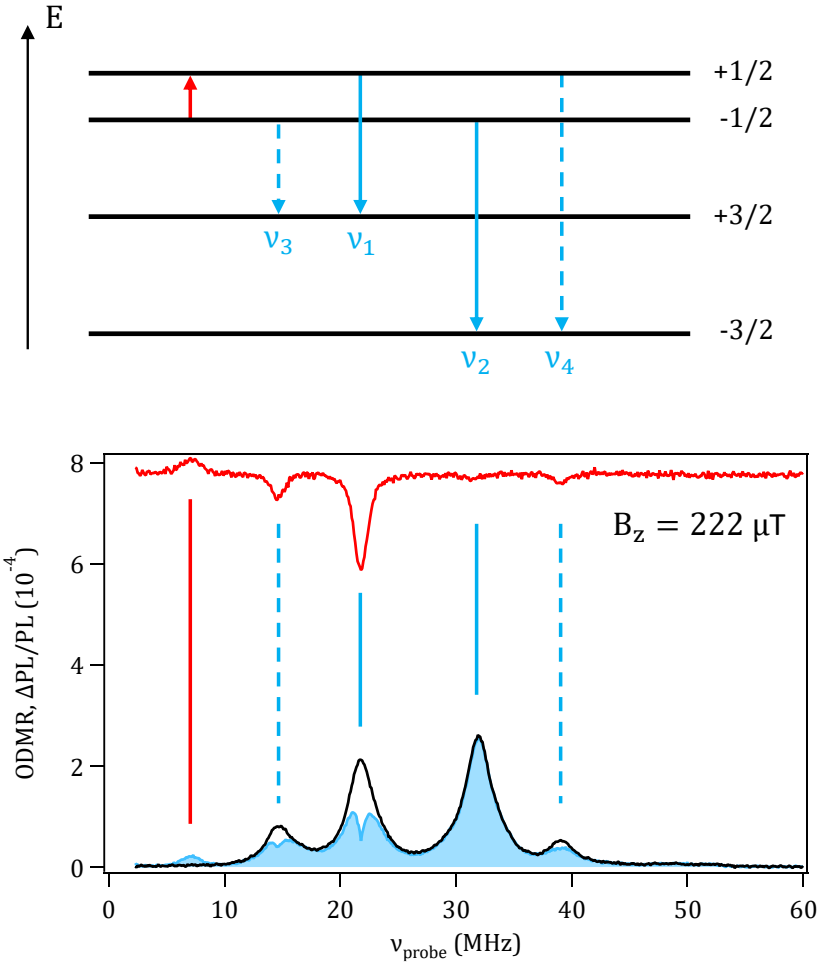

Figure 8.5.: SHB on the V3 V_{Si} defect in a small magnetic field. **top:** RF-induced transitions between different spin sublevels after optical pumping into the $\pm 3/2$ states. The solid and dashed arrows correspond to the transitions with large and small matrix elements respectively [40]. **bottom:** ODMR spectra in a magnetic field of $B = 222\,\mu$T with and without SHB at $\nu_{pump} = 21.8$ MHz. The upper curve is obtained under pump modulation.

It shows four ODMR lines, corresponding to the transitions $\nu_1 - \nu_4$ (See upper part of fig. 8.5). The inner transitions ν_1 and ν_2 are stronger than the outer transitions ν_3 and

ν_4 in accord with earlier studies [40]. A precise analysis of the line-positions [8] gives a magnetic field of $B = 222\,\mu$T with an angle of 19° between B and the c-axis.
In the following a pump RF field with $\nu_{\text{pump}} = 21.8\,$MHz is applied to burn a spectrally narrow hole into the ODMR spectrum (blue curve in fig. 8.5). As expected, the SHB satellites appear at the ν_2, ν_3 and ν_4 transitions. They can be observed even more clearly in an ODMR spectrum recorded with ν_{pump} modulated (Red curve in fig. 8.5). The spectral positions shift linearly with ν_{pump}, keeping the frequency difference the same. This is particularly pronounced in the 4H-^{28}SiC sample H2 with much larger inhomogeneous broadening, as is presented in fig. 8.6.

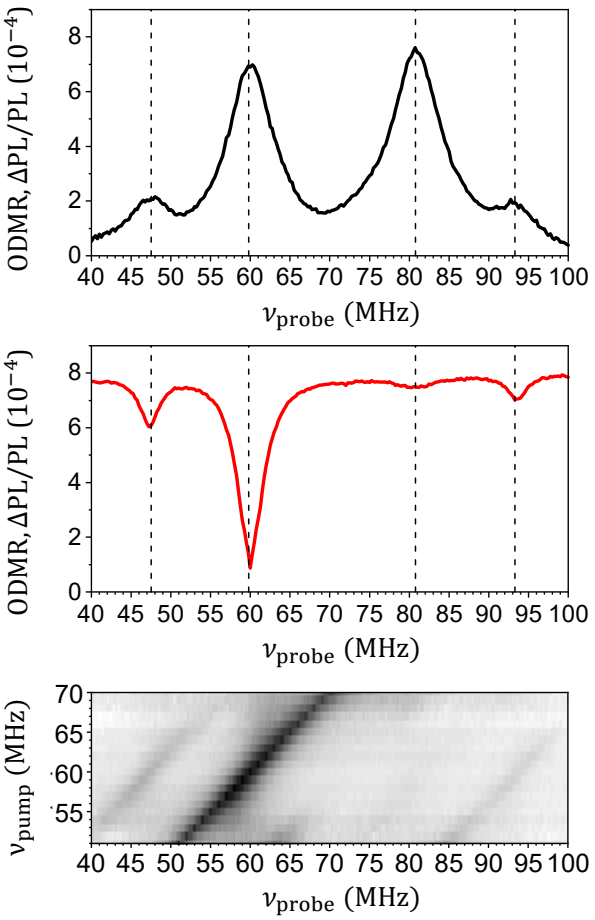

Figure 8.6.: SHB satellites in 4H-SiC. **top:** ODMR spectrum of 4H-^{28}SiC in a magnetic field $B_z = 360\,\mu$T. **middle:** Pump-induced changes in the ODMR spectrum with $\nu_{\text{pump}} = 60\,$MHz modulated. **bottom:** Pump-probe frequency scans showing relative shifts of the SHB satellites.

It can be concluded that by varying ν_{pump} within the ν_1 ODMR line different spin packets are selected.
Remarkably, the signal at ν_5 in fig. 8.5 has the opposite sign and is to 100 % conditional upon SHB at ν_1. This property is used to implement the spectrally selective coherent control of homogeneous spin packets.
Fig. 8.7 shows the two-RF pulse sequence applied to induce Rabi oscillations in a selected spin packet. The laser pulse initializes the spin sytem into the $\pm 3/2$ spin sublevel. Next, a π-pulse at $\nu_{\mathrm{pump}} = \nu_1$ is applied to select a spectrally narrow spin packet.

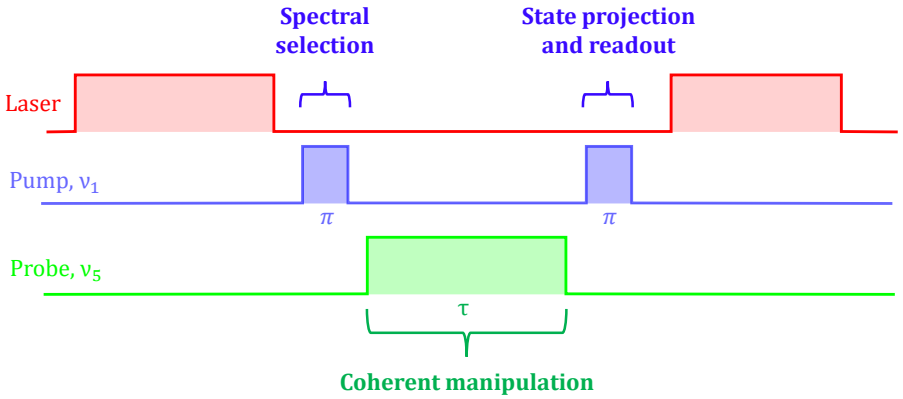

Figure 8.7.: Pulse sequence applied to select a spin packet and drive it to perform Rabi oscillations.

The $+1/2$ spin sublevel of the V_{Si} defects in this packet (i.e. the V_{Si} with $\nu_{\mathrm{pump}} = \nu_1$) is depopulated by the π-pulse at $\nu_{\mathrm{pump}} = \nu_1$. This process creates a population difference between $-1/2$ and $+1/2$ in the V_{Si} defects of the selected packet, which can be resonantly driven by applying a second RF field at ν_5. Before read-out via PL, the polarization has to be projected onto the S_z axis corresponding to the ν_1 transition by a second π-pulse at ν_1.
First, the length of the π-pulse at ν_{pump} needs to be calibrated. For this purpose, rabi oscillations are recorded at the ν_1 resonance with low driving power $W = 11\,\mathrm{dBm}$. They are presented in fig. 8.8.

In such kind of experiments a longer π-pulse results in a spectrally narrower selected spin packet [112]. The corresponding duration of the π-pulse is $1.2\,\mu\mathrm{s}$, providing sub-MHz spectral selectivity.
The spin polarization of the V_{Si} defects in the selected packet is successively RF-driven between $-1/2$ and $+1/2$. Fig. 8.9 shows the Rabi oscillations of the spin packet, coherently driven at the ν_5 transition with the pulse sequence presented in fig. 8.7.

The high driving power $W_5 = 33\,\mathrm{dBm}$ yields fast Rabi oscillations with a $\pi/2$ pulse length of 80 ns, corresponding to a bandwidth of approximately 10 MHz. This band-

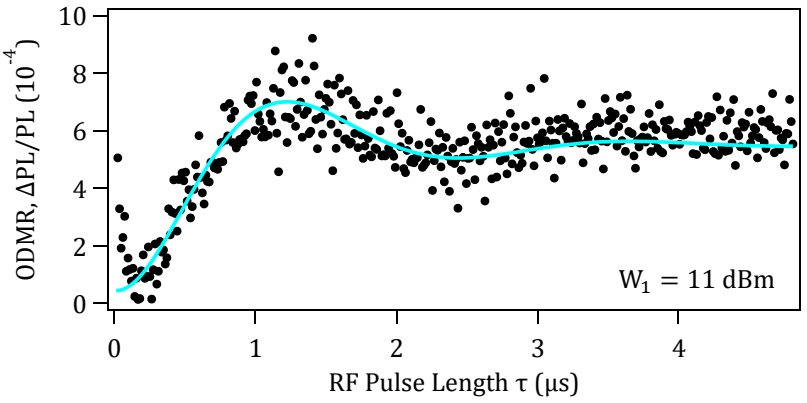

Figure 8.8.: Rabi oscillations at the ν_1 resonance driven by the RF power $W_1 = 11\,\mathrm{dBm}$ with the corresponding π-pulse duration of $1.2\,\mu\mathrm{s}$.

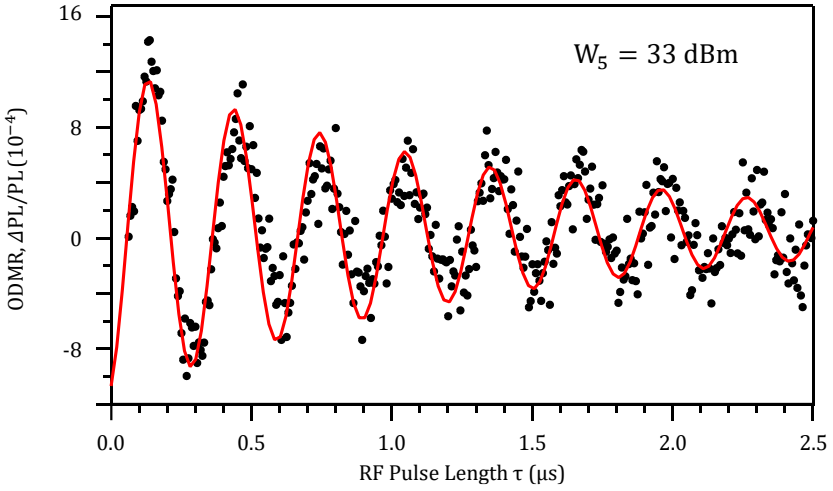

Figure 8.9.: Rabi oscillations of a selected, spectrally narrow spin packet at the ν_5 resonance driven by the RF power $W_5 = 33\,\mathrm{dBm}$

width is wide enough to encompass the ν_5 linewidth while keeping other ODMR resonances nearly unaffected.

8.3. Ramsey interferometry

In order to demonstrate the advantages of spectrally selected spin packets for quantum sensing two-frequency Ramsey experiments using the protocol presented in fig. 8.10 were performed.

The Bloch sphere in fig. 8.10 represents the spin polarization of the selected spin packet after the first ν_1-π-pulse. The successive $\pi/2$-pulse flips the polarization into

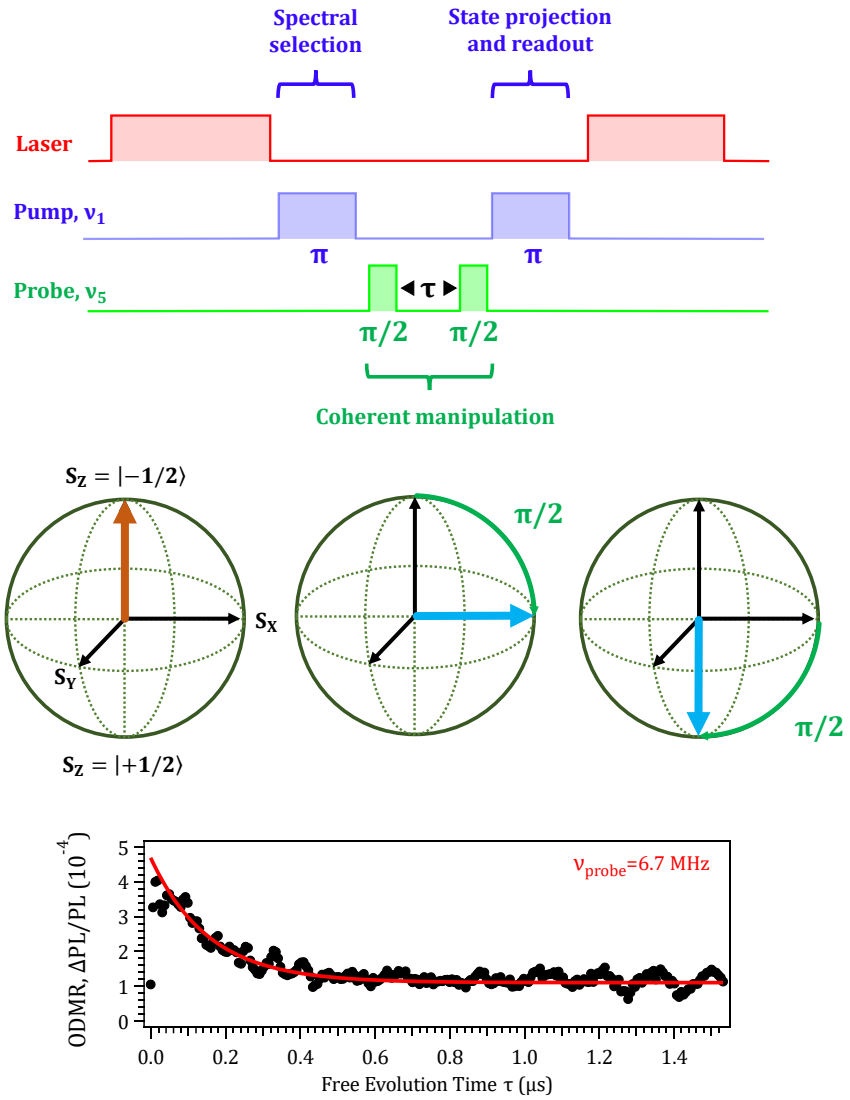

Figure 8.10.: Ramsey interferometry of spectrally selected spin packets. **top:** Pulse pattern for the spectral selection, coherent manipulation and state projection followed by the read out of spin packets. **middle:** Impact of the pulses on the spin polarization of the selected spin packet. The Bloch spheres show the polarization between the two π-pulses at ν_{pump}. **bottom:** Ramsey measurement of the spin packet selected by $\nu_{\mathrm{pump}} = 21.8\,\mathrm{MHz}$ in a magnetic field of $222\,\mu\mathrm{T}$. The probe frequency $\nu_{\mathrm{probe}} = 6.7\,\mathrm{MHz}$ is set to the ν_5 resonance. The solid line represents the fit to an exponential decay with $T_2^* = 168 \pm 7\,\mathrm{ns}$.

the S_x-S_y- plane. If the probe frequency $\nu_{\mathrm{probe}} = 6.7\,\mathrm{MHz}$ is nearly equal to the maximum of the ν_5 resonance, the signal represents free induction decay. The corresponding time-resolved spin polarization is presented in fig. 8.10. The absence of oscillations indicates that other resonances are not driven.

If the probe frequency $\nu_{\mathrm{probe}} = 11.7\,\mathrm{MHz}$ is detuned from the ν_5 resonance, a time de-

pendent phase δ in the S_x-S_y-plane between the applied RF- frequency ν_{probe} and the oscillating polarization is present. This is illustrated by the red curve in fig. 8.11.

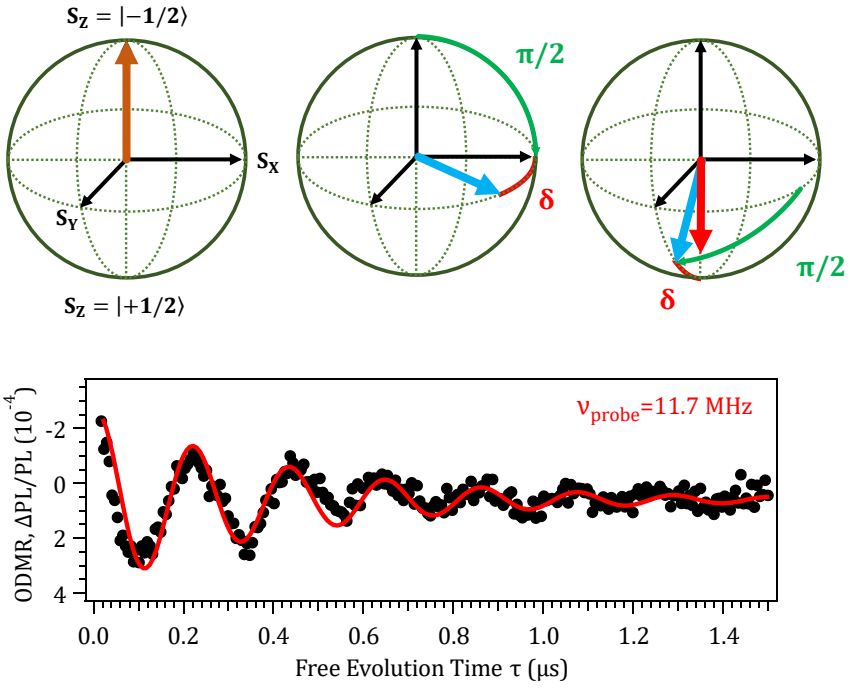

Figure 8.11.: Ramsey interferometry of spectrally selected spin packets with detuned ν_{probe}. **top:** Impact of the pulses on the spin polarization of the selected spin packet. The Bloch spheres show the polarization between the two π-pulses at ν_{pump}. **bottom:** Ramsey measurement of the spin packet selected by $\nu_{pump} = 21.8\,\text{MHz}$ in a magnetic field of $222\,\mu\text{T}$. The probe frequency $\nu_{probe} = 11.7\,\text{MHz}$ is detuned from the ν_5 resonance. The solid line represents the fit to an exponential decaying sinusoid with $T_2^* = 357 \pm 24\,\text{ns}$.

After a free evolution time τ, the second $\pi/2$-pulse is applied. The projection of the polarization onto the S_z-axis (represented by the red arrow) depends on the phase δ. Hence, the decaying spin polarization shows oscillations. This is presented in fig. 8.11 for $\nu_{probe} = 11.7\,\text{MHz}$. A fit of these dynamics to $\cos(\pi f_R \tau)\exp(-\tau/T_2^*)$ gives the coherence time of the spin packet $T_2^* = 357 \pm 24\,\text{ns}$.
The oscillations are observable only with a spectrally selected spin packet. Without selection inhomogeneous broadening forbids the oscillations. In the standard Ramsey measurements using single RF frequency performed in this work no pronounced fringes were observed, as shown in fig. 8.12.

The rotation frequency ν_0 of the polarization of the spin packet in the S_x-S_y-plane depends on the external magnetic field and hence accumulates the phase [113]:

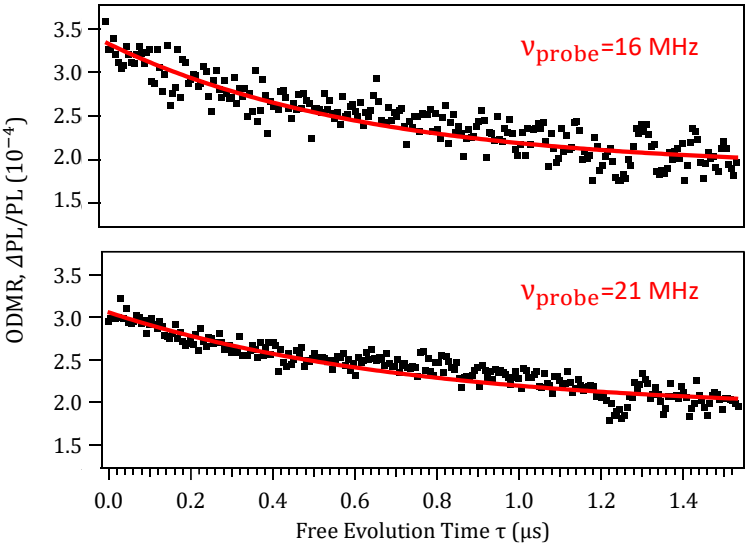

Figure 8.12.: Standard Ramsey measurements in isotopically purified 6H-^{28}SiC sample H1. **top:** Ramsey measurement at the ν_1 resonance. **bottom:** Ramsey measurement with the RF frequency detuned from the ν_1 resonance.

$$\delta = (\nu_5 - \nu_0)\, t = (\nu_5 - \frac{\gamma B_z}{\hbar})\, t. \tag{8.4}$$

This enables the derivation of the magnetic field B_z from the oscillations in the Ramsey fringes. Since $\nu_{\text{probe}} = \nu_5$ is very precisely generated by the RF source, the accuracy of the magnetic field measurement solely relies on the measurement of the Ramsey fringes. The solid circles in fig. 8.13 represent the fast Fourier transform (FFT) of the experimental data from fig. 8.11.

The fitting of these data to a Lorentz function yields the frequency of the Ramsey fringes $f_R = 4.51 \pm 0.03\,\text{MHz}$. Following eq. 8.2, the effective magnetic field can be measured with high accuracy as [108]

$$B_{\text{eff}} = \frac{\nu_{\text{propbe}} - f_R}{\gamma\sqrt{1 + 3sin^2(\theta)}}. \tag{8.5}$$

With the angle $\theta = 19°$ between the magnetic field direction and the c-axis derived from the data of fig. 8.5, $B_{\text{eff}} = 223 \pm 1\,\mu\text{T}$ was obtained from f_R.
For a verification of the high spectral resolution the magnetic field is slightly changed and measured again. To select the same spin package as in the previous case ν_{pump} is shiftet. The required shift is calculated from a bias coil current of 105 mA with corresponding $B_{\text{eff}} = 222 \pm 2\,\mu\text{T}$ for 100 mA. The FFT of the Ramsey fringes is represented

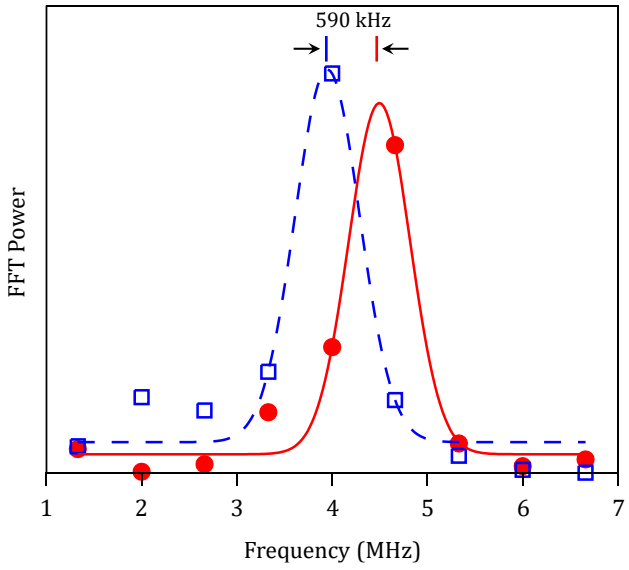

Figure 8.13.: FFT of the Ramsey fringes fitted to a Lorentz function. The solid fit corresponds to the data from fig. 8.11. The dashed fit is for the same spin packet as in fig. 8.11, but probed in a magnetic field of $242 \pm 2\,\mu$T.

by the open squares in fig. 8.13 and a Lorentz fit yields $F_R = 3.92 \pm 0.05$ MHz and a magnetic field of $B_{\text{eff}} = 242 \pm 2\,\mu$T. The two obtained values of B_{eff} correspond to measurements No. 1 and 2 in tab. 8.1.

A comparison of measurements No. 1 and No. 2 demonstrates a spectral resolution of approximately 600 kHz.

Successively, the measurement of B_{eff} was repeated with another spin packet selected (Measurement No. 3 in tab. 8.1). Within the error bars the obtained value of B_{eff} corresponds well to that of measurement No. 1. This again is a manifestation, that the inhomogeneous broadening is caused by local variations of the strain (resulting in variation of D) rather than magnetic field fluctuations. In this manner, the magnetic field strength can be measured without calibration of the zero-field splitting. This enables the implementation of absolute (i.e. immune to thermal noise and strain inhomogeneity) dc magnetometry with V_{Si} defects in SiC [114].

On the other hand, the measurements No. 1 and No. 3 cannot confirm that two different spin packets are indeed spectrally selected. To do this, similar measurements are repeated on a 4H-SiC sample with natural isotope abundance (No. 4 and No. 5 in tab. 8.1). In these measurements, B_{eff} is different for the same bias coil current. This can be explained by magnetic field fluctcations being the main mechanism of inhomogeneous broadening in this sample, resulting in a different magnetic environment for each spin packet. This results in a different B_{eff}. However, a similar measurement

No.	Polytype	I (mA)	ν_{pump} (MHz)	ν_{probe} (MHz)	f_R (MHz)	B_{eff} μT
1	6H-^{28}SiC	100	21.80	11.70	4.51 ± 0.03	223 ± 1
2		105	21.20	11.70	3.92 ± 0.05	242 ± 2
3		100	21.20	11.70	4.51 ± 0.04	223 ± 1
4	4H-SiC	150	58.60	17.00	5.33 ± 0.04	363 ± 2
5		150	58.00	17.00	4.82 ± 0.04	379 ± 2

Table 8.1.: Measurements of B_{eff} via Ramsey interferometry with two RF frequencies.

accuracy of several single μT was achieved.
Summarizing, various inhomogeneous broadening mechanisms were investigated using spectral hole burning. Further, high-resolution radio-frequency spectroscopy of V_{Si} defects in SiC at room temperature was demonstrated. In case of high-purity 6H-^{28}SiC crystals with marginal magnetic noise the proposed approach can be applied to implement absolute, sample-independent magnetometry. Due to the cross-coupling between different spin sublevels, homogeneous and highly coherent spin packets were selectively addressed and manipulated. These findings open new possibilities to significantly improve the sensitivity of quantum sensors based on strongly broadened spin ensembles.

9. Summary

In this work, the optical and quantum properties of negatively charged silicon vacancy defects (V_{Si}) in silicon carbide created with particle irradiation were examined by means of confocal pulsed optically detected magnetic resonance (pODMR) and confocal photoluminescence (PL) microscopy. The results can be used as a guideline for the creation of V_{Si} defects for quantum sensing and other quantum applications, be it the creation of an ensemble with long spin coherence or a small number of highly coherent single V_{Si} included into an electronic or photonic structure.

In the first part of this thesis the optical properties of V_{Si} defects, created by neutron, electron or proton irradiation were investigated. The analysis included a wide range of irradiation fluences and corresponding emitter densities N_V. The emitter density was determined by measuring the PL emission, calibrated with the PL emssion of a sample with known N_V. It became apparent that neutrons create considerably more crystal damage and hence a higher density of emitters than electrons for a given fluence. In both cases the maximum was $N_{V,\max} \approx 10^{16}\text{cm}^{-3}$. In neutron irradiated samples this was achieved at a fluence of $\Phi_n = 6.7 \times 10^{17}\text{cm}^{-2}$, in the case of electron irradiated samples at $\Phi_e = 4 \times 10^{18}\text{cm}^{-2}$. In the neutron irradiated samples the PL decreased in samples with a fluence higher than $\Phi_n = 6.7 \times 10^{17}\text{cm}^{-2}$ due to PL quenching caused by non V_{Si} crystal defects. The resulting underestimation of the density of V_{Si} in samples irradiated with high neutron fluences was revealed by classical EPR. Further, targeted creation of V_{Si} via proton beam writing was investigated. Control of the V_{Si} creation in all three dimensions was achieved by moving a proton beam and tuning the proton energy. By reducing the fluence at the irradiation sites, the number of V_{Si} was scaled from dense ensemble down to isolated defects.

Subsequently, the spin lattice relaxation time T_1 and coherence time T_2 were measured as a function of N_V with pODMR. The T_1 time showed to be robust against crystal damage and was constant at 300 μs up to a limit of $N_V = 10^{16}\text{cm}^{-3}$. T_2 showed strong dependence on N_V and was constant only up to $N_V = 7 \times 10^{14}\,\text{cm}^{-3}$, while decreasing with a further increase of N_V. A general approach that considers the quality of the wafer was established to describe T_2 as a function of N_V in neutron and electron irradiated samples. This approach enables V_{Si} ensemble creation with predictable spin coherence.

The T_2 time in neutron irradiated samples was considerably shorter than in electron irradiated samples. This is due to the fact that neutrons create more non V_{Si} defects, resulting in more spin-spin interactions and thus in a reduced spin coherence of the V_{Si} defects. The longest times were achieved in electron irradiated samples with low irradiation fluence and an emitter density $N_V < 7 \times 10^{14}\,\mathrm{cm}^{-3}$ with $T_2^{\mathrm{pristine}} \approx 48\,\mu\mathrm{s}$ and the proton irradiated sample with $T_2 = 42 \pm 20\,\mu\mathrm{s}$, making them most suitable for applications requiring an ensemble with long spin coherence. The ability to write V_{Si} on target and with good coherence properties in a SiC crystal makes proton beam writing an all-purpose weapon for embedding them into existing structures of any kind.
Successively, several samples irradiated with neutrons or electrons were annealed in order to heal non V_{Si} defects and improve the optical and spin properties of the V_{Si} defects. In the electron irradiated sample no change of the PL emission, T_1 or T_2 was apparent. In contrast to that significant improvements were achieved in the neutron irradiated samples. Due to the reduction of the percentage of non V_{Si} defects the PL emission increased and T_1 as well as T_2 could be significantly prolonged. The effects were stronger in the samples with higher N_V due to a higher number of non V_{Si} defects prior to annealing. The results demonstrate the potential of sample annealing to partly restore the coherence of V_{Si} defects in an ensemble with high and, also in large bulk crystals, in depth homogeneous N_V created with neutron irradiation.
In the fourth and final part of this thesis, various inhomogeneous broadening mechanisms were investigated with two-frequency ODMR and corresponding spectral hole-burning. Further, two-frequency Ramsey interferometry was used to increase measurement accuracy for quantum sensing. In case of high-purity ^{28}Si-enriched SiC crystals with marginal magnetic noise the proposed approach can be applied to implement absolute, sample-independent magnetometry. A spectral resolution of about 600 kHz at room temperature was achieved, which is one order of magnitude improvement compared to the inhomogeneous linewidth, boosting the potential precision of quantum sensors based on the V_{Si} platform. These findings open new possibilities for a significant improvement of the sensitivity of quantum sensors based on strongly broadened spin ensembles.
The results in this thesis provide an engineering guide for V_{Si} defects in SiC created by electron, neutron or proton irradiation for quantum sensing and other applications. The demonstrated control of the V_{Si} density, their spin coherence and targeted implantation provides the possibility of sample fabrication containing custom made V_{Si} ensembles, structures or single V_{Si}. Two-frequency Ramsey interferometry was performed to demonstrate absolute dc magnetometry, i.e. insensitive to the fluctuations of the sample-specific parameters. The results obtained can give V_{Si} defects in silicon

carbide a huge boost and justify its position among the top material systems in the future of quantum applications.

Zusammenfassung

In dieser Arbeit wurden die optischen und Kohärenzeigenschaften von Silizium Fehlstellen (V_{Si}- Defekten) in Siliziumkarbid, welche durch Bestrahlung mit Neutronen, Elektronen oder Protonen erzeugt wurden, mit Hilfe von konfokaler Mikroskopie und gepulster optisch detektierter Magnetresonanz (pODMR) untersucht. Die Ergebnisse können als Anleitung zur Erzeugung von V_{Si}-Defekten für Anwendungen im Bereich der Quantensensorik und verwandter Anwendungsgebiete dienen, sei es zur Erzeugung eines Ensembles mit langer Kohärenz oder einzelner weniger isolierter V_{Si}-Defekte in einer bestehenden elektrischen oder photonischen Struktur.

Im ersten Teil dieser Arbeit wurden die optischen Eigenschaften von V_{Si}-Defekten, erzeugt durch Bestrahlung mit Neutronen, Elektronen oder Protonen, untersucht. Die Ergebnisse umfassen einen weiten Bereich der Fluenz, mit der die Proben bestrahlt wurden und der zugehörigen Emitterdichte N_V. Die Emitterdichte wurde mit Hilfe der PL-Emission einer Probe bestimmt, wobei eine Refernzprobe mit bekannter N_V zur Kalibrierung verwendet wurde. Es zeigte sich, dass ein SiC Kristall bei gleicher Fluenz durch Neutronenbestrahlung deutlich mehr beschädigt wird als durch Elektronenbestrahlung. Daraus resultiert eine höhere Anzahl erzeugter Emitter im Falle der Neutronenbestrahlung. Sowohl bei Neutronen-, als auch bei Elektronenbestrahlung lag das erreichte Maximum bei $N_{V,\max} \approx 10^{16}\mathrm{cm}^{-3}$. In den neutronenbestrahlten Proben wurde dieses Maximum bei einer Fluenz von $\Phi_n = 6.7 \times 10^{17}\mathrm{cm}^{-2}$ erreicht, für Elektronenbestrahlung lag der Wert bei $\Phi_e = 4 \times 10^{18}\mathrm{cm}^{-2}$. Die PL sank in Proben, welche mit einer Fluenz über $\Phi_n = 6.7 \times 10^{17}\mathrm{cm}^{-2}$ bestrahlt wurden auf Grund von Quenching. Durch die Bestrahlung entstanden nicht nur V_{Si}-Defekte, sondern auch Defekte anderer Art. Dies führte zu einer Unterschätzung der Defektdichte in stark neutronenbestrahlten Proben, was durch die Untersuchung der Proben mit klassischer Elektronenspinresonanz bestätigt wurde. Desweiteren wurde die gezielte Erzeugung von V_{Si}-Defekten mit Hilfe eines Protonenstrahles untersucht. Die Kontrolle der Erzeugung in allen drei Raumdimensionen wurde durch die Bewegung des Protonenstrahles in lateraler Richtung und durch Variation der Energie der Protonen erreicht. Durch eine Reduzierung der Fluenz konnten so isolierte, einzelne V_{Si}-Defekte erzeugt werden.

In zweiten Teil der Arbeit wurden die Spin-Gitter-Relaxationszeit T_1 und die Spinkohärenzzeit T_2 in Abhängigkeit von N_V durch pODMR bestimmt. Die T_1-Zeit lag bis zu einer Grenze von $N_V = 10^{16}\mathrm{cm}^{-3}$ konstant bei ca. $300\,\mu$s. Im Gegensatz dazu hing T_2 stark von N_V ab. Sie war bis $N_V = 7 \times 10^{14}\,\mathrm{cm}^{-3}$ konstant und fiel dann mit steigender N_V kontinuierlich ab. Es wurde ein mathematischer Zusammenhang hergeleitet, welcher die Abhängigkeit von T_2 von N_V in neutronen- und elektronenbestrahltem SiC

theoretisch beschreibt. Dies ermöglicht die Erzeugung von V_{Si} Ensembles mit vorhersagbaren Kohärenzeigenschaften.
Die T_2 Zeit von V_{Si}-Defekten, welche durch Neutronenbestrahlung erzeugt wurden, war deutlich geringer als im Falle von Elektronenbestrahlung. Dies ist der Tatsache geschuldet, dass Neutronenbestrahlung einen geringeren Anteil von V_{Si}-Defekten erzeugt und einen höheren Anteil anderer Defekttypen. Daraus folgen mehr Spin-Spin Wechselwirkungen zwischen Kristalldefekten im Vergleich zu V_{Si}-Defekten in elektronenbestrahlten Proben, was zu einer verringerten Spinkohärenz führt. Die längsten T_2 Zeiten ergaben sich in elektronenbestrahlten Proben mit $N_V < 7 \times 10^{14}\,\mathrm{cm}^{-3}$ und $T_2^{\mathrm{pristine}} \approx 48\,\mu\mathrm{s}$. Auch in der protonenbestrahlten Probe war T_2 mit $T_2 = 42 \pm 20\,\mu\mathrm{s}$ vergleichsweise lang. Dies bietet die Möglichkeit der gezielten Erzeugung von Defekten mit guten Kohärenzeigenschaften.
Im dritten Teil dieser Arbeit wurden einige neutronen- und elektronenbestrahlte Proben getempert, um störende Kristalldefekte auszuheilen. In der elektronenbestrahlten Probe konnte keine Änderung der optischen oder Kohärenzeigenschaften nachgewiesen werden. Im Gegensatz dazu konnte in den stark neutronenbestrahlten Proben eine deutliche Verbesserung der optischen Eigenschaften und eine Steigerung der T_2-Zeit um den Faktor drei erzielt werden. Dies zeigt das enorme Potential von tempern im Bezug auf die Eigenschaften von V_{Si}-Defekten.
Im vierten und letzten Teil dieser Arbeit wurden die Ursachen der inhomogenen Linienverbreiterung mit Hilfe von ODMR mit zwei Mikrowellenfrequenzen untersucht. Desweiteren wurde Ramsey- Interferometrie eingesetzt, um die Sensitivität von V_{Si}-Defekten für Quantensensorik zu verbessern. Im Falle eines hochreinen, isotopbereinigten ^{28}SiC-Kristalls konnte absolute DC-Magnetometrie realisiert werden, welche unabhängig von Fluktuationen des Zero-Field-Splittings der V_{Si}-Defekte ist. Zudem wurde eine Sensitivität von 600 kHz erzielt, was im Falle einer Magnetfeldmessung wenigen μT entspricht und gegenüber der inhomogen verbreiterten Linie eine Verbesserung um eine Größenordnung darstellt. Die Ergebnisse dieses Kapitels demonstrieren eine Möglichkeit, die Sensitivität von Quantensensoren, welche auf Spinensembles mit inhomogener Verbreiterung basieren, deutlich zu verbessern.
Die Ergebnisse in dieser Arbeit liefern ein Handbuch zur Erzeugung und Verwendung von V_{Si}-Defekten in SiC für Anwendungen im Bereich der Quantensensorik, aber auch verwandter Anwendungsgebiete. Es wurde die Kontrolle der Emitterdichte N_V, der Spinkohärenz, als auch der räumlich gezielten Erzeugung demonstriert. Diese Kontrolle ermöglicht die Herstellung maßgeschneiderter V_{Si}- Ensembles für spezifische Anwendungen. Zusätzlich wurde nachgewiesen, dass absolute DC-Magnetometrie mit Hilfe von Ramsey-Interferometrie möglich ist, welche unabhängig von Fluktuationen der

Materialparameter ist. Die Ergebnisse stärken die Position der V_{Si}-Defekte als Materialplattform für Quantensensorik und verdeutlichen ihre Wichtigkeit für die Zukunft der Quantenapplikationen.

Bibliography

[1] M. M. Waldrop. The chips are down for moore's law. *Nature News*, **530**, 7589, 144 (2016).

[2] R. P. Feynman. Simulating physics with computers. *Int. J. Theor. Phys*, **21**, 6/7 (1982).

[3] L. Childress, M. G. Dutt, J. Taylor, A. Zibrov, F. Jelezko, J. Wrachtrup, P. Hemmer and M. Lukin. Coherent dynamics of coupled electron and nuclear spin qubits in diamond. *Science*, **314**, 5797, 281 (2006).

[4] P. W. Shor. Algorithms for quantum computation: discrete logarithms and factoring. In *Proceedings 35th annual symposium on foundations of computer science*, 124–134. Ieee (1994).

[5] C. H. Bennett and G. Brassard. Quantum cryptography: Public key distribution and coin tossing. *arXiv preprint arXiv:2003.06557* (2020).

[6] J. W. Bos, J. A. Halderman, N. Heninger, J. Moore, M. Naehrig and E. Wustrow. Elliptic curve cryptography in practice. In *International Conference on Financial Cryptography and Data Security*, 157–175. Springer (2014).

[7] C. L. Degen, F. Reinhard and P. Cappellaro. Quantum sensing. *Reviews of modern physics*, **89**, 3, 035002 (2017).

[8] D. Simin, F. Fuchs, H. Kraus, A. Sperlich, P. Baranov, G. Astakhov and V. Dyakonov. High-precision angle-resolved magnetometry with uniaxial quantum centers in silicon carbide. *Physical Review Applied*, **4**, 1, 014009 (2015).

[9] T. Taminiau, J. Wagenaar, T. Van der Sar, F. Jelezko, V. V. Dobrovitski and R. Hanson. Detection and control of individual nuclear spins using a weakly coupled electron spin. *Physical review letters*, **109**, 13, 137602 (2012).

[10] D. J. Christle, P. V. Klimov, F. Charles, K. Szász, V. Ivády, V. Jokubavicius, J. U. Hassan, M. Syväjärvi, W. F. Koehl, T. Ohshima et al. Isolated spin qubits in sic with

a high-fidelity infrared spin-to-photon interface. *Physical Review X*, **7**, 2, 021046 (2017).

[11] E. Zhukov, D. Yakovlev, M. Glazov, L. Fokina, G. Karczewski, T. Wojtowicz, J. Kossut and M. Bayer. Optical control of electron spin coherence in cdte/(cd, mg) te quantum wells. *Physical Review B*, **81**, 23, 235320 (2010).

[12] J. J. Pla, K. Y. Tan, J. P. Dehollain, W. H. Lim, J. J. Morton, F. A. Zwanenburg, D. N. Jamieson, A. S. Dzurak and A. Morello. High-fidelity readout and control of a nuclear spin qubit in silicon. *Nature*, **496**, 7445, 334 (2013).

[13] G. Davies and M. Hamer. Optical studies of the 1.945 ev vibronic band in diamond. *Proceedings of the Royal Society of London. A. Mathematical and Physical Sciences*, **348**, 1653, 285 (1976).

[14] F. Jelezko and J. Wrachtrup. Single defect centres in diamond: A review. *physica status solidi (a)*, **203**, 13, 3207 (2006).

[15] A. Gruber, A. Dräbenstedt, C. Tietz, L. Fleury, J. Wrachtrup and C. Von Borczyskowski. Scanning confocal optical microscopy and magnetic resonance on single defect centers. *Science*, **276**, 5321, 2012 (1997).

[16] G. Balasubramanian, P. Neumann, D. Twitchen, M. Markham, R. Kolesov, N. Mizuochi, J. Isoya, J. Achard, J. Beck, J. Tissler et al. Ultralong spin coherence time in isotopically engineered diamond. *Nature materials*, **8**, 5, 383 (2009).

[17] F. Jelezko, T. Gaebel, I. Popa, A. Gruber and J. Wrachtrup. Observation of coherent oscillations in a single electron spin. *Physical review letters*, **92**, 7, 076401 (2004).

[18] J. R. Maze, P. L. Stanwix, J. S. Hodges, S. Hong, J. M. Taylor, P. Cappellaro, L. Jiang, M. G. Dutt, E. Togan, A. Zibrov et al. Nanoscale magnetic sensing with an individual electronic spin in diamond. *Nature*, **455**, 7213, 644 (2008).

[19] J.-I. Chao, E. Perevedentseva, P.-H. Chung, K.-K. Liu, C.-Y. Cheng, C.-C. Chang and C.-L. Cheng. Nanometer-sized diamond particle as a probe for biolabeling. *Biophysical journal*, **93**, 6, 2199 (2007).

[20] T. M. Babinec, B. J. Hausmann, M. Khan, Y. Zhang, J. R. Maze, P. R. Hemmer and M. Lončar. A diamond nanowire single-photon source. *Nature nanotechnology*, **5**, 3, 195 (2010).

[21] S. Carter, Ö. Soykal, P. Dev, S. E. Economou and E. Glaser. Spin coherence and echo modulation of the silicon vacancy in 4h-sic at room temperature. *Physical Review B*, **92**, 16, 161202 (2015).

[22] D. Simin, H. Kraus, A. Sperlich, T. Ohshima, G. Astakhov and V. Dyakonov. Locking of electron spin coherence above 20 ms in natural silicon carbide. *Physical Review B*, **95**, 16, 161201 (2017).

[23] M. Niethammer, M. Widmann, T. Rendler, N. Morioka, Y.-C. Chen, R. Stöhr, J. U. Hassan, S. Onoda, T. Ohshima, S.-Y. Lee et al. Coherent electrical readout of defect spins in silicon carbide by photo-ionization at ambient conditions. *Nature communications*, **10**, 1, 1 (2019).

[24] P. G. Baranov, A. P. Bundakova, A. A. Soltamova, S. B. Orlinskii, I. V. Borovykh, R. Zondervan, R. Verberk and J. Schmidt. Silicon vacancy in sic as a promising quantum system for single-defect and single-photon spectroscopy. *Physical Review B*, **83**, 12, 125203 (2011).

[25] S. Castelletto, B. Johnson, V. Ivády, N. Stavrias, T. Umeda, A. Gali and T. Ohshima. A silicon carbide room-temperature single-photon source. *Nature materials*, **13**, 2, 151 (2014).

[26] M. Widmann, S.-Y. Lee, T. Rendler, N. T. Son, H. Fedder, S. Paik, L.-P. Yang, N. Zhao, S. Yang, I. Booker et al. Coherent control of single spins in silicon carbide at room temperature. *Nature materials*, **14**, 2, 164 (2015).

[27] G. Kucsko, P. C. Maurer, N. Y. Yao, M. Kubo, H. J. Noh, P. K. Lo, H. Park and M. D. Lukin. Nanometre-scale thermometry in a living cell. *Nature*, **500**, 7460, 54 (2013).

[28] H. Kraus, V. Soltamov, F. Fuchs, D. Simin, A. Sperlich, P. Baranov, G. Astakhov and V. Dyakonov. Magnetic field and temperature sensing with atomic-scale spin defects in silicon carbide. *Scientific reports*, **4**, 5303 (2014).

[29] H. Kraus, C. Raymond, N. Murphy, C. Cochrane, J. Blacksberg, P. Neudeck and D. Spry. High-sensitivity solid state magnetometry leveraging silicon carbide quantum centers. *cosp*, **42**, A0 (2018).

[30] D. L. Dunsch, editor. *Band 85: Joens Jacob Berzelius*. Biographien hervorragender Naturwissenschaftler, Techniker und Mediziner. BSB B. G. Teubner Verlagsgesellschaft (1986).

[31] E. G. Acheson. Production of artificial crystalline garbonaceous materials (1893). US Patent 492,767.

[32] H. Moissan. Nouvelles recherches sur la météorité de cañon diablo. *Comptes rendus*, **139**, 773 (1904).

[33] W. J. Choyke and G. Pensl. Siliciumkarbid — halbleiter für die neunziger jahre. *Physikalische Blätter*, **47**, 3, 212. doi: 10.1002/phbl.19910470309.

[34] P. Ivanov and V. Chelnokov. Recent developments in sic single-crystal electronics. *Semiconductor science and technology*, **7**, 7, 863 (1992).

[35] R. Weast et al. Handbook of chemistry and physics. crc press, boca raton, fl. *Handbook of chemistry and physics. 64th ed. CRC Press, Boca Raton, FL.* (1986).

[36] L. d. S. Balona and J. Loubser. Esr in irradiated silicon carbide. *Journal of Physics C: Solid State Physics*, **3**, 11, 2344 (1970).

[37] E. Burgemeister, W. Von Muench and E. Pettenpaul. Thermal conductivity and electrical properties of 6 h silicon carbide. *Journal of Applied Physics*, **50**, 9, 5790 (1979).

[38] P. Ravindran, K. Manisekar, R. Narayanasamy and P. Narayanasamy. Tribological behaviour of powder metallurgy-processed aluminium hybrid composites with the addition of graphite solid lubricant. *Ceramics International*, **39**, 2, 1169 (2013).

[39] H. Kraus, V. Soltamov, D. Riedel, S. Väth, F. Fuchs, A. Sperlich, P. Baranov, V. Dyakonov and G. Astakhov. Room-temperature quantum microwave emitters based on spin defects in silicon carbide. *Nature Physics*, **10**, 2, 157 (2014).

[40] D. Simin, V. Soltamov, A. Poshakinskiy, A. Anisimov, R. Babunts, D. Tolmachev, E. Mokhov, M. Trupke, S. Tarasenko, A. Sperlich et al. All-optical dc nanotesla magnetometry using silicon vacancy fine structure in isotopically purified silicon carbide. *Physical Review X*, **6**, 3, 031014 (2016).

[41] C. J. Cochrane, H. Kraus, P. G. Neudeck, D. Spry, R. J. Waskiewicz, J. P. Ashton and P. M. Lenahan. Magnetic field sensing with 4h sic diodes: n vs p implantation. In *Materials Science Forum*, volume 924, 988–992. Trans Tech Publ (2018).

[42] S. Tanaka, R. S. Kern and R. F. Davis. Effects of gas flow ratio on silicon carbide thin film growth mode and polytype formation during gas-source molecular beam epitaxy. *Applied physics letters*, **65**, 22, 2851 (1994).

[43] L. S. Ramsdell. Studies on silicon carbide. *American Mineralogist: Journal of Earth and Planetary Materials*, **32**, 1-2, 64 (1947).

[44] C. Eddy and D. Gaskill. Silicon carbide as a platform for power electronics. *Science*, **324**, 5933, 1398 (2009).

[45] J. Bergman, L. Storasta, F. Carlsson, S. Sridhara, B. Magnusson and E. Janze'n. Defects in 4h silicon carbide. *Physica B: Condensed Matter*, **308**, 675 (2001).

[46] A. L. Falk, P. V. Klimov, B. B. Buckley, V. Ivády, I. A. Abrikosov, G. Calusine, W. F. Koehl, Á. Gali and D. D. Awschalom. Electrically and mechanically tunable electron spins in silicon carbide color centers. *Physical review letters*, **112**, 18, 187601 (2014).

[47] Ö. Soykal and T. L. Reinecke. Quantum metrology with a single spin-3/2 defect in silicon carbide. *Physical Review B*, **95**, 8, 081405 (2017).

[48] S. Castelletto, B. C. Johnson and A. Boretti. Quantum effects in silicon carbide hold promise for novel integrated devices and sensors. *Advanced Optical Materials*, **1**, 9, 609 (2013).

[49] S.-Y. Lee, M. Niethammer and J. Wrachtrup. Vector magnetometry based on $s = 3/2$ electronic spins. *Physical Review B*, **92**, 11, 115201 (2015).

[50] M. Niethammer, M. Widmann, S.-Y. Lee, P. Stenberg, O. Kordina, T. Ohshima, N. T. Son, E. Janzén and J. Wrachtrup. Vector magnetometry using silicon vacancies in 4h-sic under ambient conditions. *Physical Review Applied*, **6**, 3, 034001 (2016).

[51] C. J. Cochrane, J. Blacksberg, M. A. Anders and P. M. Lenahan. Vectorized magnetometer for space applications using electrical readout of atomic scale defects in silicon carbide. *Scientific reports*, **6**, 37077 (2016).

[52] A. Anisimov, D. Simin, V. Soltamov, S. Lebedev, P. Baranov, G. Astakhov and V. Dyakonov. Optical thermometry based on level anticrossing in silicon carbide. *Scientific reports*, **6**, 1, 1 (2016).

[53] F. Fuchs, B. Stender, M. Trupke, D. Simin, J. Pflaum, V. Dyakonov and G. Astakhov. Engineering near-infrared single-photon emitters with optically active spins in ultrapure silicon carbide. *Nature communications*, **6**, 1, 1 (2015).

[54] D. J. Christle, A. L. Falk, P. Andrich, P. V. Klimov, J. U. Hassan, N. T. Son, E. Janzén, T. Ohshima and D. D. Awschalom. Isolated electron spins in silicon carbide with millisecond coherence times. *Nature materials*, **14**, 2, 160 (2015).

[55] M. Fischer, A. Sperlich, H. Kraus, T. Ohshima, G. Astakhov and V. Dyakonov. Highly efficient optical pumping of spin defects in silicon carbide for stimulated microwave emission. *Physical Review Applied*, **9**, 5, 054006 (2018).

[56] H. B. Banks, Ö. O. Soykal, R. L. Myers-Ward, D. K. Gaskill, T. Reinecke and S. G. Carter. Resonant optical spin initialization and readout of single silicon vacancies in 4 h-si c. *Physical Review Applied*, **11**, 2, 024013 (2019).

[57] R. Nagy, M. Niethammer, M. Widmann, Y.-C. Chen, P. Udvarhelyi, C. Bonato, J. U. Hassan, R. Karhu, I. G. Ivanov, N. T. Son et al. High-fidelity spin and optical control of single silicon-vacancy centres in silicon carbide. *Nature communications*, **10**, 1, 1 (2019).

[58] M. Veldhorst, J. Hwang, C. Yang, A. Leenstra, B. de Ronde, J. Dehollain, J. Muhonen, F. Hudson, K. M. Itoh, A. Morello et al. An addressable quantum dot qubit with fault-tolerant control-fidelity. *Nature nanotechnology*, **9**, 12, 981 (2014).

[59] A. Shnirman, G. Schön and Z. Hermon. Quantum manipulations of small josephson junctions. *Physical Review Letters*, **79**, 12, 2371 (1997).

[60] A. Myerson, D. Szwer, S. Webster, D. Allcock, M. Curtis, G. Imreh, J. Sherman, D. Stacey, A. Steane and D. Lucas. High-fidelity readout of trapped-ion qubits. *Physical Review Letters*, **100**, 20, 200502 (2008).

[61] S. Diao, G. Hong, A. L. Antaris, J. L. Blackburn, K. Cheng, Z. Cheng and H. Dai. Biological imaging without autofluorescence in the second near-infrared region. *Nano Research*, **8**, 9, 3027 (2015).

[62] M. Oxborrow, J. D. Breeze and N. M. Alford. Room-temperature solid-state maser. *Nature*, **488**, 7411, 353 (2012).

[63] E. Janzén, A. Gali, P. Carlsson, A. Gällström, B. Magnusson and N. T. Son. The silicon vacancy in sic. *Physica B: Condensed Matter*, **404**, 22, 4354 (2009).

[64] D. Riedel, F. Fuchs, H. Kraus, S. Väth, A. Sperlich, V. Dyakonov, A. Soltamova, P. Baranov, V. Ilyin and G. Astakhov. Resonant addressing and manipulation of silicon vacancy qubits in silicon carbide. *Physical review letters*, **109**, 22, 226402 (2012).

[65] M. Lax, N. R. L. (U.S.) and N. P. S. (U.S.). *Application of the Franck-Condon Principle to Complex Systems*. NRL report. Naval Research Laboratory (1952).

[66] S. Orlinski, J. Schmidt, E. Mokhov and P. Baranov. Silicon and carbon vacancies in neutron-irradiated sic: A high-field electron paramagnetic resonance study. *Physical Review B - PHYS REV B*, **67** (2003). doi: 10.1103/PhysRevB.67.125207.

[67] T. Wimbauer, B. Meyer, A. Hofstaetter, A. Scharmann and H. Overhof. Negatively charged si vacancy in 4 h sic: A comparison between theory and experiment. *Physical Review B*, **56**, 12, 7384 (1997).

[68] N. Mizuochi, S. Yamasaki, H. Takizawa, N. Morishita, T. Ohshima, H. Itoh, T. Umeda and J. Isoya. Spin multiplicity and charge state of a silicon vacancy (tv2a) in 4h-sic determined by pulsed endor. *Physical review B*, **72**, 23, 235208 (2005).

[69] Ö. O. Soykal, P. Dev and S. E. Economou. Silicon vacancy center in 4h-sic: Electronic structure and spin-photon interfaces. *Physical Review B*, **93**, 8 (2016). ISSN 2469-9969. doi: 10.1103/physrevb.93.081207.

[70] P. G. Baranov, H. J. Von Bardeleben, F. Jelezko and J. Wrachtrup. *Magnetic resonance of semiconductors and their nanostructures*. Springer (2017).

[71] S. G. Müller, M. Brady, W. Brixius, R. Glass, J. R. Jenny, R. Leonard, D. Malta, A. R. Powell, V. F. Tsvetkov, S. Allen et al. Sublimation-grown semi-insulating sic for high frequency devices. In *Materials Science Forum*, volume 433, 39–44. Trans Tech Publ (2003).

[72] S. Hagen and A. Van Kemenade. Infrared luminescence in silicon carbide. *Journal of Luminescence*, **9**, 1, 9 (1974).

[73] P. Friedrichs, T. Kimoto, L. Ley and G. Pensl. *Silicon Carbide: Volume 1: Growth, Defects, and Novel Applications*. John Wiley & Sons (2011).

[74] T. Kimoto and J. A. Cooper. *Fundamentals of silicon carbide technology: growth, characterization, devices and applications*. John Wiley & Sons (2014).

[75] J. Jenny, J. Skowronski, W. Mitchel, H. Hobgood, R. Glass, G. Augustine and R. Hopkins. Deep level transient spectroscopic and hall effect investigation of the position of the vanadium acceptor level in 4h and 6h sic. *Applied physics letters*, **68**, 14, 1963 (1996).

[76] J. R. Jenny, D. Malta, M. Calus, S. G. Müller, A. R. Powell, V. F. Tsvetkov, R. Glass, C. H. Carter Jr et al. Development of large diameter high-purity semi-insulating 4h-sic wafers for microwave devices. In *Materials Science Forum*, volume 457, 35–40. Trans Tech Publ (2004).

[77] H. L. Heinisch, L. R. Greenwood, W. J. Weber and R. E. Williford. Displacement damage in silicon carbide irradiated in fission reactors. *Journal of nuclear materials*, **327**, 2-3, 175 (2004).

[78] E. Sörman, N. Son, W. Chen, O. Kordina, C. Hallin and E. Janzén. Silicon vacancy related defect in 4h and 6h sic. *Physical Review B*, **61**, 4, 2613 (2000).

[79] H. Von Bardeleben, J. Cantin, L. Henry and M. Barthe. Vacancy defects in p-type 6 h- sic created by low-energy electron irradiation. *Physical Review B*, **62**, 16, 10841 (2000).

[80] H. Kraus, D. Simin, C. Kasper, Y. Suda, S. Kawabata, W. Kada, T. Honda, Y. Hijikata, T. Ohshima, V. Dyakonov and G. V. Astakhov. Three-dimensional proton beam writing of optically active coherent vacancy spins in silicon carbide. *Nano Letters*, **17**, 5, 2865 (2017).

[81] F. Nava, G. Bertuccio, A. Cavallini and E. Vittone. Silicon carbide and its use as a radiation detector material. *Measurement Science and Technology*, **19**, 10, 102001 (2008).

[82] E. Wendler, T. Bierschenk, F. Felgenträger, J. Sommerfeld, W. Wesch, D. Alber, G. Bukalis, L. C. Prinsloo, N. Van der Berg, E. Friedland et al. Damage formation and optical absorption in neutron irradiated sic. *Nuclear Instruments and Methods in Physics Research Section B: Beam Interactions with Materials and Atoms*, **286**, 97 (2012).

[83] H. Weber, H. Böck, E. Unfried and L. Greenwood. Neutron dosimetry and damage calculations for the triga mark-ii reactor in vienna. *Journal of Nuclear Materials*, **137**, 3, 236 (1986).

[84] https://ati.tuwien.ac.at/reactor/en/.

[85] S. N. Ahmed. *Physics and engineering of radiation detection*. Academic Press (2007).

[86] J. F. Ziegler. Srim - the stopping and range of ions in matter.

[87] C. Kurtsiefer, S. Mayer, P. Zarda and H. Weinfurter. Stable solid-state source of single photons. *Physical review letters*, **85**, 2, 290 (2000).

[88] D. Fattal and Y. Yamamoto. Single photons for quantum information processing. Ph.D. thesis, Stanford University (2005).

[89] A. Kastler. Optical methods of atomic orientation and of magnetic resonance. *JOSA*, **47**, 6, 460 (1957).

[90] C. Kasper, D. Klenkert, Z. Shang, D. Simin, A. Gottscholl, A. Sperlich, H. Kraus, C. Schneider, S. Zhou, M. Trupke et al. Influence of irradiation on defect spin coherence in silicon carbide. *Physical Review Applied*, **13**, 4, 044054 (2020).

[91] L. Snead and J. Hay. Neutron irradiation induced amorphization of silicon carbide. *Journal of nuclear materials*, **273**, 2, 213 (1999).

[92] T. Suzuki, T. Yano, T. Mori, H. Miyazaki and T. Iseki. Neutron irradiation damage of silicon carbide. *Fusion technology*, **27**, 3, 314 (1995).

[93] F. Fuchs, V. Soltamov, S. Väth, P. Baranov, E. Mokhov, G. Astakhov and V. Dyakonov. Silicon carbide light-emitting diode as a prospective room temperature source for single photons. *Scientific reports*, **3**, 1637 (2013).

[94] M. Radulaski, M. Widmann, M. Niethammer, J. L. Zhang, S.-Y. Lee, T. Rendler, K. G. Lagoudakis, N. T. Son, E. Janzen, T. Ohshima et al. Scalable quantum photonics with single color centers in silicon carbide. *Nano letters*, **17**, 3, 1782 (2017).

[95] S. Pezzagna, D. Wildanger, P. Mazarov, A. D. Wieck, Y. Sarov, I. Rangelow, B. Naydenov, F. Jelezko, S. W. Hell and J. Meijer. Nanoscale engineering and optical addressing of single spins in diamond. *small*, **6**, 19, 2117 (2010).

[96] J. Taylor, P. Cappellaro, L. Childress, L. Jiang, D. Budker, P. Hemmer, A. Yacoby, R. Walsworth and M. Lukin. High-sensitivity diamond magnetometer with nanoscale resolution. *Nature Physics*, **4**, 10, 810 (2008).

[97] T. D. Ladd, F. Jelezko, R. Laflamme, Y. Nakamura, C. Monroe and J. L. O'Brien. Quantum computers. *Nature*, **464**, 7285, 45 (2010).

[98] N. Jacobsen. *NMR Spectroscopy Explained: Simplified Theory, Applications and Examples for Organic Chemistry and Structural Biology*. Wiley (2007). ISBN 9780470173343.

[99] R. De Graaf. In vivo nmr spectroscopy–dynamic aspects. *In vivo NMR spectroscopy: principles and techniques. 2nd ed. Chichester: John Wiley & Sons*, 111–90 (2007).

[100] L.-P. Yang, C. Burk, M. Widmann, S.-Y. Lee, J. Wrachtrup and N. Zhao. Electron spin decoherence in silicon carbide nuclear spin bath. *Physical Review B*, **90**, 24, 241203 (2014).

[101] A. L. Falk, P. V. Klimov, V. Ivády, K. Szász, D. J. Christle, W. F. Koehl, Á. Gali and D. D. Awschalom. Optical polarization of nuclear spins in silicon carbide. *Physical review letters*, **114**, 24, 247603 (2015).

[102] P. L. Stanwix, L. M. Pham, J. R. Maze, D. Le Sage, T. K. Yeung, P. Cappellaro, P. R. Hemmer, A. Yacoby, M. D. Lukin and R. L. Walsworth. Coherence of nitrogen-vacancy electronic spin ensembles in diamond. *Physical Review B*, **82**, 20, 201201 (2010).

[103] J. Embley, J. Colton, K. Miller, M. Morris, M. Meehan, S. Crossen, B. Weaver, E. Glaser and S. Carter. Electron spin coherence of silicon vacancies in proton-irradiated 4h-sic. *Physical Review B*, **95**, 4, 045206 (2017).

[104] P. Brereton, D. Puent, J. Vanhoy, E. Glaser and S. Carter. Spin coherence as a function of depth for high-density ensembles of silicon vacancies in proton-irradiated 4h-sic. *arXiv preprint arXiv:1812.10432* (2018).

[105] G. Alfieri, E. Monakhov, B. Svensson and M. K. Linnarsson. Annealing behavior between room temperature and 2000 c of deep level defects in electron-irradiated n-type 4h silicon carbide. *Journal of applied physics*, **98**, 4, 043518 (2005).

[106] *Physical Metallurgy Principles*. Cengage Learning (2008).

[107] Y. M. Tairov and V. Tsvetkov. Investigation of growth processes of ingots of silicon carbide single crystals. *Journal of crystal growth*, **43**, 2, 209 (1978).

[108] V. Soltamov, C. Kasper, A. Poshakinskiy, A. Anisimov, E. Mokhov, A. Sperlich, S. Tarasenko, P. Baranov, G. Astakhov and V. Dyakonov. Excitation and coherent control of spin qudit modes in silicon carbide at room temperature. *Nature communications*, **10**, 1, 1 (2019).

[109] T. Biktagirov, W. G. Schmidt, U. Gerstmann, B. Yavkin, S. Orlinskii, P. Baranov, V. Dyakonov and V. Soltamov. Polytypism driven zero-field splitting of silicon vacancies in 6 h-sic. *Physical Review B*, **98**, 19, 195204 (2018).

[110] P. Kehayias, M. Mrózek, V. M. Acosta, A. Jarmola, D. Rudnicki, R. Folman, W. Gawlik and D. Budker. Microwave saturation spectroscopy of nitrogen-vacancy ensembles in diamond. *Physical Review B*, **89**, 24, 245202 (2014).

[111] S. Tarasenko, A. Poshakinskiy, D. Simin, V. Soltamov, E. Mokhov, P. Baranov, V. Dyakonov and G. Astakhov. Spin and optical properties of silicon vacancies in silicon carbide- a review (phys. status solidi b 1/2018). *physica status solidi (b)*, **255**, 1, 1870101 (2018).

[112] W. E. Moerner and G. C. Bjorklund. *Persistent spectral hole-burning: science and applications*, volume 1. Springer (1988).

[113] P. R. Berman. Atom interferometry (1997).

[114] K. Fang, V. M. Acosta, C. Santori, Z. Huang, K. M. Itoh, H. Watanabe, S. Shikata and R. G. Beausoleil. Absolute magnetometry based on quantum beats in diamond nitrogen-vacancy centers. *arXiv preprint arXiv:1212.1495* (2012).

A. Publications and Conference Contributions

Publications in peer-reviewed journals

1. C. Kasper, D. Klenkert, Z. Shang, D. Simin, A. Gottscholl, A. Sperlich, H. Kraus, C. Schneider, S. Zhou, M. Trupke, W. Kada, T. Ohshima, V. Dyakonov and G. V. Astakhov. Influence of Irradiation on Defect Spin Coherence in Silicon Carbide. *Phys. Rev. Appl.*, **13**, 4, 044054 (2020).
2. A. Gottscholl, M. Kianinia, V. A. Soltamov, C. Bradac, C. Kasper, K. Krambrock, A. Sperlich, M. Toth, I. Aharanovich, and V. Dyakonov. Room Temperature Initialisation and Readout of Intrinsic Spin Defects in a Van der Waals Crystal. *Nat. Mat.*, **19**, 540 (2020)
3. A. Opitz, C. Peter, B. Wegner, H. S. S. Ramakrishna Matte, A. Röttger, T. Florian, X. Xu, P. Beyer, L. Grubert, S. Hecht, V. Belova, A. Hinderhofer, F. Schreiber, C. Kasper, J. Pflaum, Y. Zhang, S. Barlow, S. R. Marder, and N. Koch. Ordered Donor–Acceptor Complex Formation and Electron Transfer in Co-deposited Films of Structurally Dissimilar Molecules. *J. Phys. Chem. C*, **124**, 20, 11023 (2020)
4. V. A. Soltamov, C. Kasper, A. V. Poshakinskiy, A. N. Anisimov, E. N. Mokhov, A. Sperlich, S. A. Tarasenko, P. G. Baranov, G. V. Astakhov and V. Dyakonov. Excitation and Coherent Control of Spin Qudit Modes in Silicon Carbide at Room Temperature. *Nat. Comm.*, **10**, 1, 1 (2019).
5. H. Kraus, D. Simin, C. Kasper, Y. Suda, S. Kawabata, W. Kada, T. Honda, T. Hijikata, T. Ohshima, V. Dyakonov and G. V. Astakhov Three-Dimensional Proton Beam Writing of Optically Active Coherent Vacancy Spins in Silicon Carbide. *Nano Lett.*, **17**, 5, 2865 (2017).

Contributed Talks

1. DPG Frühjahrstagung 2018 in Berlin. C. Kasper, V. Soltamov, D. Simin, T. Ohshima, V. Dyakonov and G. V. Astakhov. Engineering of Coherent Defects in Silicon Carbide with Varying Irradiation Methods.
2. ICSCRM 2017 in Washington, D.C. C. Kasper, H. Kraus, D. Simin, Y. Suda, T. Ohshima, W. Kada, A. Sperlich, C. Salter, M. Trupke, V. Dyakonov and G. V. Astakhov. Engineering of Coherent Defects in Silicon Carbide Using Different Irradiation Methods.
3. DPG Frühjahrstagung 2017 in Dresden. C. Kasper, H. Kraus, D. Simin, Y. Suda, T. Ohshima, W. Kada, S. Kawabata, T. Honda, Y. Hijikata, G. V. Astakhov and V. Dyakonov. Defect Engineering in Silicon Carbide.

Conference Posters

1. DPG Frühjahrstagung 2019 in Regensburg C. Kasper, A. Sperlich, T. Ohshima, V. Soltamov G. V. Astakhov and V. Dyakonov. Engineering and Resonant Excitation of Highly Coherent Spin Defects in Silicon Carbide.
2. DPG Frühjahrstagung 2016 in Regensburg C. Kasper, H. Kraus, A. Sperlich, D. Simin, T. Makino, S.-I. Sato, T. Ohshima, G. V. Astakhov and V. Dyakonov. Optical Spectroscopy of Vacancy Related Defects in Silicon Carbide Generated by Proton Irradiation.

B. Danksagung

An dieser Stelle möchte ich mich bei allen bedanken, die direkt oder indirekt an der Entstehung dieser Arbeit beteiligt waren.
Zunächst möchte ich mich bei meinem Doktorvater Vladimir Dyakonov bedanken, der es mir ermöglichte, an seinem Lehrstuhl zu promovieren. Danke für deine Unterstützung bei meiner Arbeit und dass du dir immer Zeit genommen hast, wenn ich eine Frage oder ein Problem hatte. Außerdem hast du mir die Auslandsaufenthalte in Washington und Taksaki ermöglicht. Das ist nicht selbstverständlich und das weiß ich sehr zu schätzen.
Desweiteren geht ein sehr großer Dank an meinen Betreuer Georgy. Du hattest immer ein offenes Ohr und gefühlt auf jede Frage eine Antwort. Deine Ideen haben diese Doktorarbeit geformt und die Gespräche mit dir haben mein Verständnis für das Thema jedes mal verbessert. Ich kann mir keinen besseren Betreuer vorstellen.
Ein Dank geht auch an Hex. Mit dir hatte ich auch viele fachliche Gespräche und Diskussionen, allerdings umso mehr Diskussion über andere Themen. Du bestachst dabei vor allem durch dein unfassbares Wissen an nützlichen und weniger nützlichen Dingen und Fakten.
Ich möchte Dmitrij dafür danken, dass er mich in das Thema dieser Arbeit eingeführt hat und mir helfend zur Seite stand. Gleichermaßen gilt mein Dank Franzi und Hannes für die hilfreichen Tipps und Erklärungen zum Beginn meiner Arbeit.
Weiter bedanke ich mich ganz herzlich bei Valentin und André. Ohne euch wäre ich in vielen Situationen nur sehr viel langsamer voran gekommen. Ihr habt irgendwie alles schon einmal gesehen und deswegen für alles sofort eine Lösung parat. Gleiches gilt für Diep, die mich treu in meinem Kampf gegen die Bürokratie unterstützt und mich unzählige Male an Fristen erinnert hat.
Ein weiterer Dank gebührt meinen Masteranden Dimitrij, Daniel und meiner Masterandin Selina für die gute Arbeit, die ihr geleistet habt und die stets fröhliche und gute Arbeitsathmosphäre. Beim Stichwort Arbeitsathmosphäre will ich mich auch bei allen bedanken, die ich bei meinen täglichen Büro-Touren besucht habe: David für die Gespräche über Fußball, Philipp als Meme-Abnehmer, Julian für SOS, Nathania für Kuchen, Liudmila für Psychoanalysen und Süßigkeiten, Janine dafür, dass sie meistens

Platz gemacht hat, wenn ich vorbei wollte, Simon für die Diskussionen über ein Tempolimit, Kris für Helluuu Dubelup, der Kicker-Crew für die spannenden Matches, Seppo für das Signal auf der Masse und den zweitgrößten Zwetschgenbauern des Universums, Michel und Bernd für 11 Minuten Fußweg und den anschließenden Portugiesisch-Kurs und allen, die noch Zeuge dieser monumentalen Ära an unserem Lehrstuhl sein durften.
Als nächstes möchte ich mich bei Krasniczki Gottscholl und Victor bedanken, mit denen ich sehr viel und sehr oft lange im Labor war, wobei immer für gute Musik gesorgt wurde und der ein oder andere lustige Dateiname entstand. Nun ist der Zeitpunkt gekommen, mich bei einem meiner Masteranden zu bedanken, den ich bis jetzt noch nicht erwähnt habe. Lebende Legende, absolute Waffe, engster Vertrauter der Mechanik-Werkstatt und Kollege Schnürschuh in Personalunion: Michael "007"Hollenbach. Nicht nur wegen unserer bahnbrechenden Erfolge im Labor, sondern vor allem wegen unserer Leidenschaft für Autos und andere gute Dinge haben wir uns mit der Zeit immer besser verstanden und am Ende sind wir Freunde geworden. Auch wenn du oft schwerer auf deinem Telefon zu erreichen bist als der Papst, hoffe ich wirklich, dass wir irgendwann bei Porsche in der selben Abteilung landen.
Ein riesen Dank geht auch an meinen treuen Weggefährten Nikolai. Ohne dich wäre das Studium nur halb so lustig und doppelt so schwer gewesen. Zehn Jahre lang haben wir uns jetzt durch Übungsblätter, Praktika, Klausuren und die Promotion gekämpft und am Ende sind wir auch noch am gleichen Lehrstuhl gelandet. Es war eine schöne Zeit und das CL-Finale 2013 wird auch mir in Erinnerung bleiben.
Ich möchte mich auch bei meinen Eltern für die finanzielle und zusätzlich bei Kerstin und Alexandra für die moralische Unterstützung bedanken. Und natürlich für die Fehlersuche in meiner Arbeit. Wir sehen uns zwar manchmal länger nicht, aber dafür ist es dann wenn es klappt jedes mal umso schöner. Abschließend möchte ich mich noch bei Teo bedanken. Dafür, dass du bist wie du bist und es schaffst mir, egal wie es mir geht, ein Lächeln in mein Gesicht zu zaubern.

Acknowledgment

Die Arbeit an der Universität Würzburg wurde durch die Deutsche Forschungsgemeinschaft (DFG) unterstützt.